

# Out of equilibrium dynamics through a phase transition

Alberto Sicilia



# Contents

<b>1</b>	<b>Introduction</b>	<b>5</b>
1.1	Some concepts in statistical mechanics and phase transitions . . . . .	5
1.1.1	Phases of matter . . . . .	5
1.1.2	Symmetry breaking and phase transitions . . . . .	6
1.1.3	Classification of phase transitions . . . . .	6
1.1.4	Thermal vs. Quantum phase transitions . . . . .	7
1.1.5	Equilibrium vs. Out-of-Equilibrium statistical mechanics . . . . .	8
1.1.6	Different levels in the description of the dynamics . . . . .	9
1.2	Goals of the thesis and results presented in the manuscript . . . . .	11
1.2.1	Geometry of domain growth in $2d$ . . . . .	11
1.3	Results not presented in the manuscript . . . . .	12
1.3.1	Defect formation through a passage by the phase transition. Revision of the classical Kibble-Zurek mechanism. . . . .	12
1.3.2	Geometrical properties of critical parafermionic spin models . . . . .	12
1.3.3	Relaxation in spatially extended chaotic systems . . . . .	13
1.3.4	Coarsening in the Potts model . . . . .	13
1.3.5	Equilibrium and Out-of-Equilibrium dynamics of the Blume-Capel Model . .	14
<b>2</b>	<b>Coarsening: introduction and state of the art</b>	<b>15</b>
2.1	Phenomenology of coarsening . . . . .	15
2.2	Mathematical formalism . . . . .	17
2.3	State of the art . . . . .	18
2.4	Our work . . . . .	19
<b>3</b>	<b>Non-conserved dynamics</b>	<b>21</b>
3.1	Introduction: Hull-enclosed areas and domain areas . . . . .	21
3.2	Coarsening at $T = 0$ . The Allen-Cahn equation. . . . .	22
3.3	Exact result for the distribution of hull-enclosed areas . . . . .	23
3.3.1	Equation of evolution for hull-enclosed areas . . . . .	23
3.3.2	Initial distributions of hull-enclosed areas . . . . .	24
3.3.3	Distribution of hull-enclosed areas during the dynamics . . . . .	25
3.4	Distribution of domain areas . . . . .	28
3.4.1	Initial condition for the distribution of domain areas . . . . .	29
3.4.2	Evolution equation for domain areas during coarsening . . . . .	30
3.4.3	Distribution of domain areas during coarsening . . . . .	34
3.5	Effect of the working temperature . . . . .	35
3.6	Statistics of perimeters and fractal properties . . . . .	40

3.6.1	Initial conditions . . . . .	40
3.6.2	Time evolution at zero temperature . . . . .	42
3.6.3	Finite temperature evolution . . . . .	45
3.7	Conclusions . . . . .	46
<b>4</b>	<b>Effects of the disorder: test of the super-universality hypothesis</b>	<b>47</b>
4.1	Introduction . . . . .	47
4.2	Hull enclosed area distribution . . . . .	47
4.3	Geometrical structure . . . . .	50
4.4	Hull length distribution . . . . .	51
4.5	Conclusions . . . . .	52
<b>5</b>	<b>Conserved dynamics</b>	<b>55</b>
5.1	Phase separation: Introduction and state of the art . . . . .	55
5.2	Statistics of areas: analytic results . . . . .	58
5.2.1	Initial distribution . . . . .	58
5.2.2	Characteristic domain length . . . . .	59
5.2.3	Large structures . . . . .	59
5.2.4	Small structures . . . . .	59
5.2.5	Super universality . . . . .	60
5.3	Statistics of areas: numerical tests . . . . .	61
5.3.1	Domain areas . . . . .	62
5.4	Statistics of perimeters and fractal properties . . . . .	63
5.5	Conclusions . . . . .	65
<b>6</b>	<b>Experiments in the coarsening dynamics of liquid crystals</b>	<b>67</b>
6.1	Introduction . . . . .	67
6.2	Experimental setup . . . . .	67
6.3	Analysis of the images . . . . .	68
6.4	Conclusion . . . . .	71
<b>7</b>	<b>Geometry of <math>2d</math> coarsening: a final picture emerging</b>	<b>73</b>
<b>A</b>	<b>Algorithm to obtain the hull enclosed area</b>	<b>75</b>

# Chapter 1

## Introduction

### 1.1 Some concepts in statistical mechanics and phase transitions

#### 1.1.1 Phases of matter

Matter can be found in a large number of different states. Understanding and describing such a variety in the nature of matter is a central problem not only in physics but also in chemistry and biology (at the end of the day, we are all complex matter!). Let us give three examples, ranging from high energies to very low temperatures:

- Cosmologists and particle physicists try to elucidate the nature of matter in the first moments of the Universe after the Big Bang. The understanding of the different phases of nuclear matter, such as the *quark-gluon* plasma is another open challenge.
- At room temperatures, the properties of a type materials known as *glasses* depend on their thermal history. In this category we find the familiar *structural glasses*, but also *dense granular matter* or *proteins*. There is a longstanding debate about their underlying stable phase and whether there is a phase transition in the hypothetical limit of infinitely long relaxation times.
- At very low temperatures, strongly correlated electrons in metallic layers can form *Mott insulators*, *fractional quantum-Hall matter*, *heavy fermion materials*. These materials show unusual (but technologically very useful) properties, such as superconductivity. Even in the theoretical limit of zero temperature, matter can be found in a variety of phases, depending on the strength of quantum fluctuations.

The quest for the understanding of the nature of matter has lead to a vast interdisciplinary cross-fertilization with other fields of physics and mathematics. Field theory, developed to describe *quantum relativistic* theories is now a fundamental tool in *classical non-relativistic* statistical mechanics. In the opposite way, the BCS and Ginzburg-Landau theories of superconductivity were the main ideas leading to the formulation of the Higgs mechanism in particle physics.

New problems often involve developing new mathematical tools, that then can be used in different disciplines. For example, mathematical concepts developed for the study of glassy systems, such as replica symmetry breaking are now central in computer science. The study of  $2d$  critical phenomena has given a fabulous push to a very important field in modern mathematics: the geometry of random curves. The mathematical framework developed to understand the movement of a pollen grain in a fluid (stochastic processes) is now at the core of the analysis of financial markets.

### 1.1.2 Symmetry breaking and phase transitions

Given the variety in the phases of phases described in the previous paragraphs, a natural step forward is to study the nature of the transformations from one to another, i.e., *phase transitions*.

Phase transitions are usually characterized by the system undergoing a transition from a symmetric (*disordered*) state which incorporates some symmetry of the Hamiltonian to a broken-symmetry (*ordered*) state which does not have that symmetry, although the Hamiltonian still possesses it. Typically, the more symmetrical phase is on the high-temperature side of a phase transition, and the less symmetrical phase on the low-temperature side. This happens because the Hamiltonian exhibits all the possible symmetries of the system, whereas the low-energy states lack some of these symmetries. At low temperatures, the system tends to be confined to the low-energy states. At higher temperatures, thermal fluctuations allow the system to access states in a broader range of energy, and thus more of the symmetries of the Hamiltonian.

A good example is given by a spin ferromagnet: the relevant symmetry of the Hamiltonian is the rotational symmetry in spin space, and the disorder and ordered states are represented by the paramagnetic and the ferromagnetic states, respectively. In the former, there is no preferred direction for the magnetic moments of the spins. The net magnetization is therefore zero, and the state has the same spin rotational symmetry as the Hamiltonian. That is, if we rotate the coordinate system in spin space, then the system still looks the same. In the ferromagnetic phase, there is a preferred direction for the spins, and this is the direction which the overall magnetization will point in. The state therefore does no longer respect the spin rotational symmetry, and we say that the symmetry is *spontaneously broken* (spontaneously in order to distinguish this phenomenon from the explicit breaking that occurs if we apply an external field).

The *order parameter* is a quantity that measures the degree of order in the system. It is usually defined as zero in the disordered phase and non-zero in the ordered one. For example, in a ferromagnetic system the order parameter is the net magnetization.

### 1.1.3 Classification of phase transitions

A phase transition is then characterized by an abrupt change in value of the order parameter given a smooth change of a control parameter, that is in general the temperature or some other thermodynamic field. This abrupt change implies a discontinuity in the  $n^{th}$  derivative of the free energy density at the transition point. The traditional classification of phase transitions, due to Ehrenfest, group phase transitions according to the degree of non-analyticity involved.

- *First order phase transitions* exhibit a discontinuity in the first derivative of the free energy with a thermodynamic variable. The various solid/liquid/gas transitions are classified as first order transitions because they involve a discontinuous change in density (which is the first derivative of the free energy with respect to the chemical potential). First-order phase transitions involve a latent heat: during such a transition, a system either absorbs or releases a fixed amount of energy. First-order transitions are associated with mixed-phase regimes in which some parts of the system have completed the transition (jumping over the energy barrier) and others have not. This phenomenon is familiar to anyone who has boiled a pot of water: the water does not instantly turn into gas, but forms a mixture of water and water vapor bubbles.
- *Second order phase transitions* Second-order phase transitions are continuous in the first derivative but exhibit a discontinuity in a second derivative of the free energy. These include the ferromagnetic phase transition in materials such as iron, where the magnetization (which

is the first derivative of the free energy with the applied magnetic field) increases continuously from zero as the temperature is lowered below the Curie temperature. The magnetic susceptibility, the second derivative of the free energy with respect to the field, changes discontinuously. They have no associated latent heat. It turns out that in a continuous phase transition, thermodynamic quantities diverge as power-law functions of the control parameter. It is customary to describe the phase transition by its exponents, known as *critical exponents*. It is a remarkable experimental fact that second order phase transitions arising in different systems often possess the same set of critical exponents. This phenomenon is known as *universality*. For example, the critical exponents at the liquid-gas critical point have been found to be independent of the chemical composition of the fluid. More amazingly, they are exactly the same as the critical exponents of the ferromagnetic phase transition in uniaxial magnets. Such systems are said to be in the same *universality class*. Universality is naturally explained in the framework of renormalization group theory: the thermodynamic properties of a system near a phase transition depend only on a small number of features, such as dimensionality and symmetry, and are insensitive to the underlying microscopic properties of the system. The fact that the critical behavior is independent of the microscopic details of the Hamiltonian is due to the diverging correlation length. In order to correctly describe the universal critical behaviour it is then sufficient to work with an *effective theory* that keeps explicitly only the large-distance behavior of the original Hamiltonian.

- *Infinite order phase transitions* are continuous phase transitions, but break no symmetries. The most famous example is the Kosterlitz-Thouless transition in the two-dimensional  $XY$  model.

#### 1.1.4 Thermal vs. Quantum phase transitions

A fundamental question is the following: to what extent is quantum mechanics necessary in order to understand critical phenomena, and to what extent will classical physics suffice? Generally speaking, quantum mechanics is important whenever the temperature goes below some characteristic energy of the system under consideration. For instance, in an atom, the characteristic energy is the Rydberg energy. Let us assume its value is  $\hbar\omega_c$ . It then follows that quantum mechanics will be important when  $k_B T < \hbar\omega_c$ . This indicates that for any phase transition that takes place at a non-zero temperature, the critical behavior asymptotically close to the transition can be described by classical physics. These phase transitions are called *classical or thermal transitions*. What drives the correlation length to infinity are *thermal fluctuations*, which become very large close to the critical point.

In contrast, we can think of a transition that occurs at zero temperature, and that is triggered by varying some non-thermal parameter (e.g. a coupling constant in the microscopic Hamiltonian). These transitions are called *quantum or zero-temperature* phase transitions. Even at zero temperature a quantum-mechanical system has *quantum fluctuations* and therefore can still support phase transitions.

Note that some phase transitions in systems that are considered as the paradigm of quantum mechanics, like the superconducting transition in mercury or the  $\lambda$ -transition in helium are thermal transitions. Indeed, in both cases the critical behavior (but not the physical mechanisms or the properties of either phase) can be understood entirely using classical physics. By the way, this is the very reason for the fact that there are three Nobel Prizes for the theoretical description of superconductivity. In 1950, the phenomenological theory of superconductivity was devised by Landau and Ginzburg. The complete microscopic theory of superconductivity was finally proposed

in 1957 by Bardeen, Cooper, and Schrieffer. In 1959, Lev Gorkov showed that the BCS theory reduced to the Ginzburg-Landau theory close to the critical temperature.

### 1.1.5 Equilibrium vs. Out-of-Equilibrium statistical mechanics

- *Equilibrium dynamics.* Usually, when studying equilibrium properties of a system, it is not necessary to know its *microscopic dynamics*. The *ergodic theorem* states that computing ensemble averages is equivalent to taking time averages. This equivalence also allow us to perform simulations in which we explore very efficiently the phase space by implementing *non physical movements*.
- *Out of equilibrium, but close to equilibrium: the linear regime.* If we slightly deviate a system from its equilibrium state by applying an instantaneous perturbation, the system will then relax to the equilibrium state by dissipating the energy transfered in the kick. The idea of relating the amplitude of this dissipation to the amplitude of fluctuations in equilibrium, dates back to Einstein's work in Brownian motion. Later, Onsager, established the hypothesis that the relaxation of a macroscopic nonequilibrium perturbation follows the same laws which govern the dynamics of fluctuations in equilibrium systems. This results represents a fundamental tool in non-equilibrium statistical mechanics since it allows one to predict the average response to external perturbations, without applying any perturbation. In fact, via equilibrium simulations one can compute correlation functions at equilibrium and then, using the Green-Kubo formula, obtain the transport coefficients. Note the difference between this and to use directly the definitions of transport coefficients: one perturbs the system with an external force or imposes driving boundary conditions (e.g. a shear) and observes the relaxation process. It is in the framework of the out of equilibrium linear regime where Onsager developed the ideas on *Irreversible Linear Thermodynamics*.
- *Far from equilibrium in a Stationary state. Non-equilibrium steady states.* Imagine that we coupled our system to two thermal reservoirs with different temperatures or two particle reservoirs with different chemical potentials. It is reasonable to assume that after a transient interval, a steady state is eventually reached. Although its statistical properties will be time-independent, this state will be very different from the equilibrium one. The fluctuations of far from equilibrium systems are much richer than equilibrium ones because time-reversibility is lost, and the Gibbs-Boltzmann distribution does not hold. This kind of states are the natural playground of the recently developed *Fluctuation Theorems* [1, 2, 3].
- *Crossing a phase transition out of equilibrium.* Another possibility to force a system to a far from equilibrium situation is by changing rapidly some of the control parameters, in such a way that we force it to cross a phase transition. The system will subsequently relax to the equilibrium state corresponding to the new values of the control parameters. This relaxation usually exhibits *slow dynamics* and the relaxation time eventually diverges in the thermodynamic limit.

The relaxation process will depend on the nature of the transition crossed. Let us consider first the case of a system crossing a second order phase transition. Due to symmetry breaking, in the low temperature phase there will exist several different ground states in which the order parameter takes different values. In an Ising ferromagnet we have two minima in the ferromagnetic phase: all the spins pointing up or all the spins pointing down. As we force our system to cross the transition at a finite velocity (or even instantaneously in a quench), different regions of the system will choose different minima of the free energy. This leads to the



appearance of *topological defects*. Note that the local choice of the minima is instantaneous when crossing a second order phase transition, because there is no energy barrier to overcome. In the Ising ferromagnet this example corresponds to the appearance of regions where the spins are parallel and pointing either up or down. These regions are called *domains* and their *walls* are the corresponding defects.

In order to reach the equilibrium state, the system needs to eliminate these defects. This process is known as *coarsening* or *phase ordering dynamics*. One of the most striking features of this out of equilibrium evolution is a *dramatic slowing down* in the dynamics. Looking at two-times quantities that depend on two times  $s$  and  $t$  (where  $t > s$ ), we observe that the decay as a function of  $t$  is slower for larger  $s$ . This phenomenon is usually referred to as *ageing*: older samples respond more slowly. An important aspect of ageing systems is that the equilibrium fluctuation-dissipation theorem (FDT) does not hold. Such violations of the FDT have been the starting point for the introduction of fruitful ideas such as non-equilibrium fluctuation-dissipation relations and effective temperatures [4, 5, 6, 7].

We can also think of a system crossing a first order phase transition. As discussed before, first order phase transitions are characterized by the existence of metastable states in the phase diagram region defined by the *spinodal lines*. Metastability is the consequence of the existence of energy barriers that the system needs to overcome in order to reach the low temperature phase. Two well defined time intervals characterize then the relaxation process: first, the system needs to wait until a large enough thermal fluctuation that allows it to cross the energy barrier is produced (*nucleation*). Then, the low temperature phase can *grow* to cover all the system.

### 1.1.6 Different levels in the description of the dynamics

- *Microscopic equations*. In principle, the *true dynamics* of a system is specified by its microscopic equations of motion. Depending on the system under consideration, they can be:
  - Classical equations of motion: Newton or Hamilton equations (e.g., as it is usually considered in “soft-matter” physics).
  - Quantum equation of motion: Heisenberg or Schrödinger equations (e.g., as it is usually considered in “hard” condensed matter problems).
  - Equations of motion for the fields (e.g., as it is usually considered relativistic quantum field theories).

However, solving the dynamics in this fully microscopic approach is rarely viable for many body systems, even numerically. Moreover, in some situations only a few number of all the degrees of freedom play an interesting role. We need then to introduce some kind of “coarse-grained” dynamics. The new dynamics are usually constructed by integrating out the *fast* degrees of freedom in the problem, which give rise to some effective *stochasticity*:

- *Master equation*. This approach makes use of the representation of the dynamics as a stochastic process defined in the space of configurations of the system. At this description level, one has to assign the transition rates between different configurations on the basis of physical considerations. Then, the master equation rules the time evolution probability of finding the system in a given state.

- *Mesoscopic level: Langevin equation.* A *phenomenological* description in terms of mesoscopic variables is in some cases preferable, since it focuses directly on those quantities that are expected to determine the dynamical properties at length and time scales (referred as mesoscopic) that are much larger than the microscopic ones but still small compared to the macroscopic one (set by the dimension of the sample). A viable approach to dynamics, which was first successfully applied to Brownian motion, consists of a description taking advantage of the separation between the typical time scale of fast and slow dynamical processes. This separation of time scales emerges naturally in many problems. An example is a colloidal suspension in a fluid, where the molecules of the fluid play the role of the heat bath while the colloidal particles move much slower. It is natural to assume that the dynamics of the mesoscopic observables can be described as a result of an effective slow deterministic drift towards a stationary state (equilibrium or not) and of a stochastic force that sums up the effects of the fast microscopic fluctuations. The mathematical implementation of this idea is known as the *Langevin equation*. Of course, this description fails to reproduce the dynamics taking place at microscopic time and length scales. Hence, when the macroscopic physics is crucially related to some microscopic events, such a mesoscopic description is not expected to capture the relevant physical mechanisms. During this work, we will consider systems for which the mesoscopic description is feasible. The Langevin equation is rarely derived rigorously from the underlying microscopic dynamics, and some *ad hoc* assumptions must be done. To compensate for insufficient microscopic information, great care with physical intuition goes into choosing the order parameter and its equations of motion.

## 1.2 Goals of the thesis and results presented in the manuscript

*The goal of this thesis was to gain some understanding in the dynamics of systems forced to cross a phase transition out of equilibrium.* This being a vast research field, we have studied in detail some particular problems summarized in the next paragraphs.

### 1.2.1 Geometry of domain growth in $2d$

When a system is instantaneously quenched through a second order phase transition, the relaxation proceeds by the annihilation of defects. In this case, defects are the walls separating the domains where the order parameter takes one of the two possible equilibrium values. This dynamical process is known as “domain growth” or “coarsening” [8].

In this manuscript we present and discuss analytical results, simulations and experiments in the phase ordering dynamics of  $2d$  systems. A general idea along our work will be to study this phenomenon from a *geometrical point of view*. This project has been done in collaboration with Alan Bray (Manchester), Jeferson Arenzon (Porto Alegre) and Leticia Cugliandolo (LPTHE, Paris).

The structure of the manuscript is the following:

Chapter 2 is a general introduction to phase ordering dynamics. We present in detail the phenomenology of coarsening phenomena and the state of the art.

In chapter 3 we obtain some exact results for the coarsening dynamics of a non-conserved scalar field in two dimensions. In particular, we obtain the distribution of the areas enclosed by the domain walls at any moment during the evolution. This result provides the first analytical proof of the dynamical scaling hypothesis for two-dimensional curvature driven coarsening. We also compute some other geometrical quantities such as the distributions of domain areas and lengths, and the fractal properties of the boundaries.

In chapter 4, we analyze the coarsening dynamics of two-dimensional models with non-conserved order parameter under the effect of weak quenched disorder. By “weak disorder” we mean randomness that does not modify the character of the ordered phase. An important property of the domain growth in systems with weak disorder is the so-called “super-universality hypothesis” that states that once the correct growing length scale is taken into account, all scaling functions are independent of the disorder strength. In particular, the scaling functions of the disorder system are the same than the ones corresponding to the pure (non disorder) one. Having obtained the exact scaling function for the distribution of wall enclosed areas in the pure case, we can then put to the test the super-universality hypothesis. Comparing the scaling function of the disorder case, obtained numerically, with the ones obtained analytically in the pure case, we conclude that the super-universality hypothesis applies to the random bidimensional ferromagnet.

In chapter 5 we extend the geometrical analysis previously developed to the domain growth in systems where the order parameter is a conserved quantity (e.g. demixing in binary fluids). This work was done in collaboration with Yoann Sarrazin, student at the Master in Theoretical Physics of Complex Systems at Paris 6 and whom I co-supervised during his stage.

In chapter 6 we present an experiment in the coarsening dynamics of liquid crystals. We performed this experiment in collaboration with the group lead by Ingo Dierking (Manchester). When the liquid crystal is confined in a quasi- $2d$  layer and an electric field is applied between the top and the bottom plates of the layer, domain growth is observed. Comparing the experimental measurements with our predictions, we conclude that the coarsening dynamics in this liquid crystal is a curvature-driven process. Moreover, we show that our analytical results can be used as an experimentally-useful test for this dynamical universality class.

The manuscript finishes with chapter 7, in which we discuss the global picture of domain growth in  $2d$  emerging from our studies.

The results presented in this manuscript have been published in a series of papers [9, 10, 11, 12], and [13] to be published.

### 1.3 Results not presented in the manuscript

#### 1.3.1 Defect formation through a passage by the phase transition. Revision of the classical Kibble-Zurek mechanism.

Crossing a symmetry breaking phase transition at a *finite* velocity causes the formation of topological defects. A natural question is then to understand how the density of defects created depends on the velocity at which the transition is crossed.

This problem has been mainly investigated by cosmologists, trying to understand the first moments of the universe. After the Big Bang, as the fireball expands, the temperature of the universe decreases. These could have lead the universe to go through a serie of symmetry breaking phase transitions, which precise number is still matter of debate. As the typical temperatures of these phase transitions are orders of magnitude higher than ones that can be obtained in particle accelators, the study of the defects is the only possible way to understand the phase transitions in the early universe [14, 15, 16, 17].

In the late 70's, Tom Kibble [18] proposed a theoretical framework to compute the density of defects as a function of the cooling rate at which the transition is crossed. Some years later, W. Zurek pointed out that, as the Kibble mechanism was only based on universality arguments, it could be possible to test it by performing experiments in condensed matter systems [19, 20].

Despite a vast experimental interest, the Kibble-Zurek (KZ) mechanism has never been proven nor refuted. Some of the most notorious experiments are [21, 22, 23]. A complete review of other experiments can be found in [24]. The KZ mechanism has also been applied very recently to the study of quantum non-dissipative systems crossing a zero temperature phase transition [25, 26, 27, 28].

In collaboration with Giulio Biroli (Saclay) and Leticia Cugliandolo we proposed a critical revision of this classical framework. We were concerned by some of the assumptions used by KZ. In particular, the critical dynamics and the phase ordering dynamics in the ordered phase are not taken into account in their arguments. We have proposed a new scaling, which includes the effect of both process. We have tested our scaling with an analytical calculation in the  $O(N)$  model, for  $N \rightarrow \infty$  and Monte Carlo simulations in the  $2d$  Ising model. This work will be published soon [29].

#### 1.3.2 Geometrical properties of critical parafermionic spin models

The understanding of critical phenomena has been one of the central issues in statistical mechanics for the last decades. A prominent role has been played by the investigation of  $2d$  systems, because they are believed to enjoy *conformal symmetry*. Conformal Field Theory (*CFT*) provides tools for the exact computation of all the critical exponents [30, 31]. In spite of its fundamental role, conformal invariance of  $2d$  critical systems remains a *conjecture*. Rigorously proving that scale invariance implies conformal invariance has been a long-standing challenge in modern mathematics. The recent introduction of the so-called Schramm-Loewner-Evolution (*SLE*) has allowed the proof of conformal invariance in some models [32].

Another issue that arises in the study of  $2d$  conformal invariant theories is the role played by additional symmetries. The so-called, *non-minimal CFTs* obey conformal symmetry but also

additional symmetries. These additional symmetries are for example the  $SU(2)$  spin-rotational symmetry in spin-chains [33] or replica permutational symmetry in disordered systems [34, 35]. By now, the connexion between  $SLE$  and minimal  $CFT$ s is completely understood [36]. Some attempts have been made recently to extend the connexion to non-minimal  $CFT$ s [37, 38], but the geometrical properties of non-minimal  $CFT$ s are still poorly understood.

In collaboration with Marco Picco (LPTHE, Paris) and Raoul Santachiara (LPT ENS Paris, now at Orsay) we studied the geometrical properties of spin models with an additional  $Z_N$  symmetry under the cyclic-permutation of the spin states.

For  $N = 2$  and  $N = 3$  these models correspond to the well known Ising and three-states Potts models, whose critical points are described in the continuum limit by minimal  $CFT$ s. All the physical properties of these models are known to be encoded in the percolation properties of geometrical objects known as  $FK$  clusters [39, 40, 41, 42, 43, 44, 45].

$Z_N$  models with  $N \geq 4$  admit critical points described by non-minimal  $CFT$ s [46, 47, 48]. In the cases  $N = 4$  and  $N = 5$ , we showed numerically that the  $FK$  construction is no longer valid, since these objects do not percolate at the critical point of the  $Z_N$  model. We also computed the fractal dimension for spin clusters that do percolate at criticality. The results obtained point out important differences in the behavior of the geometrical clusters between the cases  $N = 2$  and  $N = 3$  and non-minimal  $CFT$ s. This can be traced back to the fact that, for  $N \geq 4$ , the internal  $Z_N$  degrees of freedom play a fundamental role. Our results have been published in [49].

### 1.3.3 Relaxation in spatially extended chaotic systems

It is believed that statistical mechanics has its origins in the fundamental equations of motion of many body systems. For classical systems, equations of motion are *deterministic* and statistical ensembles are expected to be *effective* descriptions of the system. But it still remains an open problem to rigorously prove that the solutions of the fundamental equations really yield the same results as the statistical mechanics ones.

In principle, the deterministic equations of motion should describe not only the equilibrium properties of a system but also the dynamical ones. As discussed in Sect. (1.1.6), in statistical mechanics, dynamics is often given by some effective *stochastic* equation of motion, e.g., Langevin equations or Monte Carlo algorithms. So the question is up to what point the chaotic deterministic equations of motion are equivalent to Langevin equations. Chaos is suggested to be responsible of the way microscopic deterministic laws of motion lead to non-equilibrium phenomena, such as transport and entropy production.

In collaboration with Eytan Katzav (LPS ENS Paris, now at King's College, London), we analyzed the relaxation dynamics of coupled map lattices [50, 51, 52, 53]. Our results show that these deterministic chaotic systems share many properties with their stochastic counterparts. Various links with out of equilibrium statistical mechanics problems can be drawn to understand this type of extensively chaotic regimes. A preprint is in the course of preparation [54].

### 1.3.4 Coarsening in the Potts model

In collaboration with Marcos Loureiro (Porto Alegre), Jeferson Arenzon, Alan Bray and Leticia Cugliandolo, we studied the coarsening dynamics of the Potts model. The Potts model out of equilibrium presents rich applications in soft-condensed matter, since it describes the dynamical properties of a variety of complex materials such as foams and cellular tissues [55].

From a theoretical point of view, the study of the Potts model allowed us to understand how the coarsening proceeds when dealing with more than two competing ground states. In [56], we

showed that although the underlying dynamical process is the same as the one for the systems with only two competing states, the geometrical properties are quite different in both kinds of systems.

### 1.3.5 Equilibrium and Out-of-Equilibrium dynamics of the Blume-Capel Model

To better understand the effects of the different kinds of phase transitions in the relaxation dynamics, we have also started the study of the Blume-Capel model [57, 58]. Introduced to mimic phase transitions in magnetic mixtures, the phase diagram of this model shows both first and second order transition lines, separated by a tricritical point. It is therefore possible to explore the interplay between coarsening (crossing the second order phase transtion) and nucleation and growth (crossing the spinodal lines).

Before starting the study of the out of equilibrium dynamics, we needed to obtain a precise knowledge of the equilibrium phase diagram. We performed first an analytical mean field analysis which gave us a rough but very useful idea of the properties of the model. Then, by using powerful simulation techniques such as the Wang-Landau algorithm [59] and finite size scaling [60], we were able to reconstruct very precisely the phase diagram of the Blume Capel model.

This work is being done in collaboration with Camille Aron (LPTHE), Leticia Cugliandolo and Marco Baitsy-Jessi, student at the Master in Theoretical Physics at Ecole Normale Supérieure and whom I co-supervised during his stage. The project is still in progress and we hope to publish our results at some time in the future.

## Chapter 2

# Coarsening: introduction and state of the art

### 2.1 Phenomenology of coarsening

Let us suppose that we instantaneously quench a system initially in equilibrium at a high temperature  $T_0$ , to a temperature  $T$  equal or lower than the critical one. Due to symmetry breaking, the order parameter must choose one between the new possible equilibrium free energy minima. Because of the instantaneous quench, different parts of the system cannot communicate to each other which minima they choose. The order parameter will then take different values in different regions of the space and topological defects will appear. This mosaic of ordered phases will evolve in time, since distinct broken-symmetry phases compete with each other in the quest to select the low-temperature thermodynamic equilibrium state. As a result of this competition, equilibrium is never reached for an infinite system. This out-of-equilibrium process is known as “coarsening” or “phase ordering dynamics”.

The simplest example of a system exhibiting phase ordering kinetics is a ferromagnet quenched from a temperature above its critical temperature to a temperature below it. After the quench such a system is brought into a thermodynamically unstable state. The two possible phases are characterized by a positive and a negative magnetization respectively. Since both of the coexistent (positive and negative) phases are equally likely to appear, the system consists of domains of these two phases. During the phase ordering towards one of the two equilibrium states, the domains coarsen and the system orders over larger and larger length scales.

Note that phase ordering is typical of second order phase transitions. In the course of a first order phase transition, a new broken symmetry phase nucleates after the temperature falls some distance below the transition temperature. Separated islands of the new phase form independently and expand, resulting in a local selection of the broken symmetry vacuum. Second order phase transitions are different. Here, the phase transition occurs simultaneously throughout the volume, because there is no energy barrier to overcome. The resulting broken symmetry phase will contain many distinct regions with different choices of the vacuum.

A central feature of this out-of-equilibrium evolution is the experimental observation that the system “looks statistically the same” at different times. Only its overall length scale changes. This observation is the origin of the so-called *dynamical scaling hypothesis*. The hypothesis states that a system in the late stages of coarsening is described by a single characteristic length scale  $R(t)$  that grows with time. As a result, for any observable, all time-dependencies are encoded in  $R(t)$  and all length-dependencies appear scaled by this typical length. The growth law  $R(t)$  depends

critically on the nature of the order parameter and the spatial dimensionality of the system as well as the presence of conservation laws.

The empirically observed scaling behaviour, involving the single length scale  $R(t)$ , suggests that a renormalization group (RG) treatment might be fruitful [61]. The foundations of RG treatments of coarsening are however not as robust as for equilibrium critical phenomena. This is due to the nonperturbative character of the dynamical problem: there is not an upper critical dimension for this dynamical process [8]. Although an approach based fully on the RG is not available, complementing RG techniques with a physically motivated ansatz can give a lot of useful information. These kind of procedures suggest that there are basically two different coarsening scenarios [8, 62, 61, 63, 64, 65, 66]:

- For  $T < T_C$ , phase ordering proceeds essentially as for  $T = 0$  (apart from some  $T$ -dependent prefactor).
- For  $T = T_C$ , phase ordering is different (usually referred as “critical coarsening”).

Note that when quenching to a temperature  $T > T_c$ , the dynamics is trivial because the system relaxes exponentially fast to thermal equilibrium, even in the thermodynamic limit. In the following we will only discuss the  $T < T_C$  case.

The dynamical scaling hypothesis supports the idea of a universal character of the phase ordering dynamics, that would allow for a definition of non-equilibrium universality classes where quantities would be the same in the whole low temperature phase. The observables will be independent of microscopic details and only associated with the Hamiltonian symmetries, dimension or equations of motion. For example, it has been long understood that the results depend crucially on whether the order parameter is conserved or not.

The existence of a  $T = 0$  temperature fixed point agrees with the physical idea that  $T$  only determines the size of the thermal islands inside the domains, leaving unchanged large-scale long-time properties of the interface motion. When domains are large, their bulk is in quasi-equilibrium in one of the broken symmetry phases, while the motion of the boundaries keeps the system globally out of equilibrium. At a given time  $t$ , non-equilibrium effects can be detected by looking over distances larger than  $R(t)$ , because in this case one or more interfaces will be observed. In terms of time, non-equilibrium effects can be observed for times  $t$  and  $s$  separated enough  $t - s > t$ , because in this time scale at least one interface has typically crossed the observation region [67].

A lot of interest in the study of coarsening has been recently generated because of its close relation with the dynamics of structural and spin glasses. Coarsening problems are the first step in the long-standing quest for a coherent theoretical picture of glassy dynamics. Just like glassy systems, coarsening systems show *slow dynamics*. One of the defining features of slow dynamics is *ageing*: observables that depend on two times ( $t$  and  $s$ , where  $t > s$ ) do not depend on  $t - s$ , even for long times. Furthermore, their decay as a function of  $s$  is slower for larger  $t$ . Ageing behaviour has been experimentally observed in a variety of systems [68]. An important aspect of ageing systems is that the fluctuation-dissipation theorem (FDT) does not hold. Such violations of FDT have been the starting point for the introduction of fruitful ideas in the field of glassy systems such as non-equilibrium fluctuation-dissipation relations and effective temperatures [4, 5, 6, 7]. These ideas are under experimental investigation in glassy and granular materials [69, 70, 71, 72]. Violations of the FDT are not peculiar to glassy or disordered systems: a magnetic material undergoing coarsening displays non-trivial fluctuation-dissipation relations.

The study of defect dynamics is another important issue. As explained before, topological defects are formed when crossing the symmetry breaking transition because the order parameter chooses different equilibrium states in different regions of the space. If the order parameter is a



scalar field, the topological defects are domain walls. Domain walls are surfaces on which the order parameter vanishes and which separate domains of different equilibrium phases. In the case of a vector field, depending on its number of components and the dimension of the space, topological defects can be vortices, strings, monopoles or textures. A physical approach to coarsening is based on studying the structure and dynamics of the topological defects. In some cases, ordering occurs by mutual defect-antidefect annihilations, such as in the Ising chain, where the up and down domains are separated by point-like interfaces performing random walks. In other cases, such as in curvature-driven coarsening, domain walls shrink and disappear.

## 2.2 Mathematical formalism

Now that the phenomenology of phase ordering has been discussed, let us introduce the mathematical framework used to study it.

In view of the universality properties supported by experimental data, it is possible to study this collective behaviour in a formal Landau approach to phase transitions. Indeed, as long as one is interested in the behaviour at mesoscopic lengths and time scales, an effective Hamiltonian which reflects the internal symmetries of the underlying microscopic system can be used.

In the following, we will consider a scalar order parameter  $\phi(\vec{x}, t)$ , short range interactions and a second-order phase transition to an ordered state with two possible equilibrium phases. The Hamiltonian is then given by,

$$H[\phi] = \int d^d x \left[ \frac{1}{2} (\nabla \phi)^2 + \frac{r}{2} \phi^2 + \frac{g}{4} \phi^4 \right] \quad (2.1)$$

with  $r < 0$  and  $g > 0$ .

Because of the additional universality of the dynamics, effective equations of motion can be introduced as well. A classification of several dynamical universality classes was done in the early seventies and is reviewed in the classical paper of Hohenberg and Halperin [73]. These universality classes have been named with capital letters, from *A* to *J*. In the following we introduce the two dynamical universality classes that we will consider in our work.

- *Model A* is constructed phenomenologically by asserting that the order parameter changes at a rate that is proportional to the local thermodynamical force  $\frac{\delta H[\phi]}{\delta \phi(\vec{x}, t)}$ . The system flows down the free energy gradient until one of the potential minima is reached. The dynamics is then dissipative: the equation of motion contains only a first derivative on time

$$\frac{\partial \phi(\vec{x}, t)}{\partial t} = -\frac{\delta H[\phi]}{\delta \phi(\vec{x}, t)} + \eta(\vec{x}, t) \quad (2.2)$$

The white noise  $\eta(\vec{x}, t)$  represent the thermal agitation generated by a thermal bath at temperature  $T$ . This noise is a Gaussian distributed random scalar field with zero mean and correlation,

$$\langle \eta(\vec{x}, t) \eta(\vec{x}', t') \rangle = 2T \delta^d(\vec{x} - \vec{x}') \delta(t - t'). \quad (2.3)$$

Equation (2.2) without the noise term is the well known time-dependent Ginzburg Landau equation. A system described by a nonconserved scalar field in  $d > 2$  coarsens by curvature domain growth. The domain growth law in this case is  $R(t) \sim t^{1/2}$ . At the basis of this result is the so called *curvature driven* mechanism: the existence of a surface tension implies a force

per unit of boundary area proportional to the mean curvature, which, in turn, is proportional to the inverse of  $L(t)$ . For model A this readily gives the  $t^{1/2}$  growth law independent of dimensionality. Real systems belonging to this dynamical universality class are for example anisotropic alloys and magnets [73].

- *Model B.* In some cases model A is not suited to describe the dynamics of physical systems. For instance, when the order parameter is related to the density of particles in a fluid, as it is the case when studying the liquid-gas transition, one expects a continuity equation to be obeyed. The simplest model in which such a local conservation law is implemented is known as model B, according to the classification of [73]. At a phenomenological level, we seek a dynamical equation that ensures that the flux of atoms of each element of the alloy can be expressed in the form of a conserved continuity equation

$$\frac{\partial \phi(\vec{x}, t)}{\partial t} + \nabla \vec{J}(\vec{x}, t) = 0. \quad (2.4)$$

We have considered again dissipative dynamics so that the equation of motion is first order in time. The simplest choice for  $\vec{J}$  that involves gradient descent in the free energy landscape is  $\vec{J}(\vec{x}, t) \propto -\nabla \frac{\delta H[\phi]}{\delta \phi(\vec{x}, t)}$ . The equation of motion for model B is then

$$\frac{\partial \phi}{\partial t} = \nabla^2 \left( \frac{\delta H[\phi]}{\delta \phi(\vec{x}, t)} \right) + \eta(\vec{x}, t). \quad (2.5)$$

The stochastic field  $\eta(\vec{x}, t)$  represents a thermal Gaussian noise of zero average and correlator given by

$$\langle \eta(\vec{x}, t) \eta(\vec{x}', t') \rangle = -2T \nabla^2 \delta^d(\vec{x} - \vec{x}') \delta(t - t') \quad (2.6)$$

Equation (2.5) without the noise term is called the Cahn-Hilliard equation.

## 2.3 State of the art

The scaling hypothesis has been well-verified experimentally and numerically. But it has only been analytically proven in a small number of solvable simple cases, such as the one-dimensional ferromagnetic chain or the  $O(N)$  model in the large  $N$  limit. Verifying the scaling hypothesis, and computing the scaling functions, has been a longstanding challenge. Let us mention some of the strategies used to study phase ordering dynamics:

- *Scaling arguments.* Imposing the scaling hypothesis (without proving it) allows one to find useful results. One example we already mentioned is the determination of the  $t^{1/2}$  growth law for model A.
- *Exact results.* There are a few exactly solvable models of phase ordering dynamics. They are far from experimentally interesting systems, but give us some ideas that survive in more relevant models. In particular, they are the only cases where the dynamical scaling hypothesis has been proven. Examples of these models include the  $O(N)$  model with  $N \rightarrow \infty$  for both conserved and non-conserved dynamics [74], the one-dimensional Ising model with Glauber dynamics [75, 76] or the 1d-XY model [77].
- *Field theoretical approach.* A number of field-theoretical approaches to find an approximate form of the scaling functions of two-point and two-time correlations have been proposed but

none of them is fully successful [8]. Some of them rely on a path-integral description of stochastic processes. The procedure that allows the construction of the path integral associated with a given Langevin equation was developed by Martin, Siggia and Rose [78] and De Dominicis and Peliti [79] (a very useful review is [80]). From there, non-perturbative approaches like  $1/N$  expansions can be used [8].

- *Simulations in spin models.* Most of the analytical results are based on continuous models where the usual tools of differential analysis can be used. But other useful information can be obtained from Monte Carlo simulations in discrete spin models. The equivalence between both approaches relies on the fact that at a coarse-grained level, the order parameter of spin models take a continuous character and can be well described in terms of partial differential equations. Monte Carlo techniques are, *in principle*, well suited to study equilibrium properties but not out-of-equilibrium ones. Note that the power of Monte Carlo simulations relies on the ability to explore the phase space by performing non-physical movements. But due to the dynamical universality of coarsening, some Monte Carlo algorithms also belong to the dynamical universality classes discussed previously. In particular, kinetic spin models on the lattice with Glauber dynamics belongs to model *A*, and with Kawasaki dynamics, to model *B*.

## 2.4 Our work

The goal of our work is to compute the observables which describe the *geometry* of the coarsening dynamics of a  $2d$  system with a scalar order parameter. In particular, we will compute the scaling functions for the distributions of domain areas and boundary lengths. We will also describe the evolution of the morphology of the domains.

In the next chapters we will address the following issues:

- Prove the dynamical scaling hypothesis in  $d = 2$  curvature-driven coarsening.
- Discuss the role played by different initial conditions  $T_0$ .
- Discuss the role played by the working temperature  $T$ .
- Discuss the effects of weak disorder.
- Discuss the role played by conservation laws (model *A* vs. model *B*).
- Discuss the experimental applications of our results.



## Chapter 3

# Non-conserved dynamics

### 3.1 Introduction: Hull-enclosed areas and domain areas

In this chapter we present some exact results for the coarsening dynamics of a *non-conserved* scalar field in two dimensions. Furthermore, these results provide the first demonstration of the *dynamical scaling hypothesis* for this system. We will discuss the phase ordering dynamics from a geometrical point of view. The geometrical observables which we will study are the distributions of two characteristic areas, the domain area and the hull enclosed area, and their associated lengths, the domain perimeter and the hull perimeter.

In a spin system, a *domain* is defined as a *connected region* where the spins are aligned. The domain area is the number of spins belonging to the domain. In a continuous model, a domain is defined as a connected region where the order parameter  $\phi(\vec{x}, t)$  takes the same sign, the domain area being the surface of this region. Note that *a domain can have holes*. *Hulls* are the domain boundaries. A *hull enclosed area* is defined as the full interior of a domain boundary, irrespective of there being other interfaces and thus regions of the opposite phase within. *A hull enclosed area has no holes*. The number of hulls is always equal to the number of domains because one can associate a hull to each domain: the hull corresponding to the *external* border of the domain. See Fig. 3.1 for a sketch explaining these definitions.

Naively, one may imagine that coarsening is basically due to the coalescence of small domains that form larger ones. However, in two dimensional curvature driven coarsening, *coalescence processes are avoided*. All the interfaces move with a velocity that is proportional to the local curvature. This velocity points in the direction of decreasing the curvature; therefore, *interfaces disappear independently of one another*. This is the reason why we first focused on the statistics of hull enclosed areas, quantities that depend on the motion of a *single* interface, and not on the statistics of the more natural domain areas.

Hull enclosed and domain areas have distributions that, at late times after the quench exhibit, according to the scaling hypothesis, the scaling form  $n(A, t) = t^{-2}f(A/t)$ , where  $n(A, t)dA$  is the number of hulls (domains) per unit area with area in the range  $(A, A + dA)$ . The argument of the scaling function arises from the fact that the characteristic length scale is known to grow as  $t^{1/2}$ , so the characteristic area (of hulls and domains) grows as  $t$ . The scaling function  $f(x)$  will be different for domains and hulls. The prefactor  $t^{-2}$  follows from the fact that there is of order one hull (or domain) per scale area. In this chapter we derive these scaling forms from first principles (i.e. without recourse to the scaling hypothesis), and determine explicitly the scaling functions. We will also discuss the domain-perimeter and hull *lengths*, which are themselves distributed quantities related in a non-trivial manner to their corresponding areas.

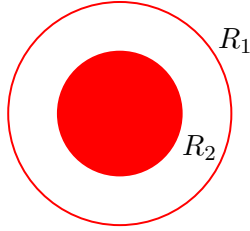


Figure 3.1: A sketch of a configuration with two concentric and circular interfaces with radius  $R_1$  and  $R_2$  is shown to illustrate the definition of hull enclosed and domain areas as well as hull and domain-wall perimeters. This configuration has two hull enclosed areas  $A_h^{(1)} = \pi R_1^2$  and  $A_h^{(2)} = \pi R_2^2$  and two domains with areas  $A_d^{(1)} = \pi(R_1^2 - R_2^2)$  and  $A_d^{(2)} = \pi R_2^2$ . There are two hulls with length  $p_h^{(1)} = 2\pi R_1$  and  $p_h^{(2)} = 2\pi R_2$ , and two domain walls with length  $p_d^{(1)} = 2\pi(R_1 + R_2)$  and  $p_d^{(2)} = 2\pi R_2$ .

The structure of this chapter is as follows. In Sect. 3.2 we present the equation which governs the dynamics of the interfaces after a quench to  $T = 0$ . In Sect. 3.3 we obtain the exact evolution equation for each hull enclosed area,  $A_h(t)$ , and the exact distribution  $n_h(A, t)$  at any time during the coarsening dynamics. In Sect. 3.4 we focus on the distribution of domain areas  $n_d(A, t)$ . The evolution of domain areas is much more complicated than the hull enclosed ones, because domains areas do not evolve independently one from each other. An approximate analytical result is obtained for  $n_d(A, t)$  and its accuracy is checked using numerical simulations. In Sect. 3.5 we discuss the effects on the area distributions of quenching the system to a temperature  $T \neq 0$ . Section 3.6 is devoted to the analysis, both analytical and numerical, of the geometry of hulls and domain walls during the dynamics. We conclude in Sect. 3.7.

Along the discussion we will present in parallel analytical results with their simulations counterparts. Let us present briefly the details of the simulations. We carried out Monte Carlo simulations on the  $2d$  square-lattice Ising model ( $2dIM$ ) with periodic boundary conditions using a heat-bath algorithm with random sequential updates. All data have been obtained using systems with size  $L^2 = 10^3 \times 10^3$  and  $2 \times 10^3$  runs using independent initial conditions. Domain areas are identified with the Hoshen-Kopelman algorithm [81]. In order to identify the hull-enclosed ones, we developed an algorithm which performs a directed walk along each domain wall of the system. The detailed description of this algorithm is given in Appendix A.

### 3.2 Coarsening at $T = 0$ . The Allen-Cahn equation.

As explained in the previous chapter, the coarsening dynamics following a quench to any temperature lower than the critical one is essentially the same than in a quench to  $T = 0$ . It is therefore natural to start our discussion with the case  $T = 0$ .

Our analytical results are obtained using a continuum description of domain growth in which the non conserved order parameter is a scalar field,  $\phi(\vec{x}, t)$ , defined on a  $d$ -dimensional space. Its evolution is determined by the time-dependent Ginzburg-Landau equation or model A dynamics (see Sect. 2.2):

$$\frac{\partial \phi(\vec{x}, t)}{\partial t} = \nabla^2 \phi(\vec{x}, t) - \frac{\delta V(\phi)}{\delta \phi(\vec{x}, t)} + \xi(\vec{x}, t). \quad (3.1)$$

where the potential  $V$  is a symmetric double well, with  $V(\phi \rightarrow \pm\infty) = \infty$  and two minima at  $\pm\phi_0$ .

$\xi$  is a Gaussian distributed random scalar field with zero mean and correlation

$$\langle \xi(\vec{x}, t) \xi(\vec{x}', t') \rangle = 2T \delta^d(\vec{x} - \vec{x}') \delta(t - t') . \quad (3.2)$$

The low-temperature ordering dynamics from a disordered initial condition corresponds to the growth of ordered domains of the two equilibrium states,  $\phi(\vec{x}, t) = \pm\phi_0$ , separated by interfaces.

Using the evolution equation (3.1) at *zero temperature*, Allen and Cahn [82] showed that in any dimension  $d$  the velocity,  $v$ , of each element of a domain boundary is proportional to the local interfacial mean curvature,  $\kappa$  (for a pedagogic derivation of the Allen-Cahn result see [8]),

$$v = -\frac{\lambda_h}{2\pi} \kappa . \quad (3.3)$$

$\lambda_h$  is a material constant with the dimensions of a diffusion constant, and the factor  $1/2\pi$  is for later convenience. The velocity is normal to the interface and points in the direction of reducing the curvature. The dynamics is then purely curvature driven at zero temperature. Note that the advantage of the Allen-Cahn construction is to pass from Eq. (3.1), which describes the *dynamics of the order parameter* to Eq. (3.3) which describes the *dynamics of the interfaces*.

### 3.3 Exact result for the distribution of hull-enclosed areas

#### 3.3.1 Equation of evolution for hull-enclosed areas

In two dimensions we can quickly deduce the time-dependence of the area contained within any finite hull. Integrating Eq. (3.3) around a hull:

$$\frac{dA_h}{dt} = \oint v dl = -\frac{\lambda_h}{2\pi} \oint \kappa dl \quad (3.4)$$

where  $dl$  is the element of length.

We need to compute the integral in the last member of Eq. (3.4). But that is an easy task using the Gauss-Bonnet theorem, which states the following: suppose  $M$  is a compact two-dimensional manifold with boundary  $\partial M$ . Let  $K_g$  be the Gaussian curvature of  $M$ , and let  $\kappa$  be the geodesic curvature of  $\partial M$ . Then

$$\int_M K_g dS + \oint_{\partial M} \kappa dl = 2\pi\chi(M), \quad (3.5)$$

where  $\chi(M)$  is a topological invariant called the Euler characteristic of the manifold. As we are interested in a  $2d$  flat surface without any internal hole (remember than we are studying the hull enclosed area),  $K_g = 0$  and  $\chi(M) = 1$ . Then, the integral of the curvature over the interface is just

$$\oint_{\partial M} \kappa dl = 2\pi . \quad (3.6)$$

Equation (3.4) reduces to

$$\frac{dA}{dt} = -\lambda_h \quad (3.7)$$

Integrating over time, with initial time  $t_i$ , we find

$$A_h(t, A_i) = A_i - \lambda_h(t - t_i) . \quad (3.8)$$

Therefore the distribution of hull-enclosed areas at any time during the evolution is

$$\begin{aligned} n_h(A, t) &= \int_0^\infty dA_i \delta(A - A_i + \lambda_h(t - t_i)) n_h(A_i, t_i) \\ &= n_h(A + \lambda_h(t - t_i), t_i) . \end{aligned} \quad (3.9)$$

In deriving this result we have implicitly assumed that a single domain cannot split into two, and that two domains cannot coalesce. A little thought shows that neither process is possible for two-dimensional curvature-driven growth since both processes require that two parts of a single domain boundary (for splitting) or parts of two different domain boundaries (for coalescence) come together and touch. But it is clear that the curvature driven dynamics always acts to prevent this happening, since the velocities of the domain boundaries at the incipient contact point are in opposite directions.

From Eq. (3.9) it is clear that *if we know the distribution  $n_h(A, t_i)$  at the initial time, we will know the distribution  $n_h(A, t)$  at any time during the evolution.*

### 3.3.2 Initial distributions of hull-enclosed areas

Right before the quench, the system is in *equilibrium* at some initial temperature  $T_0$ . We will consider quenches to  $T = 0$  from two different equilibrium initial states:  $T_0 = T_c$  and  $T_0 \rightarrow \infty$ . While the equilibrium distribution for hull enclosed areas at  $T_c$  has been already exactly computed by Cardy and Ziff [83], there are no exact results available for  $T_0 \rightarrow \infty$ . But, as we will discuss later, we can exploit the fact that the infinite temperature equilibrium state is closely related to the critical percolation point, for which the distribution of hull enclosed areas was also exactly computed in [83].

The equilibrium hull enclosed area distributions at percolating criticality and Ising criticality in two dimensions are [83]:

$$n_h(A, 0) \sim \begin{cases} 2c_h/A^2 , & \text{critical percolation,} \\ c_h/A^2 , & \text{critical Ising.} \end{cases} \quad (3.10)$$

These results are valid for  $A_0 \ll A \ll L^2$ , with  $A_0$  a microscopic area and  $L^2$  the system size.  $n_h(A, 0) dA$  is the number density of hulls per unit area with enclosed area in the interval  $(A, A+dA)$  (we keep the notation to be used later and set  $t = 0$ ). The adimensional constant  $c_h$  is a universal quantity that takes a very small value:  $c_h = 1/(8\pi\sqrt{3}) \approx 0.022972$ . The smallness of  $c_h$  plays an important role in the analysis of Sect. 3.4.

Let us discuss now the relation between  $T_0 \rightarrow \infty$  and the percolation critical point, first numerically and then with a physical argument.

We mimicked an instantaneous quench from  $T_0 \rightarrow \infty$  by using random initial states with spins pointing up or down with probability 1/2. Assigning site occupation to up spins and vacant sites to down spins the infinite temperature initial condition can be interpreted as a percolation problem at  $p = 0.5$  and thus below the percolation transition  $p_c = 0.5927$  in a square bi-dimensional lattice. Even if initially away from criticality, in a few MC steps the hull enclosed area distribution becomes the one in Eq. (3.10), as shown in Fig. 3.2. The initial distribution lacks large areas, there being almost none with  $A > 10^3$ , and the tail of  $n_h$  falls off too quickly well below the critical percolation curve. In a few time steps large structures appear and the tail of the distribution approaches the expected form at critical percolation. Simultaneously, the weight at small areas diminishes and the curve progressively gets flatter.

It is intuitively clear why this must be so. Soon after the quench, the characteristic length scale  $R(t)$  becomes substantially larger than the lattice spacing. If the system is coarse-grained on



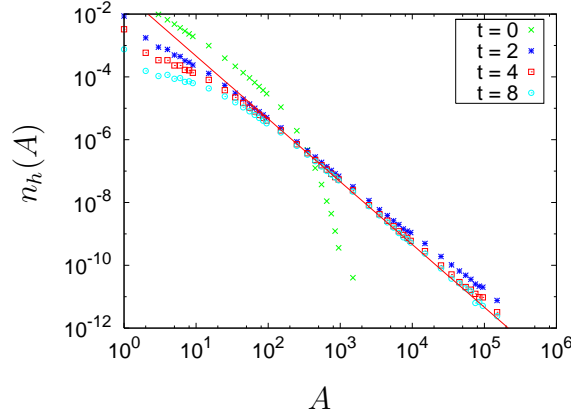


Figure 3.2: Early evolution of the infinite temperature initial condition. In a few MC steps the hull enclosed area distribution reaches the one of critical percolation (3.10), whose slope, -2, is shown by the straight line.

the domain typical scale,  $R(t)$ , it will look completely disordered. When  $R(t)$  is large compared to the lattice spacing, the disorder will be that of continuum percolation, for which the critical density is one half by symmetry in two dimensions [84, 85, 86, 87]. It follows that the coarsening system will be asymptotically at percolative criticality, *i.e. the dynamics self-tunes the system to percolative criticality in two dimensions* [provided  $R(t)$  remains much smaller than the system size]. The data show that, as far as the hull area distributions are concerned, this only takes a few Monte Carlo steps in practice. During these few steps many small domains coalesce to form larger ones meaning that the dynamics is dominated by processes that are not taken into account by Eq. (3.3). The physical argument explained in this paragraph has also been used very recently in [88] to analytically determine the probability to reach a metastable strip state in the two-dimensional Ising ferromagnet.

We can look at this from another perspective in the context of the continuum model. Consider a random field  $\phi(\vec{x})$ , symmetrically distributed with respect to zero, with bounded variance and two-point correlator  $C(r) = \langle \phi(\vec{x})\phi(\vec{x} + \vec{r}) \rangle$  with  $r = |\vec{r}|$ . The zero contour lines of this field can be imagined to divide the plane into regions of black and white with each contour line forming a boundary between black and white regions. Provided that  $C(r)$  falls off faster than  $r^{-3/4}$  for large  $r$ , this problem is known to belong to the standard percolation universality class [85]. If we now identify  $\phi(\vec{x})$  with the order parameter field when well-defined domain walls (the zero contour lines) have formed, we see that the resulting domain structure corresponds to critical percolation.

### 3.3.3 Distribution of hull-enclosed areas during the dynamics

Inserting the initial distributions (3.10) into Eq. (3.9) for  $t \gg t_i$  one immediately recovers:

$$n_h(A, t) = \frac{2c_h}{(A + \lambda_h t)^2}, \quad T_0 \rightarrow \infty, \quad (3.11)$$

$$n_h(A, t) = \frac{c_h}{(A + \lambda_h t)^2}, \quad T_0 = T_c, \quad (3.12)$$

in the limit  $A_0 \ll A \ll L^2$ , *i.e.* for hull enclosed areas much larger than microscopic areas but much smaller than the area of the system.

Equations (3.11) and (3.12) have the expected scaling forms  $n_h(A, t) = t^{-2}f(A/t)$  corresponding to a system with characteristic area proportional to  $t$  or characteristic length scale  $R(t) \sim t^{1/2}$ , which is the known result if scaling is *assumed* [8]. Here, however, we do not *assume* scaling – rather, it emerges from the calculation. Furthermore, the conventional scaling phenomenology is restricted to the ‘scaling limit’:  $A \rightarrow \infty$ ,  $t \rightarrow \infty$  with  $A/t$  fixed. Equations (3.11) and (3.12), by contrast, are valid whenever  $t$  is sufficiently large and  $A \gg A_0$ . This follows from the fact that, for large  $t$ , the forms (3.11) and (3.12) probe, for any  $A \gg A_0$ , the tail (i.e. the large- $A$  regime) of the Cardy-Ziff results, which is just the regime in which the latter is valid. The restriction  $A \gg A_0$  is needed to justify the use of Eq. (3.3), which breaks down when the reciprocal of the curvature becomes comparable with the width of a domain wall.

The averaged area enclosed by a hull is then given by

$$\langle A \rangle(t) = \frac{\int dA' A' n_h(A', t)}{\int dA' n_h(A', t)} \quad (3.13)$$

$$\sim \lambda_h t \quad (3.14)$$

with a time-independent prefactor that behaves as  $(A_0^2 \ln L^2)$  for large system sizes. The reason for the divergent prefactor in the infinite size limit is that a site can belong to several hulls.

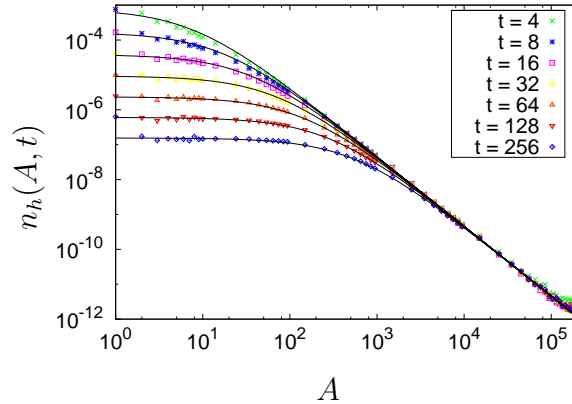


Figure 3.3: Number density of hull enclosed areas per unit system area for the zero-temperature dynamics of the 2dIM at seven times evolving from an infinite temperature initial condition. The lines represent Eq. (3.11) with  $c_h = 1/8\pi\sqrt{3}$  and  $\lambda_h = 2.1$ .

In Fig. 3.3 we show the time-dependent hull enclosed area distribution in double logarithmic scale, at seven different times, following a quench from  $T_0 \rightarrow \infty$ . The figure shows a strong time dependence at small areas and a very weak one on the tail, which is clearly very close to a power law. The curves at small areas move downwards and the breaking point from the asymptotic power law decay moves towards larger values of  $A$  for increasing  $t$ .

In Fig. 3.5 (right) we zoom on the small area region ( $A < 10^3$ ) where the time-dependence is clearer and we scale the data by plotting  $(\lambda_h t)^2 n_h(A, t)$  against  $A/\lambda_h t$  with  $\lambda_h = 2.1$ . We tried other time-dependent factors but  $\lambda_h t$  with this particular value of  $\lambda_h$  is the one yielding the best collapse of data at small areas,  $A_0 \ll A < \lambda_h t$ . For  $A$  larger than the ‘typical’ value  $\lambda_h t$  the time and  $\lambda_h$  dependence becomes less and less important. In Fig. 3.4 we show the data in their full range of variation in log-log form to test the prediction  $n_h(A, t) \sim A^{-2}$  for large  $A$ . The data are in remarkably good agreement with the prediction (3.11) – shown as a continuous curve in the figure

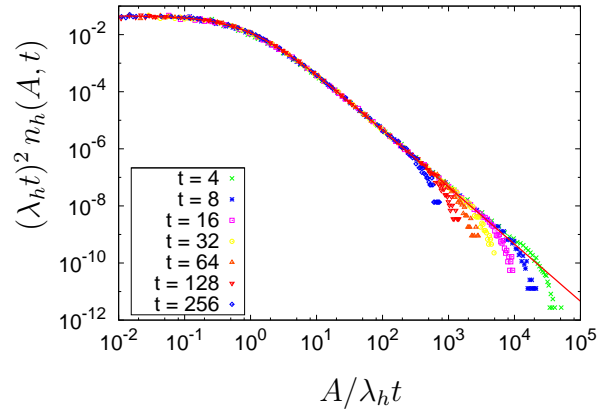


Figure 3.4: Number density of hull enclosed areas per unit system area for the zero temperature dynamics of the 2dIM evolving from an infinite temperature initial condition. The full line is the prediction (3.11) with  $c_h = 1/8\pi\sqrt{3}$  and  $\lambda_h = 2.1$ .

– over the whole range of  $A$  and  $t$ . The downward deviations from the scaling curve are due to finite-size effects. The latter are shown in more detail in Fig. 3.6, where we display the  $t = 16$  MCs results for several linear sizes. Finite size effects appear only when the weight of the distribution has fallen by many orders of magnitude (7 for a system with  $L = 10^3$ ) and are thus quite irrelevant. In the tail of the probability distribution function (pdf) the numerical error is smaller than the size of the data points. The nearly perfect agreement between the analytical theory and the data is all the more impressive given that the curvature-driven growth underlying the prediction (3.11) only holds in a statistical sense for the lattice Ising model [89]. Indeed, even at small values of  $A/\lambda_h t$ , where the lattice and continuous descriptions are expected to differ most, the difference is only a few percent.

It is clear that the evolution of the hull-enclosed area distribution follows the same ‘advection law’ (3.9), with the same value of  $\lambda_h$ , for other initial conditions. The evolution from a critical temperature initial condition is shown in the left panel of Fig. 3.5. A fit of the data at small areas yields the value of the parameter  $\lambda_h$  that, consistently with the analytic prediction, takes the same value  $\lambda_h = 2.1$ . In the right panel of Fig. 3.5, we compare the time-dependent hull enclosed area distributions for the initial conditions  $T_0 \rightarrow \infty$  and  $T_0 = T_c$  and we zoom on the behaviour of  $n_h(A, t)$  at small areas,  $A/\lambda_h t \leq 10$ . The two solid lines correspond to the numerator in  $n_h$  being equal to  $2c_h$  for infinite temperature initial conditions and  $c_h$  for critical Ising initial conditions. The difference between the numerical data for the two initial states is clear and it goes in the direction of the analytic prediction (a factor 2 difference in the constant).

Moreover, Eq. (3.11) applies to *any*  $T_0 > T_c$  equilibrium initial condition asymptotically. Equilibrium initial conditions at different  $T_0 > T_c$  show only a different transient behaviour: the closer they are from  $T_c$ , the longer it takes to reach the asymptotic law, Eq. (3.11). Fig. 3.7 shows the evolution of initial distributions, for  $T_c < T_0 < \infty$ . Both analytic predictions, for  $T_0 = T_c$  and  $T_0 = \infty$ , are shown as solid lines along with data for increasing times after a zero-temperature quench from  $T_0 = 2.5$ . In the first steps, the curve follows the one for critical initial conditions at small  $A/\lambda_h t$  and then departs to reach the one for infinite temperature initial conditions at large  $A/\lambda_h t$ . At longer times, the deviation from the critical initial condition line occurs at a smaller value of  $A/\lambda_h t$ . Initially the system has a finite, though relatively small, correlation length  $\xi(T)$ . Thermal fluctuations with linear size of the order of  $\xi$  and also significantly larger than  $\xi$  exist

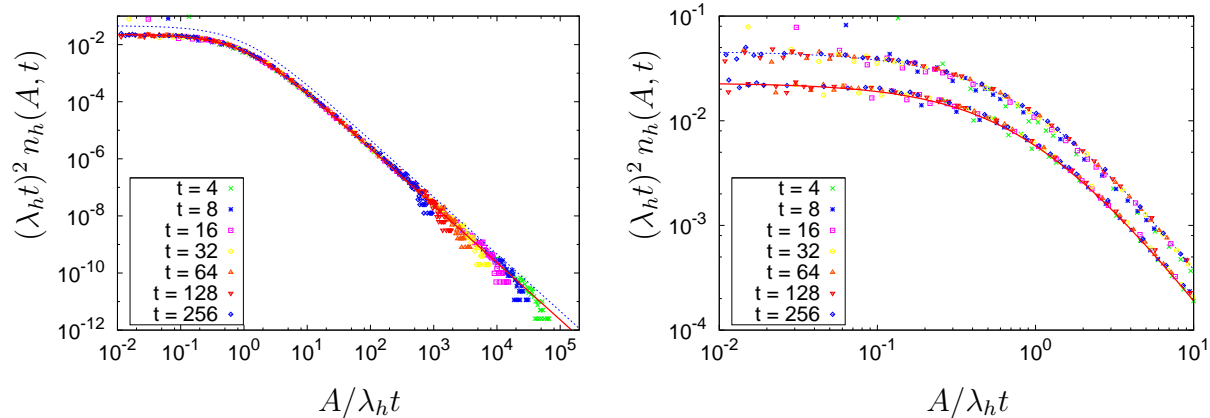


Figure 3.5: Number density of hulls per unit area for the zero-temperature  $2dIM$  evolving from critical initial conditions. The initial states are obtained after running  $10^3$  Swendsen-Wang algorithm steps. Left panel: the full (red) line is Eq. (3.12) with  $\lambda_h = 2.1$  which again yields the best fit of the data at small areas. For comparison we include with a dotted (blue) line the analytic prediction for an infinite temperature initial condition, i.e. Eq. (3.11). Right panel: more details on the influence of the initial conditions. The two data sets correspond to configurations taken at several times after a quench from  $T_0 \rightarrow \infty$  and  $T_0 = T_c$ . The solid lines are the analytic predictions (3.11), blue line, and (3.12), red line.

(see the discussion on the effect of thermal fluctuations in Sect. 3.5). Notice that  $\xi(T)$  does not correspond exactly to the size of geometric domains: thermal fluctuations are not perfectly described by domains of aligned spins, since not all of them are correlated. At any given temperature above  $T_c$ , fluctuations smaller than  $\xi(T)$  have the same statistics than those occurring at  $T_c$  and are thus described by Eq. (3.12), while domains larger than  $\xi(T)$  are not made of correlated spins and thus are described by the infinite temperature distribution, Eq. (3.11). As time increases, the system loses memory of the finite-size fluctuations and the asymptotic state does not differ from the infinite temperature one. Only when fluctuations exist over all spatial scales does the asymptotic state differ. This behaviour can be interpreted as follows. At fixed  $A/t$ , shorter times correspond to small areas while longer times are related to larger areas. Very small areas correspond to short linear sizes, of the order of the domains in the initial configurations, and thus reminiscent of critical ones. Instead large areas correspond to long linear sizes that are much longer than the correlation length and closer to the ones reached from the infinite temperature initial condition.

### 3.4 Distribution of domain areas

In the last section we have shown that the distribution of hull enclosed areas can be exactly computed, *because the area enclosed by a hull depends only on the motion of one single boundary*. This is no longer the case for the areas of the domains, for which the area will depend not only on the motion of its external wall but also on the motion of its internal walls. The computation of the domain area distribution is therefore much more difficult.

We will develop a similar strategy that the one used to obtain the hull-enclosed area distributions. First we try to write an equation of evolution for the domain areas and then we use equilibrium distributions, for which analytical results are also available.

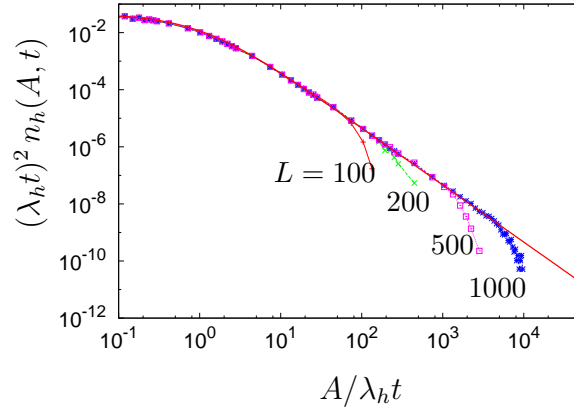


Figure 3.6: Finite size effects at  $t = 16$  MCs; four linear sizes of the sample are used and indicated by the data-points.

### 3.4.1 Initial condition for the distribution of domain areas

The distribution of *domain* areas at critical percolation is given by [42],

$$n_d(A, 0) \sim \frac{2c_d A_0^{\tau'-2}}{A^{\tau'}} , \quad \text{with } \tau' = \frac{187}{91} \approx 2.055 . \quad (3.15)$$

The quantity  $A_0$  can be interpreted as a microscopic area, and will be introduced at various points as a small-area cut-off. The quantity  $A_0^{\tau'-2}$  in Eq. (3.15) sets the units in such a way that  $[n_d] = A_0^{-2}$ . This result is also valid in the limit  $A_0 \ll A \ll L^2$ . Of course, the constants  $c_d$  and  $A_0$  are not separately defined, only the ratio  $c_d A_0^{\tau'-2}$ . In practice it is convenient to choose  $c_d$  to be the value appearing in the domain area distribution at general times (see discussion later).

In equilibrium at  $T_c$ , Stella and Vanderzande [90] computed the number density of domains with area  $A$

$$n_d(A, 0) \sim \frac{c_d A_0^{\tau-2}}{A^\tau} , \quad \text{with } \tau = \frac{379}{187} \approx 2.027 \quad (3.16)$$

in the large  $A$  limit. Janke and Schakel [91] confirmed this claim numerically finding  $\tau \approx 2.0269$ . The constants  $c_d$  were not computed in these works. Motivated by the Cardy-Ziff result for hull enclosed areas, we conjecture that the prefactor  $c_d$  in (3.16) is the same  $c_d$  (up to terms of order  $c_h^2$ ) as that appearing in the prefactor  $2c_d$  for critical percolation. We discuss this point in detail in the next section where we will also check it numerically.

For the following discussion is useful to include the small-area cut-off,  $A_0$ , in the initial number densities, transforming the denominators to  $(A + A_0)^2$  or  $(A + A_0)^{\tau, \tau'}$  for hull enclosed and domain areas, respectively.

We now present two exact sum rules. The first sum rule follows from the fact that the total domain area, per unit area of the system, is unity since each space point (or lattice site) belongs to one and only one domain. This gives

$$\int_0^\infty dA A n_d(A, 0) = 1 . \quad (3.17)$$

This sum rule yields (for  $T_0 = T_c$ ),

$$c_d = (\tau - 2)(\tau - 1) . \quad (3.18)$$

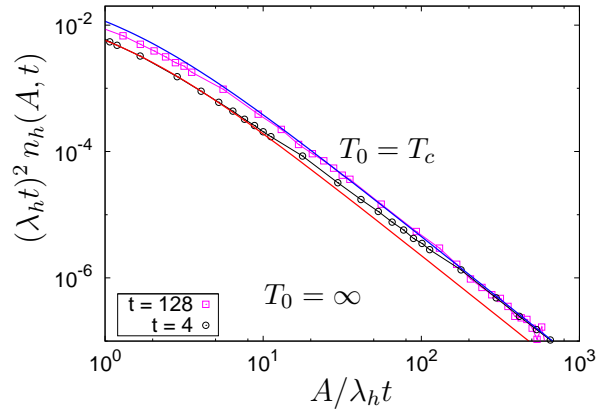


Figure 3.7: Effect of the initial condition temperature on the hull enclosed area distribution. The continuous lines are the analytic results for equilibrium initial conditions at  $T_0 = \infty$  and  $T_0 = T_c$ , bottom (red) and top (blue) lines, respectively. In between, we present numerical data for two different times given in the key after the quench from an initial state equilibrated at  $T_0 = 2.5$ .

The second sum rule follows from the fact that the total number of hulls  $N_h(0)$ , is equal to the total number of domains,  $N_d(0)$ , since each domain can be associated with a unique hull, namely the hull that forms its external boundary. This yields

$$\begin{aligned} N_d(0) &\equiv \int_0^\infty dA n_d(A, 0) \\ &= \int_0^\infty dA n_h(A, 0) \equiv N_h(0) . \end{aligned} \quad (3.19)$$

From there,

$$c_h = c_d/(\tau - 1) . \quad (3.20)$$

### 3.4.2 Evolution equation for domain areas during coarsening

We need to write an evolution equation to derive, at least approximately, the area  $A_d(t, A_i)$  at time  $t$  of a domain with initial area  $A_i$ .

Our strategy is to exploit the smallness of the parameter  $c_h \approx 0.023$ . Although  $c_h$  is a constant, we can exploit a formal expansion in  $c_h$  in the following sense. Since the total number of hulls per unit area is proportional to  $c_h$ , the number of interior hulls within a given hull is also proportional to  $c_h$ , and so on. This means that, in dealing with domains we need consider only the first generation of interior hulls, since the number of “hulls within hulls” is smaller by a factor  $c_h$ . With this approach, only one approximation – a kind of mean-field one on the number of first-generation hulls within a parent hull (see below) – is necessary.

The same line of reasoning shows that, in a hypothetical theory in which  $c_h$  can be treated as variable, the distinction between hulls and domains will disappear in the limit  $c_h \rightarrow 0$ . In this limit, therefore, the exponents  $\tau$  and  $\tau'$  must both approach the value 2, i.e. we can formally write  $\tau = 2 + O(c_h)$  and  $\tau' = 2 + O(c_h)$ . Furthermore, due to the factor 2 that appears in (3.11) but not in (3.12), the ratio  $(\tau' - 2)/(\tau - 2)$  must approach the value 2 in the limit  $c_h \rightarrow 0$ . The actual value of this ratio is  $187/91 = \tau' = 2.055$ , not very far from 2. Indeed the difference is of order  $c_h$  as expected.

We can use the same line of argument to discuss  $c_d$  and  $c_h$ . Since in the (hypothetical) limit  $c_h \rightarrow 0$ , hulls and domains become identical, it follows that in this limit one must have  $c_d \rightarrow c_h$ , i.e.  $c_d = c_h + O(c_h^2)$ .

Take a hull with enclosed area  $A_h$  at time  $t$ . This hull is also the external border of a domain, which may itself contain one or more ‘first level’ sub-domains whose external borders form the internal border (which may be disconnected) of the original domain. These external borders of the first level sub-domains are themselves ‘first generation’ hulls lying within the parent hull. These interior hulls can themselves have interfaces in their bulk separating domains of the reversed phase (higher generation hulls), see Fig. 3.8 where we show a sketch with this structure.

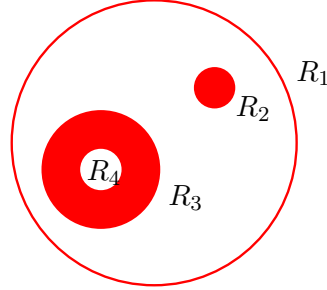


Figure 3.8: Sketch of a configuration with four circular hulls and domains. The parent hull has radius  $R_1$ . There are two first generation hulls with radius  $R_2$  and  $R_3$  and one second generation hull with radius  $R_4$ .  $\nu = 2$  in this example. The interior border of the external domain is disconnected and has two components.

Let us call  $\nu(t)$  the number of first-generation hulls within the parent one. It is clear that  $\nu(t)$  is non-negative definite, monotonically decreasing as a function of time and reaching zero at a given instant  $t_{max}$ , when all interior hulls disappear and  $A_d = A_h$  thereafter. One can estimate  $t_{max}$  from  $0 = A_h^{int}(t_{max}) = A_h^{int}(t_i) - \lambda_h(t_{max} - t_i)$ , which yields  $t_{max} - t_i = A_h^{int}(t_i)/\lambda_h$  where the index *int* indicates that we are studying here the first generation hull with maximal initial area (all others having already disappeared). It is clear that  $t_{max} - t_i$  is smaller but of the order of  $A_h(t_i)/\lambda_h$  where we replaced  $A_h^{int}(t_i)$  by the initial area of the parent hull:

$$(t_{max} - t_i) \lesssim \frac{A_h(t_i)}{\lambda_h}. \quad (3.21)$$

We wish to write a differential equation for the time-evolution of the parent domain area. It is clear that, at first order in  $dt$ :

$$A_d(t + dt) = A_d(t) - \lambda_h dt + \nu(t)\lambda_h dt \quad (3.22)$$

where the second term in the right-hand-side represents the loss in area due to the inward motion of the external domain-wall while the last term is the gain in area due to the outward motion of the first-generation internal domain-walls. This gives

$$\frac{dA_d(t)}{dt} = -\lambda_h [1 - \nu(t)]. \quad (3.23)$$

Differently from hull enclosed areas, that always decrease in size as time passes, domain areas can either diminish ( $\nu = 0$ ), increase ( $\nu > 1$ ) or remain constant ( $\nu = 1$ ) in time.

We cannot, of course, know the exact number of first generation hulls falling within a selected hull with enclosed area  $A_h$ . We can, however, estimate it with an upper bound obtained by counting all interior hulls and averaging over all parent hulls using  $n_h(A, t)$  derived in Sect. 3.3.3. Thus, we expect

$$\begin{aligned} \nu(t) &< \langle \nu(t) \rangle_{A_h(t)} \\ \langle \nu(t) \rangle_{A_h(t)} &\sim A_h(t) \int_0^{A_h(t)} dA n_h(A, t) \\ &= \frac{c_h A_h^2(t) [\lambda_h(t - t_i) + A_0]^{-1}}{[A_h(t) + \lambda_h(t - t_i) + A_0]}, \end{aligned} \quad (3.24)$$

where we include a small area cut-off,  $A_0$ , in the denominator of  $n_h$  and, for concreteness, we use the hull enclosed area distribution for critical Ising initial conditions. This equation can be further simplified if one uses that at time  $t$  the hull enclosed area we are interested in is given by

$$A_h(t) = A_h(t_i) - \lambda_h(t - t_i). \quad (3.25)$$

We have called here  $A_h(t_i)$  the initial area of the hull. Then

$$\langle \nu(t) \rangle_{A_h(t)} = \frac{c_h [A_h(t_i) - \lambda_h(t - t_i)]^2}{[\lambda_h(t - t_i) + A_0] [A_h(t_i) + A_0]}. \quad (3.26)$$

Note that, although we over-counted the interior hulls by including second-generation, third-generation, etc. hulls, the number of these is of order  $c_h^2$ ,  $c_h^3$ , ... respectively, so this treatment is exact to leading order in  $c_h$  except for the replacement of  $\nu(t)$  by its average over all first-generation hulls of the same area.

The most interesting cases are such that  $A_h(t_i) \gg A_0$ , otherwise the hull and domain areas are just identical or very similar. In these cases  $\langle \nu(t_i) \rangle_{A_h(t_i)} \sim c_h A_h(t_i)/A_0$ . Expression (3.26) has the following limiting values

$$\langle \nu(t) \rangle_{A_h(t)} \sim \begin{cases} \frac{c_h A_h(t_i)}{\lambda_h(t - t_i) + A_0}, & A_h(t_i) \gg \lambda_h(t - t_i), \\ ac_h, & A_h(t_i) \sim \lambda_h(t - t_i), \end{cases}$$

we used  $A_h(t_i) \gg A_0$  in the last case, and  $a$  is a numerical constant of order unity. The result is a very small quantity, of the order of  $c_h$ , in both cases. The remaining mathematical possibility,  $A_h(t_i) < \lambda_h(t - t_i)$  is not realized because  $A_h(t)$  cannot be negative.

While  $\nu(t)$  vanishes at  $t_{max}$ , see Eq. (3.21),  $\langle \nu(t) \rangle_{A_h(t)}$  is different from zero at all times. Thus, Eq. (3.26) cannot be used beyond the limit  $t_{max}$  when all internal hulls have already disappeared and it is no longer correct to replace  $\nu(t)$  by  $\langle \nu(t) \rangle_{A_h(t)}$ .

The analysis of infinite temperature initial conditions is identical to the one above with  $c_h$  replaced by  $2c_h$ . Thus,  $\langle \nu(t) \rangle_{A_h(t)}$  is expected to take twice the value it takes for critical Ising initial configurations.

We have checked the accuracy of this approximation numerically by counting the number of first generation internal hulls falling within each parent hull at different times. Figure 3.9 shows the results for the zero temperature evolution of the 2dIM starting from  $T_0 \rightarrow \infty$  and  $T_0 = T_c$  initial conditions. While at very short times one sees deviations between the numerical data and



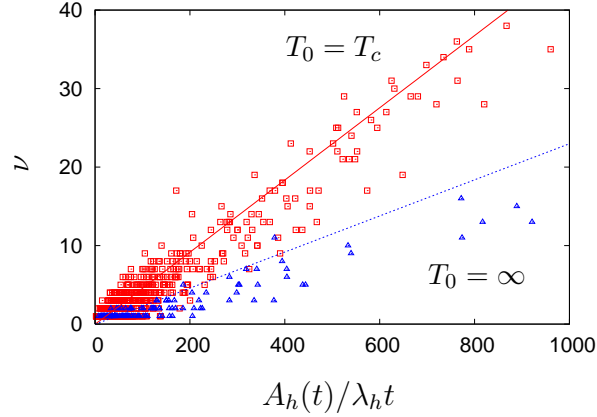


Figure 3.9: Comparison between  $\nu(t)$  and  $\langle \nu(t) \rangle_{A_h(t)}$  for the  $T = 0$  evolution of the  $2dIM$  with  $T_0 \rightarrow \infty$  and  $T_0 = T_c$  initial conditions. The measuring time is  $t = 64$  MCs. The curves are given by Eq. (3.24) in the limit  $t \gg t_i$  and  $A_h(t) \gg A_0$ , leading to the functional form  $\langle \nu(t) \rangle_{A_h(t)} = c_h x^2 / (1 + x) \sim c_h x$  when  $x \gg 1$ , with  $x = A_h(t) / \lambda_h t$  and  $\lambda_h = 2.1$ .

analytic prediction, the agreement between the two becomes very satisfactory for times of the order of  $t = 64$  MCs and longer, as shown in the figure.

If we now replace  $\nu(t)$  by  $\langle \nu(t) \rangle_{A_h(t)}$  given in Eq. (3.26), it is quite simple to integrate the differential equation (3.23). One finds

$$\begin{aligned} A_d(t) &= A_d(t_i) - \lambda_h(1 + 2c_h)(t - t_i) \\ &\quad + \frac{c_h A_0^2}{2[A_h(t_i) + A_0]} \left\{ \left[ 1 + \frac{\lambda_h(t - t_i)}{A_0} \right]^2 - 1 \right\} \\ &\quad + c_h[A_h(t_i) + A_0] \ln \left[ 1 + \frac{\lambda_h(t - t_i)}{A_0} \right]. \end{aligned}$$

Setting  $t = t_i$  one recovers  $A_d(t) = A_d(t_i)$  as required. In the natural cases in which  $A_h(t_i) \gg A_0$  and for long times such that  $\lambda_h(t - t_i) \gg A_0$  this expression can be rewritten as

$$\begin{aligned} A_d(t) &= A_d(t_i) - \lambda_h \left[ 1 + 2c_h - \frac{c_h \lambda_h(t - t_i)}{2 A_h(t_i)} \right] (t - t_i) \\ &\quad + c_h A_h(t_i) \ln \left[ 1 + \frac{\lambda_h(t - t_i)}{A_0} \right]. \end{aligned} \quad (3.27)$$

The factor in the second term

$$\lambda_d(t) \equiv \lambda_h \left[ 1 + 2c_h - \frac{c_h \lambda_h(t - t_i)}{2 A_h(t_i)} \right] \quad (3.28)$$

is a very weakly time-dependent function. Since  $t$  can take values between the initial time,  $t = t_i$ , and the maximum time before the first generation hull itself disappears,  $t_{max} = t_i + A_h(t_i) / \lambda_h$ ,  $\lambda_d(t)$  varies within the interval:

$$\lambda_h \left( 1 + \frac{3c_h}{2} \right) \leq \lambda_d(t) \leq \lambda_h(1 + 2c_h). \quad (3.29)$$

These bounds are indeed very close.  $\lambda_d$  takes a slightly higher value than  $\lambda_h$ ; it equals  $\lambda_h$  plus a small correction of order  $c_h$  (in practice,  $1.035 \lambda_h \leq \lambda_d \leq 1.046 \lambda_h$  using the analytic value for  $c_h$ ).

The coefficient in front of the logarithm,  $c_h A_h(t_i)$ , is  $\mathcal{O}(c_h)$ . The sum rules, imply  $c_h = c_d + \mathcal{O}(c_h^2)$ . Neglecting the higher order correction we can then replace  $c_h$  by  $c_d$ . The same applies to  $A_h(t_i)$ , which equals  $A_d(t_i)$  plus a term  $\mathcal{O}(c_h)$  that we can equally neglect. Thus  $A_h(t_i) \approx A_d(t_i) \equiv A_i$ . In this way we obtain

$$A_d(t, A_i) \simeq A_i - \lambda_d(t - t_i) + c_d A_i \ln \left[ 1 + \frac{\lambda_h(t - t_i)}{A_0} \right]. \quad (3.30)$$

### 3.4.3 Distribution of domain areas during coarsening

The distribution of domain areas will be given by

$$n_d(A, t) = \int_0^\infty dA_i \delta(A - A_d(t, A_i)) n_d(A_i, t_i). \quad (3.31)$$

Introducing in Eq. (3.31) the evolution equation for the domain area (3.30) and the initial domain distributions (3.15)-(3.16) with the microscopical area  $A_0$  as a small-area cut-off in the denominator of these initial distributions,

$$\begin{aligned} n_d(A, t) &\simeq c_d A_0^{\tau-2} \left\{ 1 + c_d \ln \left[ 1 + \frac{\lambda_d(t - t_i)}{A_0} \right] \right\}^{\tau-1} \\ &\times \left[ A + \lambda_d(t - t_i) + A_0 \left\{ 1 + c_d \ln \left[ 1 + \frac{\lambda_d(t - t_i)}{A_0} \right] \right\} \right]^{-\tau} \end{aligned} \quad (3.32)$$

where we have replaced  $\lambda_h$  by  $\lambda_d$  inside the logarithm, which is correct to leading order in  $c_h$ . Using the fact that  $c_d$  is very small and of the order of  $(\tau - 2)(\tau - 1) = (\tau - 2) + \mathcal{O}(c_h^2)$ , as implied by the sum rules, we can now exponentiate, correct to leading order in  $c_d$ , the logarithm in the numerator. The term containing  $c_d$  and  $A_0$  in the denominator is very small compared to  $A$ . We then obtain,

$$n_d(A, t) \simeq \frac{c_d [A_0 + \lambda_d(t - t_i)]^{\tau-2}}{[A + A_0 + \lambda_d(t - t_i)]^\tau}. \quad (3.33)$$

Finally we set the initial time,  $t_i$ , to zero and write the microscopic area,  $A_0$ , as  $\lambda_d t_0$  to obtain, for the time-dependent number density of domain areas,

$$n_d(A, t) \simeq \frac{c_d [\lambda_d(t + t_0)]^{\tau-2}}{[A + \lambda_d(t + t_0)]^\tau}, \quad (3.34)$$

The same sequence of steps for infinite-temperature initial conditions leads to the same form but with  $c_d$  replaced by  $2c_d$  and  $\tau$  replaced by  $\tau'$ . The effects of temperature are expected to appear only through the parameters  $\lambda_d$  and  $\lambda_h$  once thermal fluctuations are extracted from the analysis.

The averaged domain area is then given by

$$\langle A \rangle(t) = \frac{\int dA' A' n_d(A', t)}{\int dA' n_d(A', t)} = \frac{1}{N_d(t)} \quad (3.35)$$

$$\sim \lambda_d t. \quad (3.36)$$

Let us now check numerically the prediction for the distribution of domain areas Eq. (3.34). In Fig. 3.10 we display the number density of domain areas in the scaled form for two initial conditions,

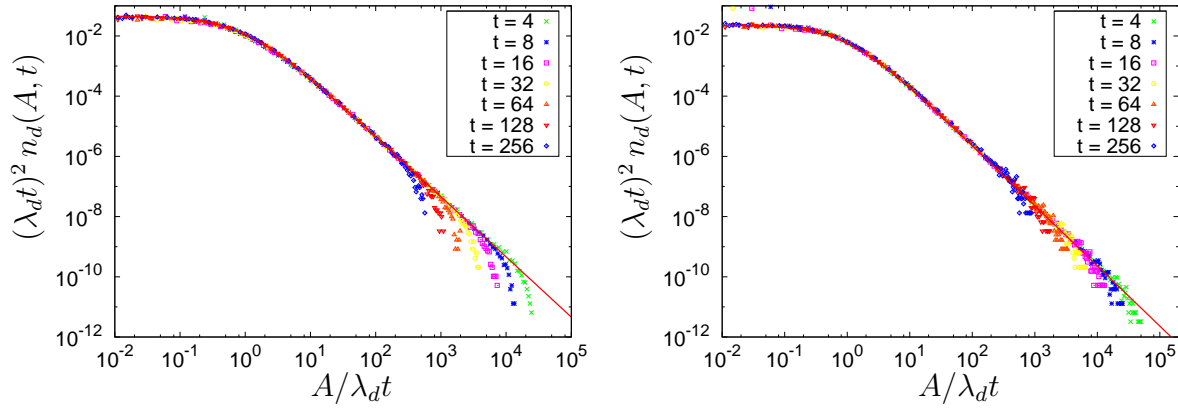


Figure 3.10: Number density of domains per unit area for the zero-temperature  $2dIM$  evolving from  $T_0 \rightarrow \infty$  (left) and  $T_0 = T_c$  (right) initial conditions. In both figures the spanning clusters have been extracted from the analysis (compare with Fig. 3.11 where we include them). The full (red) line represents Eq. (3.34), with  $c_d = 0.025$  and  $\tau' = 2.055$  (left),  $c_d \rightarrow c_d/2$  and  $\tau = 2.027$  (right), and  $\lambda_d = 2.1$  in both cases.

$T_0 \rightarrow \infty$  and  $T_0 = T_c$ , after removing any spanning domain from the statistics. For comparison, in Fig. 3.11, the same distributions with the spanning domains are shown. As done for the hull enclosed areas we fit the parameter  $\lambda_d$  by analysing the behaviour at small areas,  $A < \lambda_d t$ , and we find, once again that  $\lambda_d = 2.1$  yields the best collapse of data (as predicted from Eq. 3.29).

Both sets of figures, 3.10 and 3.11, exhibit finite size effects in the tail of the distributions, where the number of domain areas has already decreased by several orders of magnitude. As for the hull enclosed areas, the point where these finite size effects cause the deviation from the collapsed curve moves towards the right as the system size increases, becoming less and less relevant. In Fig. 3.10, large domain areas (violating the limiting condition  $A \ll L^2$ ) that would nonetheless be accounted for in an infinite system are here removed since they span the system in one of the directions, leading to the downward bending of the distribution. On the other hand, in Fig. 3.11, when counting these domains, they are chopped by the system boundaries, thus contributing to the distribution in a region shifted to the left, accounting for the bumps seen in the figure.

### 3.5 Effect of the working temperature

Up to now we have considered quenches to a zero working temperature. In this section we investigate the effect of having a finite temperature on the dynamics.

The arguments in previous sections rely on the  $T = 0$  Allen-Cahn equation (3.3). Temperature fluctuations have a two-fold effect. On one hand they generate *equilibrium thermal domains that are not related to the coarsening process*. On the other hand *they roughen the domain walls thus opposing the curvature driven growth and slowing it down*.

As explained in Sect. 2.1, renormalization group treatments of domain growth dynamics have led to the idea that a  $T = 0$  fix point controls the domain growth for all  $T < T_c$ , i.e. that thermal fluctuations are irrelevant to the asymptotic dynamics of the ordering system, their contribution being limited primarily to the renormalization of temperature-dependent prefactors. For the distribution of domain areas and hull enclosed areas, one may expect that *once equilibrium thermal domains are subtracted* (hulls and domains associated to the coarsening process are correctly iden-

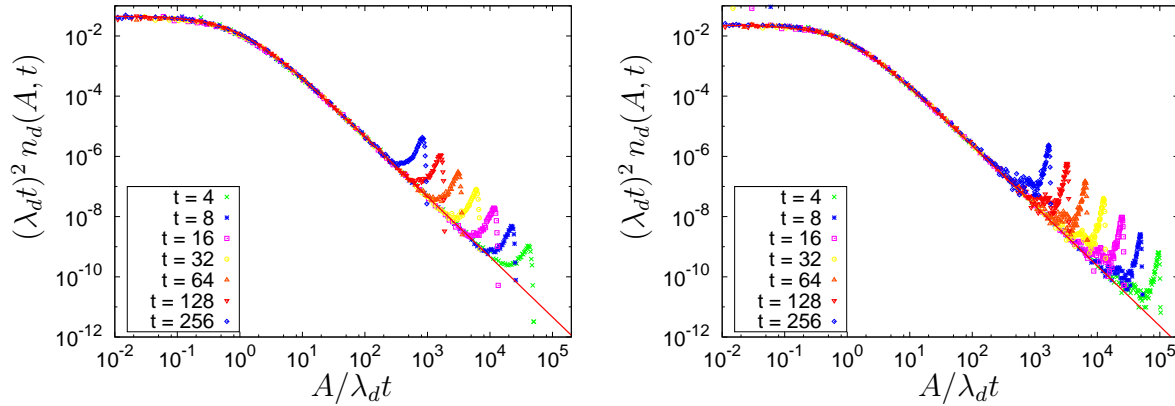


Figure 3.11: The same as Fig. 3.10, but with the spanning domains included in the statistics. Notice that due to the finiteness of the lattice, the actual area of these spanning domains are smaller than the value they would have on an infinite system, generating the overshoot of the distribution for values of  $A$  close to  $L^2$ . The larger is the system, the more to the right these peaks are localized.

tified) the full temperature dependence enters only through the values of  $\lambda_h$  and  $\lambda_d$ , which set the time scale.

Let us discuss the particular case of domain areas. The first step is to identify the temperature dependence of the parameter  $\lambda_d$ . The simplest and most direct way to do this is to use the scaling hypothesis and analyze the behaviour of the spatial correlation

$$\begin{aligned}
 C(r, t) &\equiv \frac{1}{N} \sum_{i=1}^N \langle s_i(t) s_j(t) \rangle_{|\vec{r}_i - \vec{r}_j| = r} \\
 &\sim m^2(T) f\left(\frac{r}{R(t)}\right),
 \end{aligned} \tag{3.37}$$

where  $m(T)$  is the equilibrium magnetization density and  $a \ll r \ll L$  and  $t_0 \ll t$ . The correlation is defined in such a way that  $C(0, t) = 1$ . Using  $R(t) \sim [\lambda_d(T)t]^{1/2}$ , the  $T$ -dependence of  $\lambda_d$  can be estimated either by collapsing all curves or by studying the value of  $r$  at which  $C(r, t) = 1/2$ . The resulting  $\lambda_d(T)$  obtained using these two prescriptions is shown in Fig. 3.12.  $\lambda_d(T)$  is a monotonically decreasing function of temperature, starting at  $\lambda_d(T = 0) = 2.1$  and falling-off to zero at  $T_c$ . These results are consistent with the evaluation of  $\lambda_{d,h}(T)$  from the analysis of  $n_{d,h}(A, t)$ , see below.

Assuming that  $\lambda_d$  vanishes at  $T_c$  one can derive the way in which it does with a simple argument. We require that the coarsening law for coarsening below  $T_c$ , namely  $R(t) \sim [\lambda(T)t]^{1/2}$ , match critical coarsening at  $T_c$ , viz.  $R(t) \sim t^{1/z}$  with  $z$  the dynamic exponent, for  $T \rightarrow T_c$ . Near (but just below)  $T_c$  the coarsening length grows as  $\xi^{-a}(T)t^{1/2}$  as long as  $R(t) \gg \xi(T)$  with  $\xi(T)$  the equilibrium correlation length. For  $R(t)$  comparable with  $\xi(T)$ , this has to be modified by a function of  $R(t)/\xi$  and, since  $R(t) \sim t^{1/z}$  at  $T_c$ , we can write

$$R(t) \sim \xi^{-a}(T)t^{1/2} f\left(\frac{t}{\xi^z(T)}\right). \tag{3.38}$$

In the limit  $\xi(T) \rightarrow \infty$ , the  $\xi$ -dependence must drop out. In order to cancel the time dependence at large times, one needs  $f(x) \sim x^{1/z-1/2}$  for  $x \rightarrow \infty$ . This yields  $R(t) \sim t^{1/z}$ , which fixes the

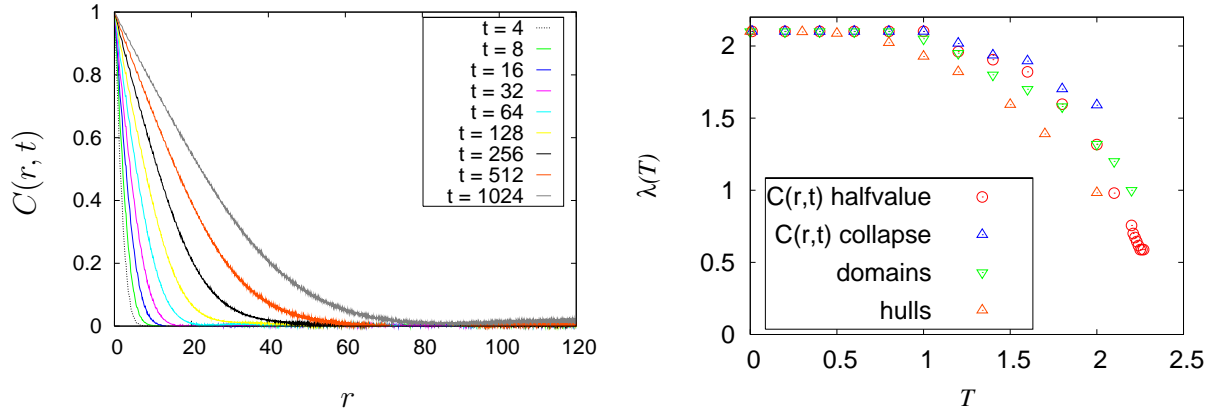


Figure 3.12: Left panel: spatial decay of the equal-time correlation, Eq. (3.37), at fixed  $T = 0$  and several different times  $t$ . Right panel: the  $T$  dependence of the parameters  $\lambda_{d,h}$ . Two sets of data points are extracted from the analysis of the correlations shown in the left panel. The data named half-value are obtained from  $C(r, t) = 1/2$  and the data named collapse from collapsing the curves on the range  $r \gg a$ . The two other sets are obtained from fitting  $n_{d,h}(A, t)$  with  $\lambda_{d,h}(T)$  as free parameters.

exponent ‘ $a$ ’ as  $a = (z - 2)/2$ , giving  $\lambda(T) \sim \xi^{-2a}(T) \sim (T_c - T)^{\nu(z-2)}$ . Inserting the exact value  $\nu = 1$  and the numerical value  $z = 2.15(2)$  [92] implies

$$\lambda_d(T) \sim (T_c - T)^{0.15}. \quad (3.39)$$

Note that we are matching two nonequilibrium growth laws (the one below  $T_c$  and the one at  $T_c$ ) not an equilibrium and a nonequilibrium one. The data in Fig. 3.12 are still far from the critical region where this small power-law decay should show up.

We have already discussed *the effects of temperature on the coarsening domains*. But, as explained before, *another effect of the temperature is to create small islands of reversed spins inside the coarsening domains, which correspond to thermal equilibrium fluctuations*. In Fig. 3.13 the raw data at  $t = 128$  MCs is shown for four working temperatures. Upward deviations with respect to the result of zero working temperature are prominent in the small areas region of the figure, and increase with temperature. In Fig. 3.14 (left) we display the raw data at the working temperature  $T = 1.5$ , for several times. Notice that although the curves move downwards, the small area region becomes time independent. This region also fails to collapse (right) with the proposed scaling using the temperature dependent values of  $\lambda_d(T)$ . The reason is that the distribution counts thermal equilibrium domains, that is to say, fluctuations that are present in an equilibrated sample at the working temperature, but are not due to the coarsening process. Thus, these fluctuations should be identified and eliminated from the statistics. We tried to apply the method introduced by Derrida [93], and extended by Hinrichsen and Antoni [94], to eliminate thermal domains, but the results were not satisfactory, as not all of them could be eliminated. Thus, instead of removing each thermal domain, we tried to directly remove their contribution to the distributions by simulating samples in equilibrium at the working temperature, starting with a fully magnetized state, and computing the number density of thermal domain areas. These data are shown with a black line in Fig. 3.15 and 3.16. Surprisingly enough, thermal fluctuations generate areas that are larger than one would have naively expected. Equilibrium arguments suggest that the averaged area of thermally generated domains scale as  $A_T \sim \xi^2(T)$  with  $\xi(T)/p_0 \sim f^-(1 - T/T_c)^{-\nu}$ ,  $\nu = 1$  and

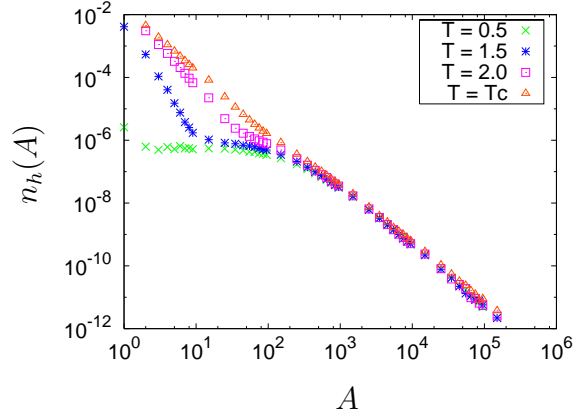


Figure 3.13: The number density of hull enclosed areas after  $t = 128$  MCs at the working temperatures  $T = 0.5, 1.5, 2$  and  $T = T_c$ .

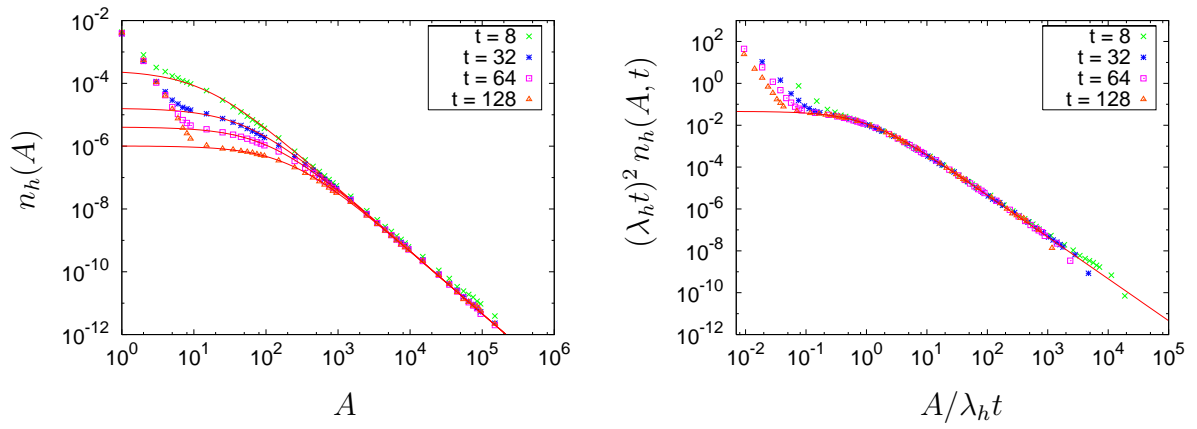


Figure 3.14: The number density of hulls for  $T = 1.5$  after different times (left) and the scaling of these data points (right)

$f^- = 0.18$  [95]. This estimate yields, for example,  $A_T \sim 4A_0$  at  $T = 1.5$  ( $p_0$  and  $A_0$  are respectively the length and area associated to the lattice step). In equilibrium at this temperature the average size of the domains found numerically is  $\langle A_T \rangle \sim 1.5A_0$ . However, the probability distribution of thermal areas has a non-negligible weight – as compared to the one of coarsening domains – that goes well beyond this value. For example, in Figs. 3.15 and 3.16 we see that the crossover between the thermal area distribution and the coarsening area distribution occurs at  $A \sim 10A_0$ .

In Fig. 3.15 we also present data for the dynamic distribution at three different times, and compared with the analytic prediction using  $\lambda_d(T)$  estimated from the analysis of the global spatial correlation, see Fig. 3.12. We conclude that the agreement between analytic prediction and numerical results is very good in the region in which the thermal domains are subdominant.

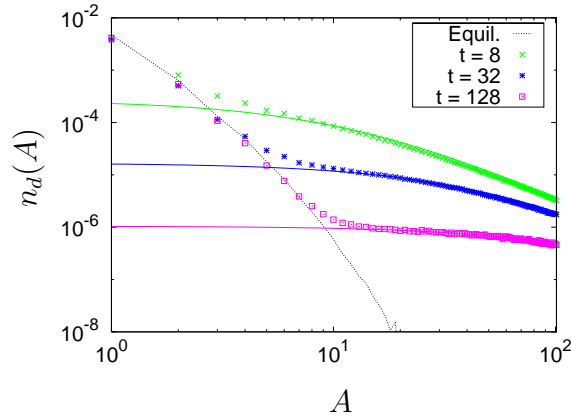


Figure 3.15: The contribution of ‘thermal domains’ obtained by simulating an equilibrated sample at the working temperature  $T = 1.5$ , along with the evolution of the distribution of domain sizes after a quench to the same temperature.

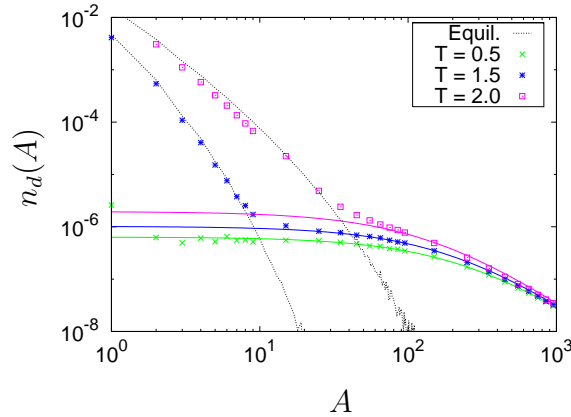


Figure 3.16: Zoom on the number density of domain areas at  $t = 128$  MCs at three working temperatures given in the key. The black lines are the equilibrium distributions at  $T = 1.5$  and  $T = 2$  and the other lines (pink, blue and green) represent our analytic prediction for the coarsening areas.

One can also use the results in Fig. 3.16 to estimate the value of  $\lambda_d(T)$ . Indeed, a fit of the numerical data for areas larger than the value at which the equilibrium thermal contribution

deviates from the dynamic one, yields the values of  $\lambda_d(T)$  [and  $\lambda_h(T)$ ] shown in Fig. 3.12. This analysis allows us to extract independent predictions for  $\lambda_d(T)$  and  $\lambda_h(T)$ . We find that the qualitative  $T$ -dependence is the same. As regards the absolute values, the numerical data yield  $\lambda_h(T) \leq \lambda_d(T)$  on the whole range. Note that the analytic prediction already suggested  $\lambda_d = \lambda_h + \mathcal{O}(c_h)$ .

### 3.6 Statistics of perimeters and fractal properties

The analytical arguments described in the previous sections can be extended to study the distributions of boundary lengths. In this section we present the analytical predictions for these functions together with numerical results that confirm them. We study two types of domain boundaries: those associated to the hulls and those associated to the domains. The perimeter of a domain is given by the sum of its external perimeter (hull perimeter) plus the perimeter of its internal borders.

#### 3.6.1 Initial conditions

In equilibrium at  $T_0 = T_c$ , we find numerically (see the left panel of Fig. 3.17) that the domain areas and their corresponding boundaries are related by

$$A_h \sim p^{\alpha_h^i}, \text{ with } \alpha_h^i \approx 1.47 \pm 0.1,$$

$$A_d \sim \begin{cases} p^{\alpha_d^{i>}}, & \alpha_d^{i>} \approx 1.14 \pm 0.1 \text{ for } p \gtrsim 50, \\ p^{\alpha_d^{i<}}, & \alpha_d^{i<} \approx 1.47 \pm 0.1 \text{ for } p \lesssim 50, \end{cases}$$

in the whole range of variation. The superscript  $i$  is used to stress that these values are measured in equilibrium, we will study the dynamical ones in the next section. Note that the longest lengths,  $p \approx 10^3 - 10^4$  may be affected by finite size effects given that the linear size of the simulating box is  $L = 10^3$ . The spanning clusters are not counted because their perimeters would be severely underestimated due to the periodic boundary condition. The exponent  $\alpha_d^{i<} \approx 1.47 \pm 0.1$  is consistent with the numerical result in [96]. The difference between the small and large  $p$  regimes in the relation between areas and perimeters for the domains is due to the existence of holes in the large structures. The small domains and hulls are just the same objects because the former do not have holes within.

Numerically, (see the right panel of Fig. 3.17), we find that the number densities of hull and domain lengths at critical Ising conditions are

$$n_h(p, 0) \sim p^{-\zeta_h^i} \text{ with } \zeta_h^i \approx 2.48 \pm 0.05.$$

$$n_d(p, 0) \sim \begin{cases} p^{-\zeta_d^{i>}}, & \zeta_d^{i>} \approx 2.17 \pm 0.05 \text{ for } p \gtrsim 50, \\ p^{-\zeta_d^{i<}}, & \zeta_d^{i<} \approx 2.48 \pm 0.05 \text{ for } p \lesssim 50, \end{cases}$$

The numerical estimation of  $\zeta_h^i \approx 2.48$  is to be compared with its exact value computed by Stella and Vanderzande [97],  $\zeta_h^i = 27/11 \approx 2.454$ . It is interesting to notice that the *equilibrium distribution of domain lengths* is not a single power law in contrast to the *equilibrium distribution of domain areas*.



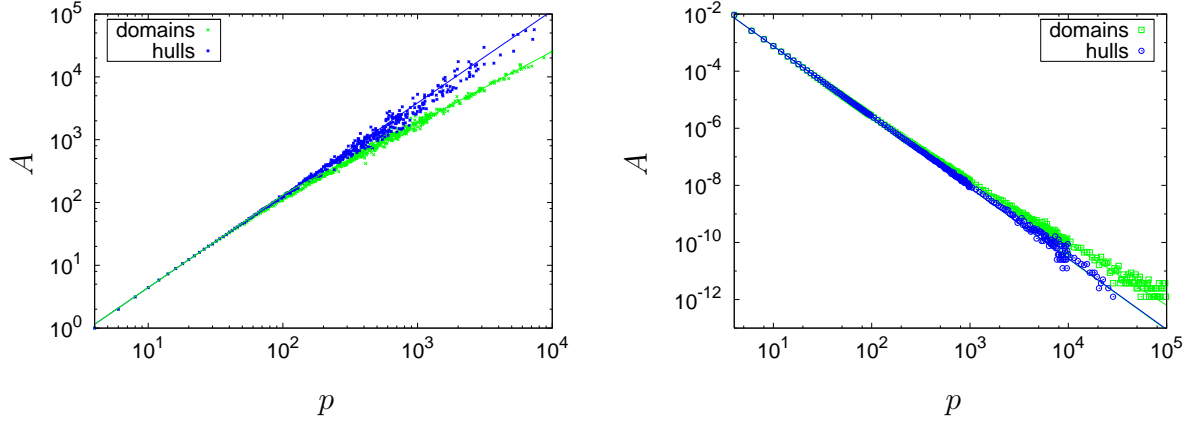


Figure 3.17: Relation between areas and perimeters (left) and distribution of domain and hull lengths, both in equilibrium at  $T_0 = T_c$ .

$T_0 = T_c$	$\alpha_h^i$	$\zeta_h^i$	$\alpha_d^{i>}$	$\zeta_d^{i>}$	$\alpha_d^{i<}$	$\zeta_d^{i<}$
	$1.47 \pm 0.1$	$2.48 \pm 0.05$	$1.14 \pm 0.1$	$2.17 \pm 0.05$	$1.47 \pm 0.1$	$2.48 \pm 0.05$
$T_0 \rightarrow \infty$	$\alpha_h^{i'}$	$\zeta_h^{i'}$	$\alpha_d^{i'>}$	$\zeta_d^{i'>}$	$\alpha_d^{i'<}$	$\zeta_d^{i'<}$
	$1.12 \pm 0.1$	$2.12 \pm 0.05$	$1.01 \pm 0.1$	$2.01 \pm 0.05$		

Table 3.1: Exponents describing the *equilibrium* geometry of both hulls and domain perimeters. It was not possible to obtain numerically  $\alpha_d^{i'>}$  and  $\zeta_d^{i'>}$ , because in order to reach critical percolation after a quench from  $T \rightarrow \infty$  we need to wait some Monte Carlo steps and this creates too much noise in the small area region.

In the case  $T_0 \rightarrow \infty$ , after a few time-steps we reach the critical percolation conditions. A numerical analysis similar to the one already performed for the critical temperature can also be done in this case. In the following, *primed quantities* are used to indicate  $T_0 \rightarrow \infty$ . The results for  $T_0 \rightarrow \infty$  are summarized in table (3.1). Note the good agreement between our numerical estimation of  $\zeta_h^{i'} \approx 2.12$  and the hull exponent in critical percolation computed analytically by Saleur and Duplantier [98]  $\zeta_h^{i'} = 15/7 \approx 2.14$ .

It is interesting to note that, for both initial conditions, the exponents characterizing the number density of perimeter lengths are significantly different. They are approximately equal to 2.5 at  $T_c$  and 2 at  $T_0 \rightarrow \infty$ . This is to be contrasted with the behaviour of the *area number densities* for which the exponents were identical for hull enclosed areas and very close indeed for domains.

The exponents  $\alpha$  and  $\zeta$  are linked by the fact that each hull-enclosed area or domain area is in one-to-one relation to its own boundary. Thus,  $n_h(A, 0)dA = n_h(p, 0)dp$ , which implies

$$\zeta_h = 1 + \alpha_h^i, \quad (3.40)$$

These conditions are also satisfied for the primed ( $T_0 \rightarrow \infty$ ) quantities. Within our numerical accuracy these relations are respected, see table (3.1).

For domain areas and domain boundaries one obtains

$$\zeta_d = 1 + (\tau - 1)\alpha_d^i, \quad (3.41)$$

These relations are also satisfied for  $\alpha_d^{i'>}$ . The numerical estimation of these values satisfy these equations, see table (3.1).

$T_0 = T_c$	$\alpha_h^>$	$\eta_h^>$	$\alpha_h^<$	$\eta_h^<$
	$1.37 \pm 0.2$	$0.26 \pm 0.15$	$1.83 \pm 0.2$	$0.06 \pm 0.02$
$T_0 \rightarrow \infty$	$\alpha_h'^>$	$\eta_h'^>$	$\alpha_h'^<$	$\eta_h'^<$
	$1.12 \pm 0.2$	$0.38 \pm 0.15$	$1.83 \pm 0.2$	$0.06 \pm 0.02$

Table 3.2: Parameters describing the geometrical structure of the *hulls* for coarsening at  $T = 0$ 

The main sources of error in the determination of the exponents in the study of the initial conditions are the following: (i) statistical errors, although we have a rather good sampling; (ii) the choice of the large area-perimeter limit that is not perturbed by finite size effects, and (iii) the fact that the  $T_0 \rightarrow \infty$  initial condition is not exactly at critical percolation. We estimated the magnitude of the error to be  $\pm 0.1$  in the  $\alpha$  exponents, and  $\pm 0.05$  in the  $\zeta$  exponents, which correspond to, roughly, less than 10% in both cases. Within this level of accuracy, the relations between exponents (3.41) and (3.40) are satisfied.

### 3.6.2 Time evolution at zero temperature

In this section we study the time evolution of the geometrical structure for both domains and hull perimeters after a quench to  $T = 0$ . Let us first discuss the hull perimeters. After a quench from  $T_0 = T_c$  (see left panel of Fig. 3.18), the hull enclosed areas and their corresponding perimeters, obey, during the dynamics, the scaling relations

$$\frac{A}{\lambda_h t} \approx \eta_h \left( \frac{p}{\sqrt{\lambda_h t}} \right)^{\alpha_h}, \quad (3.42)$$

with

$$\left. \begin{array}{l} \alpha_h^> \approx 1.37 \pm 0.2 \\ \eta_h^> \approx 0.26 \end{array} \right\} \text{ for } \frac{A}{\lambda_h t} \gtrsim 50, \quad (3.43)$$

and

$$\left. \begin{array}{l} \alpha_h^< \approx 1.83 \pm 0.2 \\ \eta_h^< \approx 0.06 \end{array} \right\} \text{ for } \frac{A}{\lambda_h t} \lesssim 10, \quad (3.44)$$

For  $T_0 \rightarrow \infty$  (see right panel of Fig. 3.18) this scaling is also valid if one replaces  $\eta_h$  and  $\alpha_h$  by the primed quantities summarized in table (3.2).

We note that the relation between area and perimeter exhibits two distinct regimes. During the coarsening process a characteristic scale  $A^*(t) \approx \lambda_h t$  develops such that hulls with enclosed area  $A > A^*$  have the same exponent as in the initial condition (structures that are highly ramified with  $\alpha$  smaller than 2) and domains with  $A < A^*$  are regular ( $\alpha$  close to 2). As shown in the right panel of Fig. 3.18, the structure of these small domains does not depend on the initial condition. This phenomenon is reminiscent of an *unroughening transition* occurring at a velocity  $\lambda_h$ . Note that we estimated the error in the exponents  $\alpha$  to be  $\pm 0.2$  and thus more important than in the analysis of the initial conditions. The reason is that the crossover from the small area to the large area regime is not sufficiently sharp and the choice of the fitting interval introduces an additional source of error. Indeed, note that in Eq. (3.42) we did not use the intermediate regime  $10 \leq \frac{A}{\lambda_h t} \leq 50$  to fit the power laws.

For the domains, we studied the relation between domain areas and their corresponding perimeters finding the same results with  $\lambda_h \rightarrow \lambda_d$  and the parameters given in table (3.3).

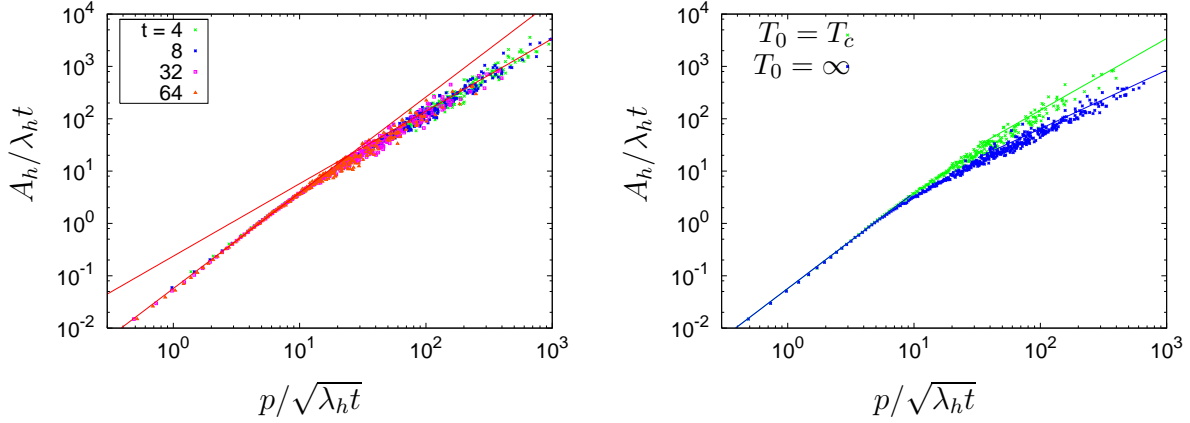


Figure 3.18: Left, time evolution of the hull enclosed area vs. perimeter relation for  $T_0 = T_c$  and different times indicated in the legend. Right, hull enclosed area vs. perimeter relation at time  $t = 32$  MCs from two different initial conditions.

In analogy with the derivation for the time-dependent number density of domain areas, the time-dependent number densities of hull and domain wall lengths are given by

$$n_{h,d}(p, t) = \int dp_i \delta(p - p(t, p_i)) n_{h,d}(p_i, t_i) \quad (3.45)$$

with  $n_{h,d}(p_i, t_i)$  the initial condition and  $p(t, p_i)$  the perimeter length of a boundary at time  $t$  that had initial length  $p_i$  at time  $t_i$ .

Let us here discuss the hull lengths. In this case one can simply use the exact number density of hull enclosed areas,  $n_h(A, t) = c_h / (A + \lambda_h t)^2$  for  $T_0 = T_c$  and Eq. (3.42) to relate time-dependent areas to their perimeters on the two regimes of large and small areas. After a little algebra one derives

$$(\lambda_h t)^{3/2} n_h(p, t) \approx \frac{\alpha_h^< \eta_h^< c_h \left( \frac{p}{\sqrt{\lambda_h t}} \right)^{\alpha_h^< - 1}}{\left[ 1 + \eta_h^< \left( \frac{p}{\sqrt{\lambda_h t}} \right)^{\alpha_h^<} \right]^2} \quad (3.46)$$

for small areas,  $A/\lambda_h t < 10$ , and

$$(\lambda_h t)^{3/2} n_h(p, t) \approx \frac{\alpha_h^> \eta_h^> c_h \left( \frac{p}{\sqrt{\lambda_h t}} \right)^{\alpha_h^> - 1}}{\left[ 1 + \eta_h^> \left( \frac{p}{\sqrt{\lambda_h t}} \right)^{\alpha_h^>} \right]^2} \quad (3.47)$$

for large areas  $A/\lambda_h t > 50$ . Note that these expressions satisfy scaling. Interestingly, the scaling function,  $f_<(x) = x^{\alpha_h^< - 1} / (1 + \eta_h^< x^{\alpha_h^<})^2$  with  $x = p/\sqrt{\lambda_h t}$  reaches a maximum at

$$x_{max} = \left( \frac{\alpha_h^< - 1}{\eta_h^< (\alpha_h^< + 1)} \right)^{1/\alpha_h^<} \quad (3.48)$$

and then falls-off to zero as another power-law. There is then a maximum at a finite and positive value of  $p$  as long as  $\alpha_h^< > 1$ , that is to say, in the regime of not too large areas. The numerical

evaluation of the right-hand-side yields  $x_{max} = p_{max}/(\sqrt{\lambda_h t}) \approx 3$  which is in the range of validity of the scaling function  $f_{<}$ . The behaviour of the time-dependent perimeter number density for long perimeters is controlled by Eq. (3.47) that falls-off as a power law  $f_{>}(x) \sim x^{-(1+\alpha_h^>)}$ . Although the function  $f_{>}$  also has a maximum, this one falls out of its range of validity. Above we used the critical Ising parameters. The results after a quench from  $T_0 \rightarrow \infty$  follow the same functional form with the corresponding primed values of  $\alpha$  and  $\eta$  and  $c_h \rightarrow 2c_h$ . The power law describing the tail of the number density of long perimeters is the same as the one characterising the initial distribution, since  $\alpha_h^> = \alpha_h^{(i)}$  and then  $1 + \alpha_h^> = \zeta_h$ . Therefore, the decay of the time-dependent number density at long perimeters after a quench from  $T_0 = T_c$  and  $T_0 \rightarrow \infty$  are distinguishably different with  $\zeta_h \approx 2.5$  and  $\zeta'_h \approx 2$ . This is to be contrasted with the small difference in the area number densities that fall with two power laws that are so close (powers of 2 and 2.05) that are impossible to distinguish numerically.

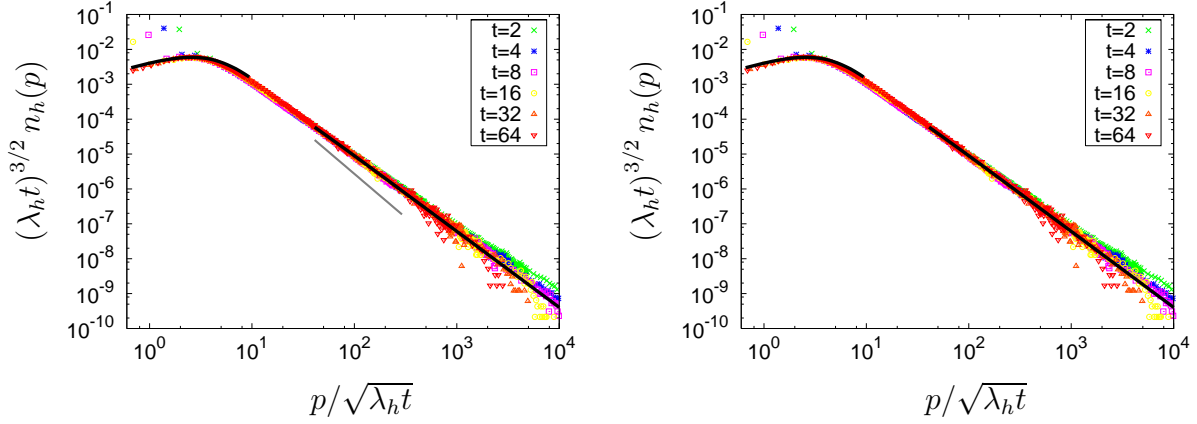


Figure 3.19: Scaling of the time-dependent number density of hull lengths evolving at  $T = 0$  from an initial condition at  $T_0 = T_c$  (left) and  $T_0 \rightarrow \infty$  (right). The solid black lines represent the theoretical prediction valid for  $A/\lambda_h t < 10$  and for  $A/\lambda_h t > 50$ . The agreement between theory and numerical data is again very impressive. The small grey line in the left plot represents the slope in the right plot, showing that in contrast with domain size distribution, perimeter distribution is very sensitive to initial conditions. The isolated data points that lie above the scaling function correspond to reversed, isolated spins within a bulk of the opposite sign that give rise to a perimeter length  $p = 4$  (four broken bonds). The area number densities also showed this anomalous behaviour for  $A = 1$ .

In Fig. 3.19 we display the scaling plot of the number density of hull lengths and we compare it to the analytic prediction (3.46) and (3.47). The data are in remarkably good agreement with the analytic prediction; the lines represent the theoretical functional forms for long and short lengths, and describe very well the two limiting wings of the number density. The maximum is located at a value that is in agreement with the prediction, Eq. (3.48).

With the same line of argument exposed above for the perimeters of the hulls, we can analyse the statistics of the domain walls, that is to say, including external and internal perimeters. For critical Ising initial conditions:

$$(\lambda_d t)^{3/2} n_d(p, t) \approx \frac{\alpha_d^< \eta_d^< c_d \left( \frac{p}{\sqrt{\lambda_d t}} \right)^{\alpha_d^<-1}}{\left[ 1 + \eta_d^< \left( \frac{p}{\sqrt{\lambda_d t}} \right)^{\alpha_d^<} \right]^\tau} \quad (3.49)$$

$T_0 = T_c$	$\alpha_d^>$	$\eta_d^>$	$\alpha_d^<$	$\eta_d^<$
	$1.16 \pm 0.2$	$0.63 \pm 0.15$	$1.83 \pm 0.2$	$0.05 \pm 0.01$
$T_0 \rightarrow \infty$	$\alpha_d'^>$	$\eta_d'^>$	$\alpha_d'^<$	$\eta_d'^<$
	$1.01 \pm 0.2$	$0.52 \pm 0.15$	$1.83 \pm 0.2$	$0.06 \pm 0.01$

Table 3.3: Parameters describing the geometrical structure of the *domains* for coarsening at  $T = 0$ 

for small areas and its obvious modification for large areas. For  $T_0 \rightarrow \infty$  one replaces  $\eta_d$  and  $\alpha_d$  by the primed quantities and  $c_d \rightarrow 2c_d$ . The scaling analysis of the number density of domain wall lengths is displayed in Fig. 3.20 for both initial conditions. Once again we find a very good agreement between the analytic predictions and the numerical data.

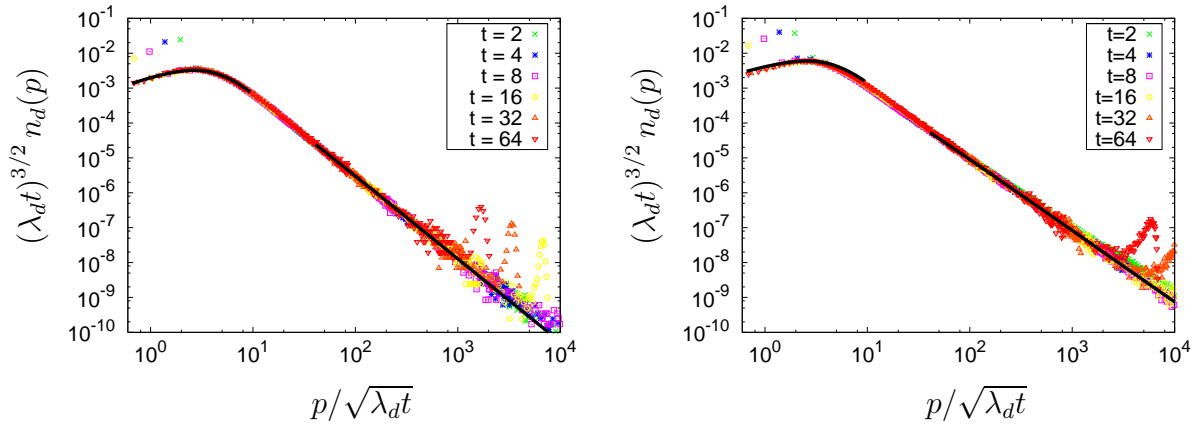


Figure 3.20: Scaling of the time-dependent number density of domain wall lengths evolving at  $T = 0$  from an initial condition at  $T_0 = T_c$  (left) and  $T_0 \rightarrow \infty$  (right). The solid black lines represent the theoretical prediction valid for  $A/\lambda_h t < 10$  and for  $A/\lambda_h t > 50$ . The origin of the isolated data points is the same as in Fig. 3.19.

### 3.6.3 Finite temperature evolution

Once we analysed the statistics of perimeters in the zero temperature dynamics, we focus on the effects of a finite working temperature. We briefly list the results below without presenting the data.

*Area-perimeter relations:* for large areas we find the same exponent as for zero temperature coarsening that is also the initial condition exponent ( $T_0 \rightarrow \infty$  or  $T_0 = T_c$ ). This is reasonable since the large structures are still ‘unaware’ of the coarsening process and thus retain the form they had in the initial configuration. For small areas, instead, we see domain walls roughening due to thermal agitation but it is hard to extract the value of the exponent  $\alpha_h^<$  with sufficient accuracy. For instance, after a quench from  $T_0 = T_c$  to  $T = 1.5$  the exponent becomes  $\alpha_h^< \approx 1.70$  (to be contrasted with the  $T = 0$  value  $\alpha_h^< \approx 1.83$ ) and after a quench from  $T_0 \rightarrow \infty$  to  $T = 1.5$  the exponent becomes  $\alpha_h'^< \approx 1.74$  (to be contrasted with the  $T = 0$  value  $\alpha_h'^< \approx 1.83$ ).

The scaling of the perimeter number densities and the functional form for the scaling function predicted analytically describe the numerical data with high precision once the values of the exponents  $\alpha$ , the prefactors  $\eta$ , and the parameter  $\lambda$  are modified to take into account thermal agitation

(for absolute area values larger than  $A \approx 10A_0$ , this value limits the range of areas where the effect of thermal fluctuations is larger than the ones of coarsening). The analytic prediction is very accurate in the region of small coarsening domains,  $A/\lambda_{d,h}t < 10$  and  $A > 10A_0$  where the maximum is located, and in the region of large coarsening domains,  $A/\lambda_{d,h}t > 10$  and  $A > 10A_0$ , for both domains and hulls and the two initial conditions.

### 3.7 Conclusions

In this chapter we studied the statistics of hull enclosed areas, domain areas and interfaces during the non-equilibrium dynamics of curvature driven coarsening in two dimensions. The analytical part of our work relies on the Allen-Cahn equation derived from the continuous Ginzburg-Landau field-theory in two-dimensions while the numerical part of it deals with Monte Carlo simulations of the  $2dIM$ . Our main results are:

- We proved scaling of the various number densities studied.
- We derived the exact number density of hull enclosed areas; we obtained approximate expressions for the number density of domain areas, hull lengths and domain perimeter lengths.
- The geometrical properties and distribution of the time dependent large structures (by large we mean much larger than the average ones) are the ones of critical continuous percolation (for all initial conditions equilibrated at  $T_0 > T_c$ ) and critical Ising (for  $T_0 = T_c$ ). The long interfaces retain the fractal geometry imposed by the equilibrium initial condition and the scaling function of all number densities decay as power laws.
- Instead, small structures progressively become regular and the area-perimeter relation is  $A \sim p^\alpha$ , with  $\alpha$  close to 2.
- We took into account the effects of a finite working temperature by eliminating purely thermal fluctuations and thus correctly identifying the coarsening structures. The temperature effect thus amounts to introducing the temperature dependence in the prefactor in the growth law,  $R(t) \sim [\lambda(T)t]^{1/2}$ .  $\lambda(T)$  is a monotonically decreasing function of  $T$  that vanishes at  $T_c$ .

It is important to stress that our analytic results rely on the use of the Allen-Cahn result for the velocity of an almost flat interface. Thus, they would be expected to hold only in a statistical sense and for large structures in the lattice model. Surprisingly, we found with numerical simulations that the number density area distributions in the  $2dIM$  match the analytic predictions for very small structures, and even after a few MC steps evolution of a critical Ising initial condition for which rather rough interfaces exist.

## Chapter 4

# Effects of the disorder: test of the super-universality hypothesis

### 4.1 Introduction

In the previous chapter we analyzed the coarsening process in pure (not disordered) two-dimensional systems with non-conserved order parameter. Here we extend the results obtained to the coarsening dynamics of two-dimensional models with non-conserved order parameter under the effect of *weak quenched disorder*. By ‘weak disorder’ we mean randomness that does not modify the character of the ordered phase (see [99] for a recent review).

An important property of domain-growth in systems with weak disorder is the so-called *super-universality hypothesis*. This hypothesis states that once the correct growing length scale (which *will depend* on the disorder strength) is taken into account, all scaling functions are independent of the disorder strength. As a consequence, these scaling functions are the same than in the pure case. This conjecture was first enunciated by Fisher and Huse in [100]. The idea is that the length scale at which the effects of quenched disorder are important is much smaller than the domain scale  $R(t)$ . The latter dominates the elastic energy. Thus the dynamics of large structures is approximately curvature driven. Pinning at small scales modifies the scale factor, that is to say the growth law  $R(t)$ , but not the scaling functions. The validity of super-universality for the scaling function of the equal-time two-point correlation of several disordered systems including the random bond Ising model was checked numerically in [101, 102, 103, 104]. The stringest test proposed in [105] that includes higher order correlations was also passed numerically in [106]. The goal of this chapter is to test the super-universality hypothesis using the exact results for the hull-enclosed areas obtained in chapter 3.

### 4.2 Hull enclosed area distribution

We have already derived an analytic expression for the hull enclosed area distribution in the non-disorder case,

$$n_h^p(A, t) = \frac{2c_h}{(A + \lambda_h t)^2} . \quad (4.1)$$

The superscript  $p$  stands for *pure*. Equation (4.1) can be recast in the scaling form

$$n_h^p(A, t) = \frac{1}{(\lambda_h t)^2} f\left(\frac{A}{\lambda_h t}\right) \quad (4.2)$$

with  $f(x) = \frac{2c_h}{(x+1)^2}$ . In this way, scaling with the characteristic length scale,  $R^p(t) = \sqrt{\lambda_h t}$ , for coarsening dynamics with non conserved order parameter in a pure system was demonstrated. The effects of a finite working temperature are fully encoded in the temperature dependence of the parameter  $\lambda_h$  while the same scaling function  $f(x)$  describes  $n_h^p$  as suggested by the zero temperature fixed point scenario.

When quenched disorder is introduced the growing phenomenon is no longer fully curvature driven and domain-wall pinning by disorder becomes relevant. At early times, the system avoids pinning and evolves like in the pure case. Later, barriers pin the domain walls and the system gets trapped in metastable states from which it can escape only by thermal activation over the corresponding free-energy barriers. In spite of these differences, coarsening in ferromagnetic systems with quenched disorder also satisfies dynamic scaling [101, 102, 103, 104, 106, 105] and a single characteristic length,  $R(t, T, \varepsilon)$ , can be identified ( $\varepsilon$  is a measure of the disorder amplitude). As a result of the competition between the curvature driven mechanism and pinning by disorder, the coarsening process is slowed down and the characteristic radius of the domains depends on the disorder strength and it is smaller than the pure one,  $R(t, T, \varepsilon) < R_p(t, T)$ . Moreover, the super-universality hypothesis applied to the scaling function of the equal-time two-point correlation function in random ferromagnets was verified numerically in a number of works [101, 102].

The scaling and super-universality hypotheses suggest that Eq. (4.2) remains valid with the same scaling function  $f(x) = 2c_h/(1+x)^2$  and  $(\lambda_h t)^{1/2}$  replaced by  $R(t, T, \varepsilon)$  for all  $2d$  non-conserved order parameter coarsening processes in which the low-temperature ordered phase is not modified. More precisely, we expect that

$$n_h(A, t, T, \varepsilon) = R^{-4}(t, T, \varepsilon) f\left[\frac{A}{R^2(t, T, \varepsilon)}\right] \quad (4.3)$$

should be valid in all these cases. In this chapter we test the superuniversality hypothesis by following the dynamic evolution of the two-dimensional random bond Ising model ( $2d$  RBIM) defined by the Hamiltonian,

$$H = - \sum_{\langle i, j \rangle} J_{ij} \sigma_i \sigma_j \quad (4.4)$$

where the  $J_{ij}$  are random variables uniformly distributed over the interval  $[1 - \varepsilon/2, 1 + \varepsilon/2]$  with  $0 < \varepsilon \leq 2$ . This model has a second-order phase transition between a high-temperature paramagnetic phase and a low-temperature ferromagnetic phase. We simulate the dynamic evolution of a model defined on a square lattice with linear size  $L = 10^3$ , using a single-flip Monte Carlo technique and the heat-bath algorithm. Data are averaged over  $10^3$  samples. We show results for a random initial condition,  $\sigma_i = \pm 1$  with equal probability to mimic an infinite temperature equilibrium state,  $T_0 \rightarrow \infty$ . At the initial time  $t = 0$  we set the working temperature to a low value and we follow the evolution thereafter. We are interested on the effect of quenched randomness and we thus focus on a single working temperature,  $T = 0.4$ , at which the ordered equilibrium phase is ferromagnetic for all  $0 \leq \varepsilon \leq 2$ . In what follows we drop the  $T$  dependence from  $R$  and  $n_h$ , so we simply denote them  $R(t, \varepsilon)$  and  $n_h(A, t, \varepsilon)$ .

We determine the growth law,  $R(t, \varepsilon)$ , from a direct measure of the spatial correlation function  $C(r, t, \varepsilon)$ :

$$C(r, t, \varepsilon) \equiv \frac{1}{N} \sum_{i=1}^N \langle s_i(t) s_j(t) \rangle_{|\vec{r}_i - \vec{r}_j| = r} \quad (4.5)$$



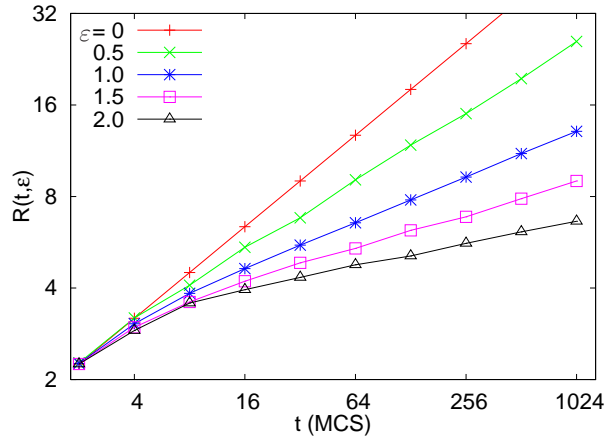


Figure 4.1: Log-log plot of the characteristic length extracted from the collapse of the equal-time two-point correlation function against time after the quench. Different curves correspond to different values of the quenched disorder strengths. For comparison we include the not disordered limit law  $R(t, \varepsilon = 0) \propto \sqrt{t}$ .

which also obeys dynamical scaling,

$$C(r, t, \varepsilon) \sim m^2(T, \varepsilon) f\left(\frac{r}{R(t, \varepsilon)}\right), \quad (4.6)$$

with  $m(T, \varepsilon)$  the equilibrium magnetisation density. In Fig. 4.1 we show  $R(t, \varepsilon)$  as a function of  $t$  for several values of the quenched disorder strength along with the pure case. We extracted  $R(t, \varepsilon)$  by collapsing the equal-time correlations data using Eq. 4.6. After a few time-steps all curves deviate from the pure  $R(t, \varepsilon = 0) \propto \sqrt{t}$  law and the subsequent growth is the slower the stronger the disorder strength  $\varepsilon$ . For strong disorder the characteristic length reaches relatively modest values during the simulation interval, for instance,  $R(t = 1024, \varepsilon = 2) \sim 7$  (measured in units of the lattice spacing). It is then quite hard to determine the actual functional law describing the late time evolution of  $R(t, \varepsilon)$  and it comes as no surprise that this issue has been the matter of debate recently [107, 108, 109, 110, 111, 112, 113, 114]. Using arguments based on the energetics of domain-wall pinning Huse and Henley [107] proposed the law  $R(t) \propto (\ln t)^{1/\psi}$  with  $\psi = 1/4$  for the random bond Ising model. More recently, powerful Montecarlo simulations [108, 109, 110, 111, 112, 113, 114] suggest a power law  $R(t) \propto t^\theta$  with a exponent  $\theta$  that depends on  $T$  and  $\varepsilon$ . We are not concerned here with predicting the time-dependence of  $R$ . Instead, we use the numerical values in Fig. 4.1 to scale our data for the distributions of hull enclosed areas and hull lengths as explained below.

In Fig. 4.2 we display data for one disorder strength,  $\varepsilon = 2$ , taken at several times after the quench. Using the scaling form, the data collapse for  $A_h/R^2(t, \varepsilon) \gtrsim 1$  over 8 decades in the vertical axis and 4 decades in the horizontal axis. Deviations are seen for small areas and we discuss their possible origin below. This analysis confirms the dynamical scaling hypothesis in the region of large areas.

In Fig. 4.3 we test the super-universality hypothesis as applied to the hull-enclosed area distribution by presenting data for a single instant,  $t = 256$  MCS, and several values of the disorder strength,  $\varepsilon = 0, 0.5, 1, 1.5, 2$ . Again, for areas such that  $A_h/R^2(t, \varepsilon) \gtrsim 1$  there is a very accurate data collapse while for smaller areas deviations, that we discuss below, are visible. The solid black line represents the analytic prediction for the pure case that yields, under the super-universality

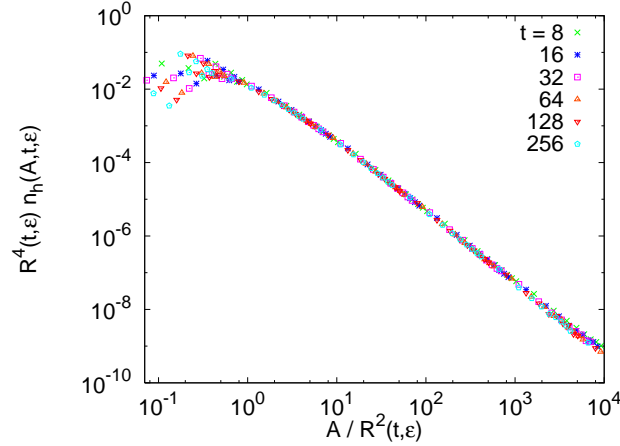


Figure 4.2: Number density of hull enclosed areas for one value of the disorder strength,  $\varepsilon = 2$ , at several times. The data are shown in the scaling form and they collapse for  $A_h/R^2(t, \varepsilon) \gtrsim 1$ .

hypothesis, the analytic prediction for all  $\varepsilon$ . The curve falls well on top of the data. In the tail of the distribution we see downward deviations that are due to finite size effects already discussed in detail in the last chapter.

Let us now examine several possible origins for the deviation of the numerical data from the analytic prediction at small areas,  $A_h/R^2(t, \varepsilon) \lesssim 1$ , in Figs. 4.2 and 4.3. The first source of problems could be the fact that we need to use a finite working temperature in the disordered case to depin the walls while the analytic results are derived at  $T = 0$ . In the pure case the effect of temperature is to create thermal domains within the genuinely coarsening ones. Based on this observation, in section 3.5 we explained that the small area probability distribution may have an excess contribution coming from these thermal fluctuations. By extracting the contribution of the *equilibrium* distribution of thermal domains, that became important for temperatures  $T \gtrsim 1$ , we showed that the number density of hull-enclosed areas at  $T > 0$  is given by the zero temperature result once scaled by  $R(T, t)$ . In the present disordered case, the working temperature we use is too low to generate any thermal domains and thus temperature cannot be the source of deviations from the analytic form.

Another possible origin of the difference between numerical data and theoretical prediction is the fact that the analytic results are derived using a continuum field-theoretic description of coarsening while numerical simulations are done on a lattice. In the presence of quenched randomness one can expect the effects of the lattice discretization to be more important than in the pure case, especially for relatively small structures. Moreover, disorder induces domain-wall roughening and the Allen-Cahn flat interface assumption is not as well justified.

Finally, the super-universality hypothesis is argued for large structures only [100] and thus the small hull enclosed areas are not really forced to follow it strictly when  $A_h \lesssim R^2(t, \varepsilon)$ .

### 4.3 Geometrical structure

In order to better characterise the geometric structure of the coarsening process we study the relation between hull-enclosed areas and their perimeters. In Fig. 4.4 we present the scatter plot of the scaled hull enclosed area,  $A_h/R^2(t, \varepsilon)$ , against the corresponding scaled perimeter,  $p_h/R^2(t, \varepsilon)$ ,

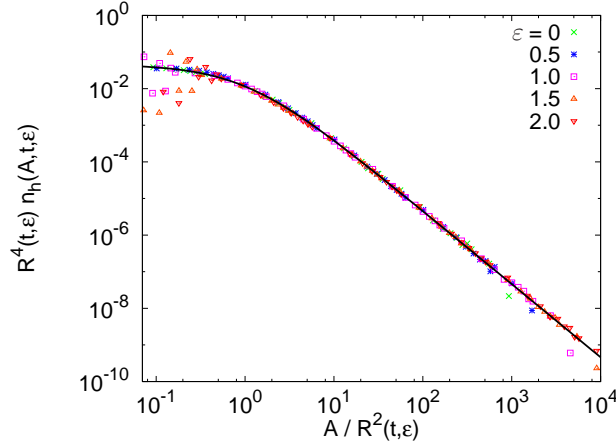


Figure 4.3: Number density of hull enclosed areas at  $t = 256$  MCs and several values of the disorder strength. The collapse of all data for  $A_h/R^2(t, \varepsilon) \gtrsim 1$  supports the validity of super-universality. The black solid line represents the analytic result for the pure case.

in a log-log plot for several values of the disorder strength at  $t = 256$  MCs. We observe a separation into two regimes at the breaking point  $p_h^*/R(t, \varepsilon) \sim 10$  and  $A_h^*/R^2(t, \varepsilon) \sim 2$ . In the upper and lower regime areas and perimeters are related by two power laws that *do not* depend on the disorder strength. As in Sect. 3.6,

$$\frac{A_h}{R^2(t, \varepsilon)} \sim \left[ \frac{p_h}{R(t, \varepsilon)} \right]^\alpha \quad (4.7)$$

with

$$\begin{aligned} \alpha^> &\approx 1.12 \pm 0.20 & \text{for } \frac{p_h}{R(t, \varepsilon)} > 10, \\ \alpha^< &\approx 1.83 \pm 0.20 & \text{for } \frac{p_h}{R(t, \varepsilon)} < 10. \end{aligned} \quad (4.8)$$

The upper exponent also characterises the highly ramified structures of the initial condition. Note that the small value of  $\alpha^>$  is not related to the existence of holes in these large structures, since hull-enclosed areas do not have holes in them. The crossover between upper and lower regimes depends on time when observed in absolute value. In other words, during the coarsening process a characteristic scale  $p^* \sim R(t, \varepsilon)$  develops such that hull-enclosed areas with perimeter  $p > p^*$  have the same exponent  $\alpha_0 \sim 1.12$  as in the initial condition before the quench (see Sect. 3.6), while hull-enclosed areas with smaller perimeter are more compact as indicated by the larger value of the exponent  $\alpha^<$ .

## 4.4 Hull length distribution

We now examine the hull length distribution that is expected to follow the scaling and super-universality hypotheses. In Fig. 4.5 we display the number density of hull lengths at  $t = 256$  MCs and  $\varepsilon = 0, 0.5, 1, 1.5, 2$ . We show the data in the form suggested by the scaling hypothesis

$$n_h(p, t, \varepsilon) = R^{-3}(t, \varepsilon) g \left[ \frac{p}{R(t, \varepsilon)} \right]. \quad (4.9)$$

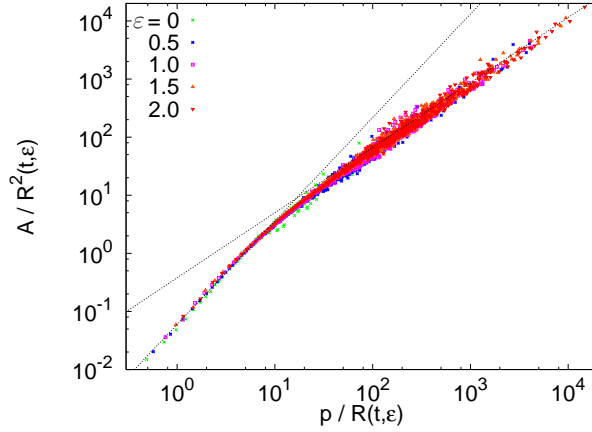


Figure 4.4: Averaged scatter plot of the scaled areas against perimeters for several values of the strength of the quenched randomness.

The data collapse on a master curve for all lengths satisfying  $p_h/R(t, \varepsilon) \gtrsim 2$  a value that is roughly the location of the maximum in the distribution. The super-universality hypothesis holds in this regime of lengths.

Relating the distribution functions of areas and perimeters through a change of variables, as explained in Sect. 3.6, we find

$$R^3(t, \varepsilon) n_h(p, t, \varepsilon) \sim \frac{\alpha^> c_h \left( \frac{p}{R(t, \varepsilon)} \right)^{\alpha^>-1}}{\left[ 1 + \left( \frac{p}{R(t, \varepsilon)} \right)^{\alpha^>} \right]^2}. \quad (4.10)$$

The scaling function is thus the same as in the pure system with two branches characterized by the exponents  $\alpha^>$  and  $\alpha^<$ . As in the pure case the maximum in the distribution is described by Eq. (4.10) with  $\alpha^<$  while the maximum found with  $\alpha^>$  falls outside its range of validity.

In Fig. 4.6 we display the number density of hull lengths scaled with the typical radius  $R$  for one value of the disorder strength at several times after the quench. The upper and lower predictions are shown with solid black lines.

## 4.5 Conclusions

In this chapter, we have analysed the statistics of hull-enclosed areas and hull lengths during the coarsening dynamics of the  $2d$  RBIM with a uniform distribution of coupling strengths. We found that the number densities of these observables satisfy scaling and super-universality for structures with  $A_h/R^2(t, \varepsilon) \gtrsim 1$  and  $p_h/R(t, \varepsilon) \gtrsim 2$ .

We showed that the analytic prediction for the number density of hull enclosed areas derived for pure systems also describes the statistics of these quantities in the presence of quenched ferromagnetic disorder. The geometrical properties of the boundaries between phases are, in principle, more sensitive to quenched randomness than their interior. We showed, however, that the relation between areas and interfaces and, in consequence, the distribution of hull lengths are independent of the disorder strength also satisfying super-universality.

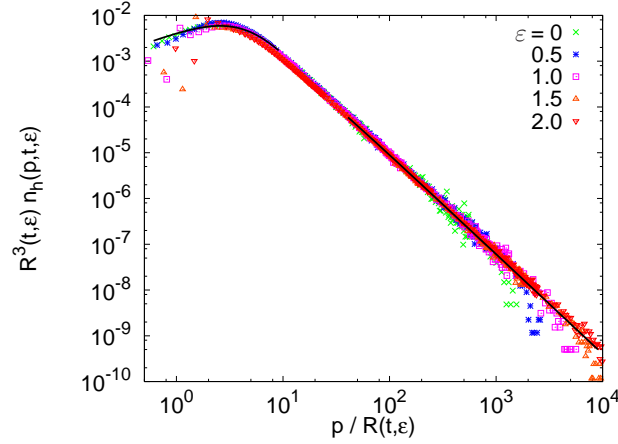


Figure 4.5: Number density of hull lengths at  $t = 256$  MCs and several values of the disorder strength given in the key. The collapse of all data for  $p_h/R(t, \varepsilon) \gtrsim 2$  supports the validity of super-universality in this regime of lengths.

In previous works all numerical tests of the super-universality hypothesis in the RBIM have focused on the study the equal time two-point correlation function [101, 102, 103, 104, 106], for which no exact results were available. The geometric approach that we have presented enables us to test the super-universality hypothesis using exact results.

We also studied a number of related problems on which we report below.

- We verified that analogous results are obtained for different probability distributions of the coupling strengths as long as these remain ferromagnetic.
- We observed that the scaling plots do not depend on the working temperature while the latter is below the critical point.

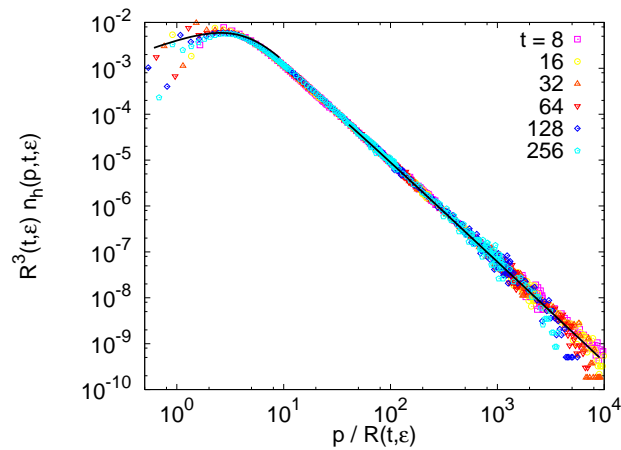


Figure 4.6: Scaling plot of the number density of hull lengths for a disorder with strength  $\varepsilon = 1.0$  at different times. The solid black lines are the analytic prediction in Eq. (4.10) and explained in the text. The part around the maximum is characterized by the exponent  $\alpha^<$  while the tail of the distribution is well-described by the exponent  $\alpha^>$ .

# Chapter 5

## Conserved dynamics

### 5.1 Phase separation: Introduction and state of the art

In the last two chapters, we have studied coarsening in systems where the order parameter is *not conserved* by the dynamics. We have obtained the distributions of different geometrical observables, and, by now, we understand which are the effects of the initial temperature, the working temperature and the disorder strength. To complete our geometrical picture of phase ordering dynamics, it would be interesting to understand what happens if the order parameter is *conserved* by the dynamics. This process, also known as *phase separation* is the topic of this chapter.

Phase separation is the process whereby a binary mixture of components  $A$  and  $B$ , initially in a homogeneous phase, demix leading to the coexistence of two phases, one rich in  $A$  and the other in  $B$ . The system, initially in an unstable spatially uniform state, performs a coarsening process to approach its thermodynamically stable phase-separated state [8].

In the case of fluids, hydrodynamic effects may be important to the demixing process [115]; these interactions are hard to treat analytically and the results of numerical simulations are sometimes controversial. Some studies even claim that dynamical scaling is broken by hydrodynamic transport [116]. In the following we focus on the phase separation process in systems without hydrodynamics. A typical realization is phase separation in binary alloys, high-viscosity fluids or polymer blends.

The time-dependent order parameter characterising the phase separation phenomenon is a continuous scalar field,  $\phi(\vec{x}, t)$ , that *represents the local difference in concentration of the two phases*, normalized by the sum of the averaged concentrations. Its evolution is described by a phenomenological Langevin-like equation:

$$\frac{\partial \phi}{\partial t} = \nabla \cdot \left[ M(\phi) \nabla \left( \frac{\delta H[\phi]}{\delta \phi} \right) \right] + \eta. \quad (5.1)$$

$H[\phi]$  is a Ginzburg-Landau type ‘free-energy’ with an elastic term and a double-well potential. The stochastic field  $\eta(\vec{x}, t)$  represents a thermal noise of zero average and correlator given by

$$\langle \eta(\vec{x}, t) \eta(\vec{x}', t') \rangle = -2T \nabla^2 \delta(\vec{x} - \vec{x}') \delta(t - t') \quad (5.2)$$

while the mobility  $M(\phi)$  is in general a function of the field  $\phi$ , as indicated. When  $M(\phi) = 1$ , Eq. (5.1) is known as the Cahn-Hilliard equation [117], or model  $B$  in the Hohenberg-Halperin classification of critical dynamics [73] (see Sect. 2.2). Several discrete models to study the phase-separation process in binary alloys have also been proposed and studied in the literature. These are

lattice gases that are themselves mapped onto Ising models with locally conserved order parameter [118]. The dynamics follows stochastic rules for the interchange of nearest neighbour  $A$  and  $B$  molecules or, in the spin language, the reversal of a pair of neighbouring antiparallel spins.

Two microscopic processes contribute to phase ordering dynamics with locally conserved order parameter, namely *bulk* and *surface* diffusion. In bulk diffusion a molecule separates (evaporation) from the surface of a domain, diffuses within the neighbouring domain of the opposite phase, and finally attaches to its original domain or another one. In the context of an Ising model simulation, there is an activation energy for this process and one can check that the dominant growth mechanism is the transport of material through the bulk from domain boundaries with *large* curvature to domain boundaries with *small* curvature. In surface diffusion molecules “walk” on the interface. This mechanism leads to the motion of whole domains in the sample and thus the possibility of merging two domains together when they collide. In the usual Kawasaki [118] spin-exchange dynamics or in model B’s evolution [119], the early dynamics is surface diffusion driven and at later time the dominant process becomes bulk diffusion. There exist, however, modified versions where either bulk or surface diffusion are suppressed [119, 120, 121]. For deep temperature quenches,  $M(\phi) \rightarrow 0$ , bulk diffusion is effectively eliminated, and domain growth proceeds by surface motion. In quenches to moderate subcritical temperatures, on the other hand, the mobility does not play an important role,  $M(\phi) \simeq \text{const.}$ , and the domain growth is bulk-driven.

Let us now review in some detail the main features of coarsening with locally conserved order parameter. Using the Cahn-Hilliard equation, it can be easily shown that the radius,  $R(t)$ , of a *single spherical* domain of negative phase ( $\phi = -1$ ) in an *infinite sea* of positive phase ( $\phi = +1$ ), evolves from time  $t = 0$  to time  $t$  as,

$$R^3(t) = R^3(0) - \frac{3}{2}\sigma t. \quad (5.3)$$

with  $\sigma$  a parameter that quantifies the surface tension (for a pedagogical derivation of this equation, see [8]). A domain with initial radius  $R_i$  thus evaporates in a time  $t \sim R_i^3$  in contrast to the non-conserved order parameter dynamics in which the area within a boundary simply shrinks under the curvature force in a time  $t \sim R_i^2$  [82].

Lifshitz-Slyozov [122] and Wagner [123] studied, for a *three-dimensional* system, the growth and shrinkage of domains of one phase embedded in one large domain of the other phase in the limit of small minority phase concentration,  $c \rightarrow 0$ . In their celebrated papers they realized that domain growth at the late stages is limited by matter diffusion through the majority domain. In this case the evolution of a domain of the minority phase with radius  $R_i$  immersed in a sea of the majority phase that is “supersaturated” with the dissolved minority species [122, 8] can follow two paths: the domain evaporates by diffusion if  $R_i < R_c$ , or it grows by absorbing material from the majority phase if  $R_i > R_c$ , where  $R_c$  is a time-dependent “critical radius”. This critical radius turns out to be the only characteristic length-scale in the system,  $R(t)$ , and serves to scale all correlation functions according to the dynamic scaling hypothesis. It grows as  $R(t) = R_c(t) \sim t^{1/3}$ . Lifshitz-Slyozov [122] also derived an expression for the density of droplets of the minority phase with linear size  $R$  in  $d = 3$ . Three important properties of the Lifshitz-Slyozov distribution are:

- The distribution of droplet radii has an upper cut-off,  $R_{\text{max}}(t)$ , where  $R_{\text{max}}(t) \sim t^{1/3}$  is a constant, equal to  $3/2$ , times the critical radius  $R_c(t)$ .
- The decay close to the cut-off is exponential.
- The density of small objects,  $R \sim 0$ , satisfies scaling and behaves as  $n(R, t) \sim R_c(t)^{-4} (R/R_c(t))^2$ , where  $n(R, t)dR$  is the number of droplets per unit volume with radius in the interval  $(R, R + dR)$ .



Later simulations established that the scaling functions depend on the minority concentration [124, 125]. The Lifshitz-Slyozov calculation can easily be extended to any space dimension  $d > 2$  [126]. However, the limit  $d \rightarrow 2$  is singular, and does not commute with the limit  $c \rightarrow 0$ . Rogers and Desai [127] showed, however, that the usual scaling forms apply in  $d = 2$ , with  $R(t) \sim t^{1/3}$ , for large  $t$  at small non-zero volume fraction  $c$ . More recently, Huse used scaling and energetic arguments to generalize the Lifshitz-Slyozov growth law and argued that it should also apply to critical quenches with equal volume fractions of the two phases [128]. Numerical simulations [128, 75], suggest that the typical domain radius scales in time as  $R(t) \sim t^{1/3}$  for any value of  $c$ , even in the 50:50 case. The scaling function for the distribution of domain areas has not been analyzed in this case.

If we take also into account the competition between bulk and surface diffusion the growth law is modified at early times. The former process is the one responsible for the scaling of global observables with a *typical* domain length  $R(t) \sim t^{1/3}$  while the latter yields a slower time-dependence,  $R(t) \sim t^{1/4}$ , that is important only at relatively short times after the quench [129, 130]. The temperature-dependent crossover can be seen, for example, in numerical simulations with Kawasaki dynamics [119]. The crossover time diverges when  $T \rightarrow 0$ . This observation has been used to develop accelerated algorithms to simulate discrete models in which only bulk diffusion processes are considered, which should describe phase-separation correctly at late times after the quench. Phase-separation in the Kawasaki spin-exchange dynamics is equivalent to a Cahn-Hilliard equation with order parameter dependent mobility. In [120], a model with  $M(\phi) = 1 - \alpha\phi^2$  was studied. The time dependent structure factor exhibits dynamical scaling, and the scaling function is numerically indistinguishable from the Cahn-Hilliard one, consistent with what was expected from numerical studies with Kawasaki dynamics.

In this chapter we study the morphology of domain and perimeter structures in the spinodal decomposition of a two dimensional system with *equal concentrations* of the two phases. In particular, we analyse the distributions of the domain areas and their associated perimeters, and the relation between areas and perimeters during the evolution. We consider both bulk-and-surface diffusion and just-bulk diffusion processes. Extending the formalism previously developed for the study of domain growth in the non-conserved case in chapters 3 and 4, we propose an analytic form for the domain size distribution function in its full-range of variation, and we test it with simulations on the two-dimensional Ising model (2dIM). Our analytic prediction for the distribution of small areas is the result of one hypothesis: that interfaces move independently. This assumption is valid for domains of any size in curvature driven dynamics: the fission of a big domain into two smaller ones or the coalescence of two domains to form a bigger one are forbidden in the continuous Allen-Cahn description (remember discussion in Sect. 3.3.1). In the conserved order parameter case, even with  $c \rightarrow 0$ , this assumption does not strictly hold and corrections must, in principle, be included. Indeed, already Lifshitz and Slyozov made an attempt to go beyond their simple model and account for coalescence when  $c \rightarrow 0$ . Later, it became clear that in locally conserved order parameter dynamics, the dominant effect not accounted for in the simple description that takes domain-boundaries as independent objects was interdomain correlations rather than coalescence. For a discussion of the limit  $c \rightarrow 0$  considering interactions between droplets see [131].

Therefore, our analytical results are just a “first order” approximation. Still, as we shall see, this approximation yields a very good description of numerical data obtained with Monte Carlo simulations. The main properties of the distributions that we will derive are:

- The number density of domain and hull-enclosed areas satisfy scaling:  $n_{h,d}(A, t) = t^{-4/3} f_{h,d}(A/t^{2/3})$ . The argument of the scaling functions arises from the fact that the characteristic area of hulls and domains grows as  $t^{2/3}$ . The prefactor  $t^{-4/3}$  follows from the fact that there is of order one domain per scale area.

- The scaling functions,  $f_{h,d}(x)$ , do not have any cut-off and extend to infinite values of  $x$  falling-off as  $(2)c_{h,d}x^{-\tau}$ , with  $x = A/(\lambda_{h,d}t)^{2/3}$ . The constants  $c_{h,d}$  are the ones in the initial (or quasi-initial – see below) area distribution,  $n_{h,d}(A_i) \sim (2)c_{h,d}/A_i^\tau$ , for  $A_i \rightarrow \infty$ . The prefactor  $c_h$  is known exactly,  $c_h = 1/8\pi\sqrt{3}$  (Sect. 3.3.2). The factor 2 is present when quenching from high temperature,  $T_0 > T_c$ , and is absent when the initial condition is the critical Ising one,  $T_0 = T_c$ . The exponent  $\tau$  depends on whether we consider hull-enclosed ( $\tau = 2$ ) or domain areas, and in the latter case on the initial condition, *i.e.* infinite or critical temperature. In both cases it is very close to 2.
- After a quench from high temperature to a sufficiently low working temperature,  $T \ll T_c$ , the small-argument behaviour of the scaling function is  $f(x) \propto \sqrt{x}$ , in agreement with the Lifshitz-Slyozov-Wagner prediction for the small concentration limit. At higher working temperature and for critical initial conditions the behaviour is modified in a way that we describe in the text.

The chapter is organised as follows. In Sect. 5.2 we describe an approximate analytic derivation of the time-dependent hull enclosed and domain area distributions. These arguments do not rely on any scaling hypothesis but rather support its validity. We compare our approach to the celebrated Lifshitz-Slyozov-Wagner theory [122, 123]. In Sect. 5.3 we show our numerical results for the statistics of areas in the  $2d$ IM evolving with locally conserved dynamics. We use variants [121] of the Kawasaki algorithm [118] that we briefly explain in this section. The use of different algorithms allows us to switch surface diffusion on and off, and pinpoint the relative importance of these processes. Section 5.4 is devoted to the analysis, both analytical and numerical, of the geometry of domain walls during the dynamics and their relation to the corresponding areas. Finally, in the conclusion we summarize our results.

## 5.2 Statistics of areas: analytic results

In this section we analyze the number density of hull-enclosed and domain areas.

### 5.2.1 Initial distribution

We study the coarsening dynamics after a quench from  $T_0 \rightarrow \infty$ . Equilibrium infinite temperature initial conditions (fraction of up spins =  $1/2$ ) are below the critical random percolation point ( $p_c \approx 0.59$ ) for a square lattice in  $d = 2$ . After a few MC steps, however, the system reaches the critical percolation condition, *e.g.* the expected  $A^{-2}$  tail is observed in the distribution of hull enclosed areas. We have checked that this is so from the analysis of several correlation functions as well as the distribution of structures. This fact justifies the use of the Cardy-Ziff exact result for the distribution of hull-enclosed areas at critical percolation [83] as our effective initial condition from  $T_0 \rightarrow \infty$ .

In Chapter 3 we have already introduced the equilibrium distribution of hull-enclosed and domain areas, domain walls and their geometrical relation to their associated areas at critical percolation. We do not repeat the description of these properties here, but just list the initial distributions,  $n_{h,d}(A_i, t_i)$ , of hull-enclosed and domain areas [83, 42]:

$$\begin{aligned} n_h(A_i, t_i) &= \frac{2c_h}{A_i^2} \\ n_d(A_i, t_i) &= \frac{c_d A_0^{\tau-2}}{A_i^\tau}, \quad \tau = \frac{379}{187} \end{aligned} \quad (5.4)$$

### 5.2.2 Characteristic domain length

It is by now well-established [122, 128] that the spatial equal-time correlation function in demixing systems is correctly described by the dynamic scaling hypothesis with a characteristic length  $R(t) \sim t^{1/3}$  in agreement with the Lifshitz-Slyozov-Wagner prediction [122, 123] and the extension beyond the small concentration limit derived by Huse [128]. The effect of temperature fluctuations is expected to be described by a  $T$ -dependent prefactor,  $R(t, T) = [\lambda(T)t]^{1/3}$ . In the following we do not write the  $T$  dependence explicitly.

### 5.2.3 Large structures

It is natural to assume that at time  $t$ , as for non-conserved order parameter dynamics, large structures, characterized by a long linear dimension  $R \gg R(t)$ , have not changed much with respect to the initial condition. We shall support this claim with the numerical results. Thus, for sufficiently large hull-enclosed areas such that the time-dependence can be neglected we expect

$$n_h(A, t) \approx \frac{2c_h}{A^2}, \quad A \gg t^{2/3}. \quad (5.5)$$

Similarly, for large domains, the area dependence of their distribution follows that of the initial condition, Eq. (5.4).

### 5.2.4 Small structures

Small structures, such that  $R \ll R(t)$ , are mostly embedded in very large domains. To a first approximation we shall assume that they are *independent*. Moreover, they are not expected to have holes of the opposite phase within, implying the equivalence between hull-enclosed and domain areas at these scales. Indeed, any smaller structure placed within must have evaporated by time  $t$ . We then propose that the number density of *small* hull-enclosed or domain areas at time  $t$  can be written as a function of the initial distribution,

$$n(A, t) \approx \int_0^\infty dA_i \delta(A - A(t, A_i)) n(A_i, t_i), \quad (5.6)$$

with  $A_i$  the initial area and  $n(A_i, t_i)$  their number density at the initial time  $t_i$ .  $A(t, A_i)$  is the area of a domain at time  $t$  that had area  $A_i$  at time  $t_i$ . In writing this equation we have implicitly assumed that an area cannot split into two, and that two such areas cannot coalesce, which is not strictly true in conserved order parameter dynamics. Note that for sufficiently large areas so that the time-dependence is not important and  $A \sim A_i$  Eq. (5.6) immediately yields  $n(A, t) = n(A_i, t_i)$  and Eq. (5.5) is recovered. It has to be stressed, however, that Eq. (5.6) does not strictly apply in this case.

Assuming that the small areas are *circular*

$$A^{3/2}(t, A_i) = A_i^{3/2} - \lambda_h(T)(t - t_i), \quad (5.7)$$

see Eq. (5.3), and after a straightforward calculation using Eq. (5.4) for the initial distribution one finds

$$(\lambda_h t)^{4/3} n_h(A, t) = \frac{2c_h \left[ \frac{A}{(\lambda_h t)^{2/3}} \right]^{1/2}}{\left\{ 1 + \left[ \frac{A}{(\lambda_h t)^{2/3}} \right]^{3/2} \right\}^{5/3}} \quad (5.8)$$

for hull-enclosed areas. This prediction has the expected scaling form  $n_h(A, t) = t^{-4/3} f(A/t^{2/3})$  corresponding to a system with characteristic area  $A(t) \sim t^{2/3}$  or characteristic length scale  $R(t) \sim t^{1/3}$ . At very small areas,  $A \ll (\lambda_h t)^{2/3}$ , where our approximations are better justified, one has

$$(\lambda_h t)^{4/3} n_h(A, t) \approx 2c_h \left[ \frac{A}{(\lambda_h t)^{2/3}} \right]^{1/2}. \quad (5.9)$$

As expected, taking the limit  $A/(\lambda_h t)^{2/3} \gg 1$  in Eq. (5.8) one recovers Eq. (5.5). Although this limit goes beyond the limit of validity of Eq. (5.8) we shall propose that Eq. (5.9) actually holds, at least approximately, for all values of  $A/(\lambda_h t)^{2/3}$ .

In Chapter 3 we have studied non-conserved order parameter dynamics and we derived the number density of domain areas from the one of hull-enclosed areas. The key fact in this case was that we could treat the distribution of hull-enclosed areas *exactly* and then use a small  $c_h \simeq 0.023$  expansion to get the statistical properties of domains. In the case of phase separation our results for hull-enclosed areas are already approximate. Still, the relation between hull-enclosed area distribution and domain area distribution obtained in chapter 3 should remain approximately true, as a first order expansion in small  $c_h$ , since small domains are not expected to have structures within. In conclusion, for large areas and long times such that a regularizing microscopic area  $A_0 = \lambda_d t_0$  can be neglected, we expect the same functional form as the one given in Eq. (5.8) with  $c_d = c_h + \mathcal{O}(c_h^2)$ ,  $\lambda_d = \lambda_h[1 + \mathcal{O}(c_h)]$  and the power 5/3 in the denominator replaced by  $(2\tau' + 1)/3$ :

$$\begin{aligned} (\lambda_d t)^{4/3} n_d(A, t) &\simeq \frac{2c_d \left[ \frac{A}{(\lambda_d t)^{2/3}} \right]^{1/2}}{\left\{ 1 + \left[ \frac{A}{(\lambda_d t)^{2/3}} \right]^{3/2} \right\}^{(2\tau' + 1)/3}} \\ &\equiv g(x) \end{aligned} \quad (5.10)$$

with  $x = A/(\lambda_d t)^{2/3}$ , and

$$(\lambda_d t)^{4/3} n_d(A, t) \simeq 2c_d \left[ \frac{A}{(\lambda_d t)^{2/3}} \right]^{1/2} \quad (5.11)$$

for  $A \ll (\lambda_d t)^{2/3}$ . This expression can be compared to Eq. (3.34), valid for non-conserved order parameter dynamics.

Let us emphasize again the main approximation of our analytical approach: we are considering each domain boundary as an independent entity. This is strictly true for the non-conserved order parameter treated in chapter 3, but is an approximation in the conserved order parameter problem.

### 5.2.5 Super universality

All the results above are valid for the bulk diffusion driven case. What happens if we consider the case in which bulk and surface diffusion are in competition, or whether we include quenched disorder in the couplings? If we suppose that all these systems belong to the same dynamical universality class, the scaling functions being the same, then Eq. (5.8) can be generalized in the form

$$R^4(t) n_h(A, t) = \frac{2c_h \left[ \frac{A}{R^2(t)} \right]^{1/2}}{\left\{ 1 + \left[ \frac{A}{R^2(t)} \right]^{3/2} \right\}^{5/3}} \quad (5.12)$$

and similarly for the domain area distribution. The time-dependence in  $R(t)$  should include all regimes (*e.g.*  $t^{1/4}$  and  $t^{1/3}$  in the clean case with surface and bulk diffusion) and can be extracted from the dynamic scaling analysis of the correlation functions. We shall check numerically the super-universality hypothesis.

### 5.3 Statistics of areas: numerical tests

To test our analytic results we carried out numerical simulations on the  $2d$  square-lattice Ising model (2dIM) with periodic boundary conditions.

$$H = - \sum_{\langle i,j \rangle} J_{ij} \sigma_i \sigma_j \quad (5.13)$$

where  $\sigma_i = \pm 1$ . We will start considering the pure model,  $J_{ij} = J > 0 \ \forall ij$ , and then the random bond model in which the  $J_{ij}$  are random variables uniformly distributed over the interval  $[1/2, 3/2]$ . We used several versions of conserved order parameter dynamics that switch on and off surface diffusion. These are Kawasaki dynamics at finite temperature including both surface and bulk diffusion, and accelerated bulk diffusion in which surface diffusion is totally suppressed. Bulk diffusion needs to overcome energy barriers; thus this variant runs at finite temperature only. In all cases we implemented the continuous time method and the algorithms become rejection free. A detailed description of these algorithms appeared in [121]. Domain areas are identified with the Hoshen-Kopelman algorithm [81].

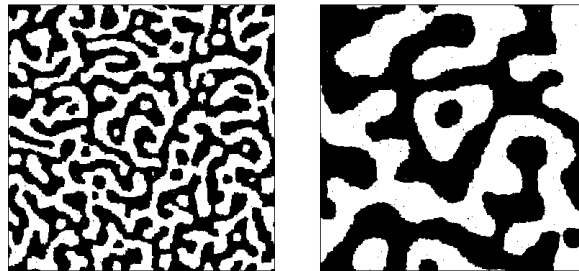


Figure 5.1: Snapshots of the  $2d$  Ising model evolving with locally conserved order parameter at  $t = 1000$  and  $t = 16000$  equivalent MC steps using the accelerated bulk algorithm explained in Sect. 5.3. The initial condition is a random configuration of  $\pm 1$  spins taken with probability one half, that is to say an infinite temperature state. Evolution occurs at  $T = 1.0$ .

All data have been obtained using systems with size  $L^2 = 10^3 \times 10^3$  and  $10^3$  runs using independent initial conditions. We ran at different temperatures specified below. We considered equilibrium at infinite temperature as initial condition,  $T_0 \rightarrow \infty$ .

### 5.3.1 Domain areas

In Fig. 5.2 (left) we show the time-dependent domain area distribution in double logarithmic scale, at three different times, following a quench from  $T_0 \rightarrow \infty$  to  $T = 1.0$ . The working temperature is very low compared to the critical value,  $T_c = 2.269$ .

The figure shows a strong time dependence at small areas and a very weak one in the tail, which is clearly very close to a power law. The curves at small areas move downwards and the breaking point from the asymptotic power law decay moves towards larger values of  $A$  for increasing  $t$ . We include the spanning domain in the statistics: the bumps on the tail of the distribution is a finite size effect visible only when the number of domain areas has already decreased by several orders of magnitude. In the tail of the probability distribution function (pdf) the numerical error is smaller than the size of the data points. The discussion of finite size effects given in previous chapters also applies to this case.

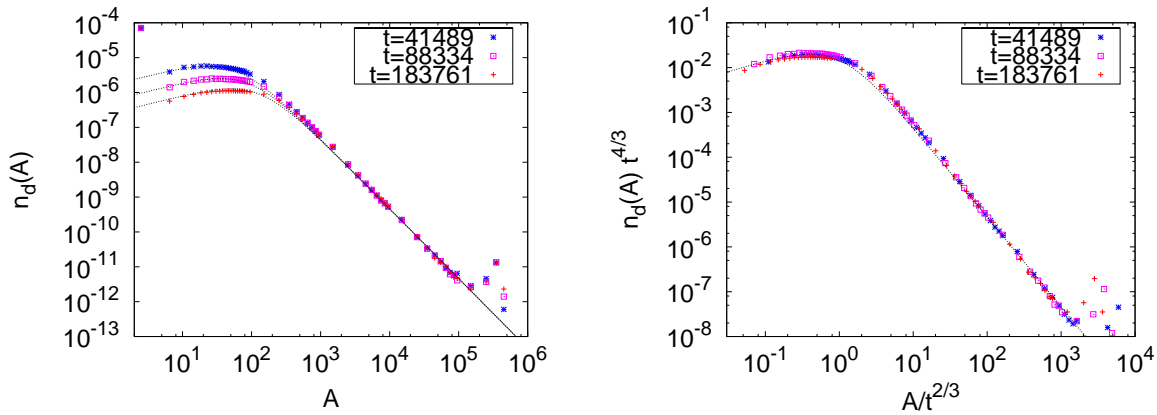


Figure 5.2: Left panel: Number density of domains areas per unit area for the  $2dIM$  evolving at  $T = 1.0$  after a quench from  $T_0 \rightarrow \infty$  using the accelerated algorithm. The dotted line represents the analytical prediction. Right panel: rescaled data using the typical domain area time-dependence  $A \sim t^{2/3}$ . The dotted line is the theoretical prediction Eq. (5.10).

We test the analytic prediction: the very good agreement between the analytical theory and the data is quite impressive. In Fig. 5.2 (right) we scale the data by plotting  $(\lambda_d t)^{4/3} n_d(A, t)$  against  $A/(\lambda_d t)^{2/3}$  with  $\lambda_d = 0.0083$ . For areas  $A$  larger than the ‘typical’ value  $(\lambda_d t)^{2/3}$  the time and  $\lambda_d$  dependence become less and less important. We fit the parameter  $\lambda_d(T)$  by analysing the behaviour at small areas,  $A^{3/2} < \lambda_d(T)t$ , and we find, that  $\lambda_d(T = 1.0) = 0.0083$  yields the best collapse of data. The full line is our prediction Eq. (5.10).

In Fig. 5.3 we present the domain area distribution for the evolution using the Kawasaki algorithm both for the clean and the disordered system. The agreement with the analytical prediction is as good as with the bulk-diffusion algorithm, suggesting the validity of super universality between both dynamics.

We extract the growing length  $R(t)$  from the analysis of the spatial correlation function and we find very good agreement between the numerical data and the scaling function suggesting that super-universality with respect to the inclusion of disorder in the interactions also holds.

Up to now we showed results obtained using a rather low working temperature. We now study whether and how our results are modified when using higher values of  $T$ . Figure 5.4 shows the numerical data and proves that the scaling is well-satisfied at all times and for all areas. The large

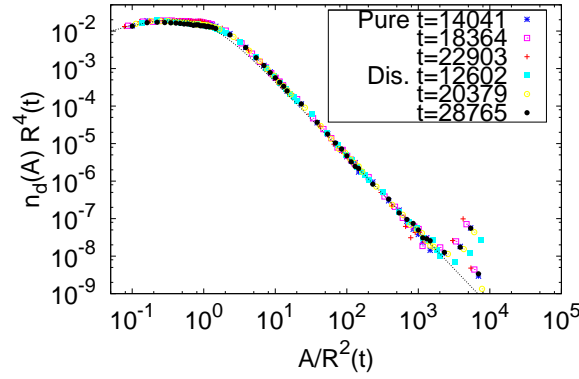


Figure 5.3: Simulations with the Kawasaki algorithm, without and with disorder. The solid lines represent the analytic prediction with  $c_d = 0.025$ ,  $\tau' = 2.055$  and  $\lambda_d = 0.3$ . For the disordered case, the growth law  $R(t)$  is extracted from the spatial correlation function. Even if there is deviations from the theoretical curve, the data seems to show super-universality.

scale behaviour of the distribution is not modified by  $T$  and all data are well-described by the initial condition form. Instead, the small scale behaviour depends strongly on temperature fluctuations. The anomalous up-rising part of the distribution at small areas is time-independent, suggesting that it can be associated with equilibrium fluctuations of the domain-walls. As shown in Fig. 5.4, it is possible to extract the interface thermal fluctuations as was done in Sect. 3.5.

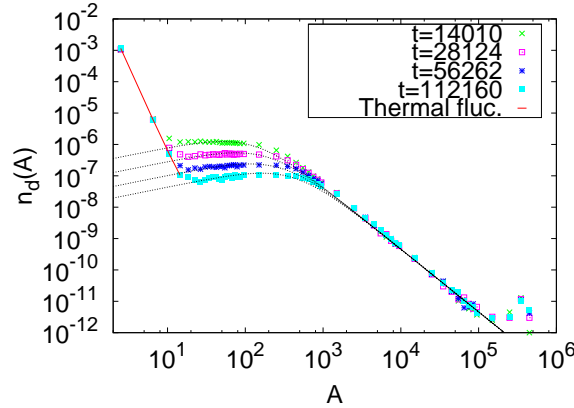


Figure 5.4: Number density of domains areas per unit area for the  $2dIM$  evolving at  $T = 1.5$  after a quench from  $T_0 \rightarrow \infty$  using the accelerated bulk algorithm. The prefactor  $\lambda_d(T)$  in the growing length is chosen to be  $\lambda_d(T) = 0.0060$ . Compare to the results shown in Fig. 5.2 obtained for a lower working temperature.

## 5.4 Statistics of perimeters and fractal properties

The analytic argument described in Sect. 5.2 can be extended to study the distribution of domain wall perimeters. The domain perimeter is the total length of the interface between the chosen

domain and the neighbouring ones – including the hull and internal borders. In this section we present the analytic prediction for this function together with numerical results that confirm it. We concentrate on  $T_0 \rightarrow \infty$  and low-working temperature. In the simulations we define the length of the boundary as the number of broken bonds.

After a quench from  $T_0 \rightarrow \infty$ , the domain areas,  $A$ , and their corresponding perimeters,  $p$ , obey the scaling relations (see Fig. 5.5)

$$\frac{A}{(\lambda_d t)^{2/3}} \sim \eta'_d \left( \frac{p}{(\lambda_d t)^{1/3}} \right)^{\alpha'_d}, \quad (5.14)$$

with

$$\left. \begin{array}{l} \alpha'_d{}^> \sim 1.00 \pm 0.1 \\ \eta'_d{}^> \sim 0.75 \end{array} \right\} \text{ for } \frac{A}{(\lambda_d t)^{2/3}} \gtrsim 10, \quad (5.15)$$

and

$$\left. \begin{array}{l} \alpha'_d{}^< \sim 2.00 \pm 0.1 \\ \eta'_d{}^< \sim 0.045 \end{array} \right\} \text{ for } \frac{A}{(\lambda_d t)^{2/3}} \lesssim 10. \quad (5.16)$$

The relation between areas and perimeters exhibits two distinct regimes with a quite sharp crossover between them. During the coarsening process a characteristic scale  $R(t) \sim (\lambda_d t)^{1/3}$  develops such that domains with area  $A > R^2(t)$  have the same exponent as in the initial condition (structures that are highly ramified with  $\alpha'^< \simeq 1$ ) and domains with  $A < R^2(t)$  become regular ( $\alpha'^< \simeq 2$ ). Interestingly, the small structures in the non-conserved order parameter dynamics are not completely circular, as demonstrated by the fact that their  $\alpha'^< \simeq 1.8$ , see Fig. 5.5.

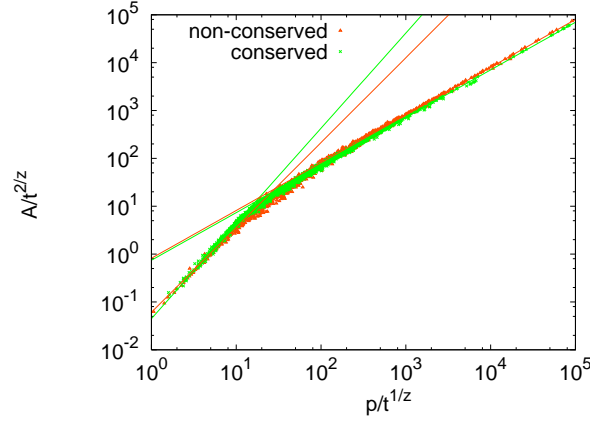


Figure 5.5: The time-dependent relation between the area and the domain boundary evolving at  $T = 1.0$  after a quench from  $T_0 \rightarrow \infty$  using conserved and non-conserved order parameter dynamics. The lines are fits to the data points. For the large structures the fit yields  $\alpha'^> \simeq 1$  in both cases while for the small structures it yields  $\alpha'^> \simeq 2$  for conserved order parameter dynamics (circular domains) and  $\alpha'^> \simeq 1.8$  for non-conserved order parameter dynamics. Here  $z = 2$  and  $3$  for non-conserved and conserved dynamics respectively.

In analogy with the derivation in Chap. 3 for the time-dependent number density of domain



areas, the time-dependent number density of domain-wall lengths,  $n_d(p, t)$ , is given by

$$(\lambda_d t) n_d(p, t) \approx \frac{\alpha_d'^{<} (\eta_d'^{<})^{3/2} 2c_d \left( \frac{p}{(\lambda_d t)^{1/3}} \right)^{\frac{3\alpha_d'^{<} - 2}{2}}}{\left[ 1 + (\eta_d'^{<})^{3/2} \left( \frac{p}{(\lambda_d t)^{1/3}} \right)^{\frac{3\alpha_d'^{<} - 2}{2}} \right]^{\frac{2\tau' + 1}{3}}} \quad (5.17)$$

for small areas,  $A/(\lambda_d t)^{2/3} < 10$ , and the same expression with  $\eta_d'^{<}$  and  $\alpha_d'^{<}$  replaced by  $\eta_d'^{>}$  and  $\alpha_d'^{>}$  for large areas  $A/(\lambda_d t)^{2/3} > 10$ . Note that these expressions satisfy scaling. The scaling function,  $f_{<}(x)$ , with  $x = p/(\lambda_d t)^{1/3}$ , reaches a maximum at

$$x_{max} = \left( \frac{3\alpha_d'^{<} - 2}{2(\eta_d'^{<})^{\frac{3}{2}} [\alpha_d'^{<}(\tau' - 1) + 1]} \right)^{2/(3\alpha_d'^{<})} \quad (5.18)$$

and then falls-off to zero as another power-law. There is then a maximum at a finite and positive value of  $p$  as long as  $\alpha_d'^{<} > 1$ , that is to say, in the regime of not too large areas. The numerical evaluation of the right-hand-side yields  $x_{max} = p_{max}/(\lambda_d t)^{1/3} \sim 3$  which is in the range of validity of the scaling function  $f_{<}$ . The time-dependent perimeter number density for long perimeters falls-off as a power law  $f_{>}(x) \sim x^{\alpha_d'^{>}(1-\tau')-1}$ . Although the function  $f_{>}$  also has a maximum, this one falls out of its range of validity. The power law describing the tail of the number density of long perimeters is the same as the one characterising the initial distribution.

In Fig. 5.6, left and right, we display the time-dependent perimeter number densities for a system evolving at  $T = 1.0$  after a quench from  $T_0 \rightarrow \infty$ . The data are in remarkably good agreement with the analytic prediction; the lines represent the theoretical functional forms for long and short lengths, and describe very well the two limiting wings of the number density. The maximum is located at a value that is in agreement with Eq. (5.18).

## 5.5 Conclusions

In this paper we studied the statistics and geometry of hull-enclosed and domain areas and interfaces during spinodal decomposition in two dimensions.

The analytical part of our work is an extension of what we presented in Chapt. 3 and 4 for the non-conserved order parameter case. The numerical part of it deals with Monte Carlo simulations of the  $2dIM$  with locally conserved magnetization. Our main results are:

- We derived the scaling functions of the number density of domain areas and perimeters with an approximate analytic argument. The expression that we obtained has two distinct limiting regimes. For areas that are much smaller than the characteristic area,  $R^2(t)$ , the Lifshitz-Slyozov-Wagner behaviour is recovered. These structures are compact with smooth boundaries, close to circular, since the area-perimeter relation is  $A \sim p^2$ .
- At higher  $T$  the small area behaviour departs from the Lifshitz-Slyozov-Wagner prediction. As for non-conserved order parameter dynamics, once we subtracted the contribution from thermal domains within the growing structures, the universal prediction is recovered.

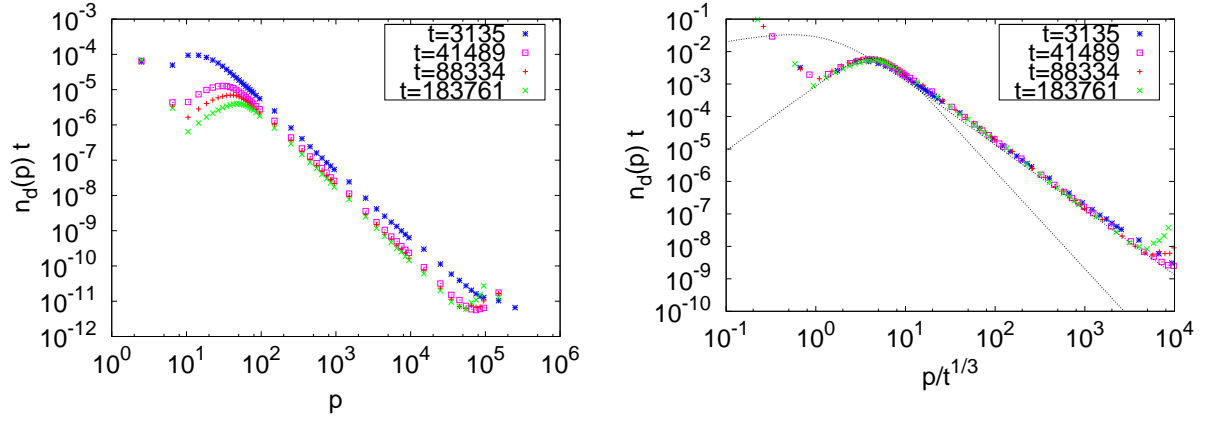


Figure 5.6: The time-dependent number density of perimeters evolving at  $T = 1.0$  from an initial condition at  $T_0 \rightarrow \infty$ . Left panel: raw data; note that the time-dependence is visible in the whole range of values of  $p$  (while in the area number densities the large area tails were very weakly dependent on time). Right panel: scaled data and analytic predictions for the small and large area regimes.

- The geometrical properties and distribution of the time-dependent areas that are larger than  $R^2(t)$  are the ones of critical continuous percolation. The long interfaces retain the fractal geometry imposed by the equilibrium initial condition.

## Chapter 6

# Experiments in the coarsening dynamics of liquid crystals

### 6.1 Introduction

In this chapter, we present an experimental application of our results. We performed an experiment on the coarsening dynamics of liquid crystals in collaboration with the group lead by Ingo Dierking (Manchester).

When applying an electric field to the liquid crystal studied (details below), we observe phase separation through the formation and coarsening of chiral domains (i.e. domains of opposite handedness). It is proposed that *deracemization* (phase ordering) in this system is a curvature-driven process. We will test this prediction using the exact result for the distribution of hull-enclosed areas in two-dimensional non-conserved phase ordering dynamics obtained in chapter 3.

We will show that the experimental data are in good agreement with the theory. We thus demonstrate that deracemization in such liquid crystal belongs to the Allen-Cahn universality class, and that the exact formula, which gives us the statistics of the hull enclosed areas during coarsening, can also be used as a strict test for this dynamic universality class.

In the next section we describe the experimental setup, and then we present a detailed analysis and discussion of the data.

### 6.2 Experimental setup

*Liquid crystals (LCs)* are substances that exhibit phases of matter that have properties between those of a conventional liquid, and those of a solid crystal. A *LC* may flow like a liquid, but have the molecules in the liquid arranged in a crystal-like way. The optical and electrical properties of *LCs* make them very interesting for technological purposes, e.g. in display devices.

Most *LCs* are formed by rod-like molecules or disc-shaped molecules. In the last decade, a lot of attention has been devoted to a new type of *LCs*: the so-called *banana shape LCs*. These *LCs*, formed by bent-core molecules, show physical properties not present in traditional *LCs*. The new macroscopic properties have their microscopical origin in the steric constraints on the packing of bent-core molecules (for a review on these peculiar *LCs*, see [132]).

In particular, we are interested in the ability of some banana-shape *LCs* to form helical structures of different chirality. Since the discovery of Louis Pasteur, more than 150 years ago, that chiral crystals can form from an achiral solution [133], deracemization has been a fundamental question in the investigation of chirality. Deracemization in an achiral fluid system is very unusual and a

topic of only recent interest [134]. It can occasionally be observed in liquid crystalline systems [135, 136, 137] formed by bent-core molecules. The most likely microscopical reason for chiral conglomerate formation are the complicated steric interactions. This is also evidenced by computer simulations which indicate chiral conformations of on the average achiral molecules [138]. Electric field induced switching between chiral domains was demonstrated in Refs. [139, 140].

The liquid crystal employed in our investigation is comprised of bent-core molecules. The studied cell has a gap of  $5\mu\text{m}$  filled with the *LC*, while lateral dimensions are much larger, approximately  $1\text{cm}$  in each direction. We are thus effectively investigating a  $2d$  system. The liquid crystal was synthesised by the group of M. B. Ros in Zaragoza, Spain. The cell itself is prepared by Extebarria group in Bilbao, but is just a standard, commercially available liquid crystal cell. The cell preparation conditions at its chemical properties are discussed in detail in Ref. [141]. Domain coarsening was followed by temperature controlled polarizing microscopy (Nikon Optiphot-Pol microscope in combination with a Linkham TMS91 hot stage), with a control of relative temperatures to  $0.1\text{K}$ . Digital images were captured at a time resolution of  $1\text{s}$ . with a pixel resolution of  $N = 1280 \times 960$ , corresponding to a sample size of  $520 \times 390\mu\text{m}^2$  (JVC KY-F1030). Note that the imaging box is approximately  $1/200$  of the whole sample. The imaging dimension is limited by the apparatus and microscope objectives we can use. Electric square-wave fields of amplitude  $E = 14\text{V}\mu\text{m}^{-1}$  and frequency  $f = 110\text{Hz}$  were applied by a TTI-TG1010 function generator in combination with an in-house built linear high voltage amplifier.

The experimental procedure is straight forward: the cell, lying over the hot stage, is placed in a polarizing microscope, equipped with the digital camera for image acquisition. The inner substrates of the cell are coated with a transparent layer of Indium tin oxide to act as electrodes. Electric fields are applied to the cell (effectively a plate capacitor filled with a dielectric) via the function generator and broad frequency range linear amplifier. Cooling from the isotropic liquid, an optically isotropic fluid liquid crystal phase is formed, which exhibits no birefringence and thus appears dark between crossed polarizers. On electric field application, chiral deracemization occurs with domains of opposite handedness growing as a function of time. This coarsening process can easily be followed when the polarizers are slightly de-crossed by a few degrees. Big chiral domains of opposite handedness get larger and larger and smaller structures disappear.

### 6.3 Analysis of the images

We performed 10 runs lasting 10 min. each with pictures taken at intervals of 10 s. on a single sample. Each run is initialized by heating the sample above the transition temperature and subsequently cooling below it before applying the electric field that starts the phase ordering. The coarsening process is visualized in terms of domains, i.e., connected regions of the same handedness. In Fig. 6.1 we show a series of snapshots taken at times  $t = 0, 60, 120, \dots, 300\text{s}$ . These pictures are then thresholded and an Ising spin  $s_i$  is assigned to each pixel, where  $s_i(t) = \pm 1$  for pixels that belong to left or right handed domains, respectively. There are many spurious small domains that are related to the image analysis. The induced graininess is also reflected in the small  $r$  behavior of the pair correlation function  $C(r, t)$  and the small  $A$  behaviour of  $n_h(A, t)$  as we shall see below. Still, at first view, the snapshots 6.1 look very similar to the ones obtained in simulations of the  $2d\text{IM}$  with non conserved dynamics.

The initial “magnetization density” in the imaging window of the liquid crystal, defined as the average of the spin variables over the box,  $m(0) = N^{-1} \sum_{i=1}^N s_i(0)$ , is not zero. This initial value is only approximately conserved by the dynamics,  $m(t) \approx m(0) = 0.2 \pm 0.1$ , but the actual value depends on the thresholding operation.

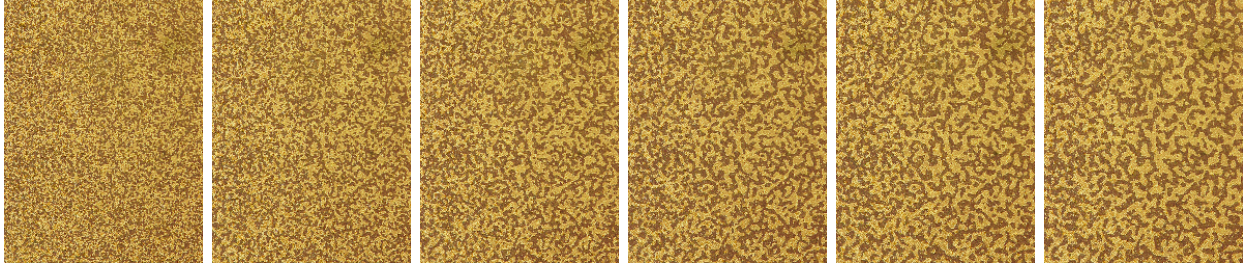


Figure 6.1: The first snapshot displays the configuration right after the quench,  $t = 0$ s. The others are snapshots during the evolution  $t = 60, 120, \dots, 300$ s.

We determine the growth law for the size,  $R(t)$ , of typical domains from a direct measure of the spatial correlation function,

$$C(r, t) \equiv \frac{1}{N} \sum_{i=1}^N \langle s_i(t) s_j(t) \rangle_{|\vec{r}_i - \vec{r}_j| = r}, \quad (6.1)$$

The angular brackets indicates an average over the 10 runs. The distance dependence of the pair-correlation at five equally spaced times,  $t = 100, \dots, 500$ s is displayed with thin (red) lines in the left panel of Fig. 6.2. As a consequence of the non-zero magnetization,  $C(r, t)$  does not decay to zero at large  $r$ . More strikingly, the curves are time-independent at distances  $r \lesssim 5$  ( $C \gtrsim 0.55$ ) and they clearly depend on time at longer distances with a slower decay at longer times. Here and in what follows we measure distances in units of the lattice spacing. The time-independence at short-distances and the long-distance decay are atypical, as can be seen by comparing to the spatial correlation in the 2dIM displayed in the inset to Fig. 6.2 (left). We ascribe the lack of time-dependence at short scales and the further slow decay to the graininess of the experimental system. Indeed, in the main panel of Fig. 6.2 (left) we also show, with thick dashed (black) lines, the correlation in the 2dIM where we have flipped, at each measuring instant, 10% of spins taken at random over the sample (the system dynamics are not perturbed and between measurements we use the original spins). By comparing the two sets of curves we see that the effect of the random spins is similar to the one introduced by the graininess of the system. This effect will also be important for the analysis of the hull-enclosed area distribution.

The function  $C(r, t)$  obeys dynamical scaling,

$$C(r, t) \simeq g[r/R(t)]. \quad (6.2)$$

We define the characteristic length-scale  $R(t)$  at time  $t$  by the condition  $C(R, t) = 0.2$  but other choices give equivalent results. The good quality of the scaling is shown in the right panel of Fig. 6.2. The time-dependence of the growing length  $R(t)$  is shown in the inset to Fig. 6.2 (right) with points. The error bars are estimated from the variance of the values obtained from the 10 independent runs. We measure the growth exponent  $1/z$  by fitting the long-time behavior of  $R(t)$ , say for  $t > 30$  s, and we find  $1/z \simeq 0.45 \pm 0.10$ . The exponent thus obtained is close to the theoretically expected value  $1/2$  for clean non-conserved order parameter dynamics [8]. The data suggest that for times longer than  $t \simeq 30$  s the system is well in the scaling regime.

We now turn to the analysis of the distribution of hull enclosed areas. In chapter 3 we derived an exact analytical expression for the hull enclosed area distribution of curvature driven two-dimensional coarsening with non-conserved order parameter:

$$n_h(A, t) = 2c_h / (A + \lambda_h t)^2. \quad (6.3)$$

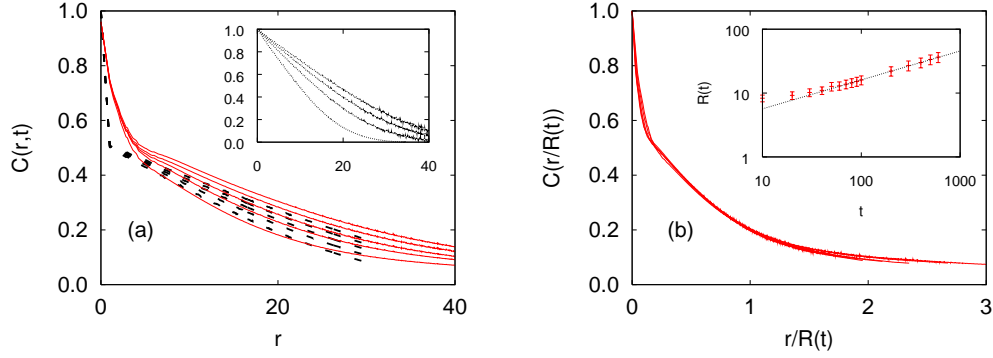


Figure 6.2: Spatial correlation function at different times after the quench. Left: experimental data at five equally spaced times,  $t = 100, \dots, 500$ s with thin (red) lines, and numerical simulation data in the 2dIM with 10% randomly flipped spins at five equally spaced times,  $t = 100, \dots, 500$  MCs with dashed (black) lines. We clearly notice the effect of graininess at very small scales ( $r \lesssim 5$  in the experiment and  $r \lesssim 1$  in the simulation), where there is no time-dependence in either case. Inset: the actual spatial correlation in the 2dIM. Right: Study of the scaling hypothesis,  $C(r,t) \simeq g[r/R(t)]$  in the liquid crystal, at the same times as in the left panel. Inset: the time-dependence of the growing-length scale. The slope of this line is  $1/z \simeq 0.45 \pm 0.10$ .

Using the digital images, we counted the number of hull-enclosed areas in  $[A, A+dA]$  to construct  $n_h(A, t)$ . It is important to note that the experimental data are taken using a *finite* imaging window and, in each sample and at each measuring time, many domains touch the boundaries (in contrast to the numerical simulations in chapters 3, 4 and 5 in which we used periodic boundary conditions).

In the left panel of Fig. 6.3 we show the hull-enclosed area distribution in the liquid crystal at three different times. In the main panel we included in the statistics the chopped areas that touch the border of the image. The upward deviation of the data with respect to the asymptotic power law  $A^{-2}$  is due to the finite image size. Indeed, domains that touch the border are actually larger but get chopped and contribute to bins of smaller  $A$ 's and this induces a bias in the data. The inset displays  $n_h$  removing from the statistics the areas that touch the border. The same anomaly appears in the 2dIM if one uses a finite imaging box within the bulk. To show this we simulated a system with  $L = 1280$  and periodic boundary conditions and we measured  $n_h$  in a finite square window with linear size  $\ell = 1000$  using 100 independent samples. In the right panel of Fig. 6.3 we show two sets of data for the 2dIM; in both cases we exclude the spanning cluster over the full system size. One set of data includes areas touching the border and lies above the theoretical curve. In the other set we eliminated these areas from the statistics and the data points fall on the analytic curve recovering the  $A^{-2}$  tail.

The data in Fig. 6.4 do not show any noticeable time-dependence at either small or large  $A$ . In the small area limit the time-independence can be traced back to the lack of time-dependence in the correlation function at distances  $r \lesssim 5$  (which corresponds to  $A \simeq \pi r^2 \lesssim 80$ ), roughly the scale of the spatial graininess (see Fig. 6.2). In the large area limit the time-dependence naturally disappears; structures with  $A \gg R^2(t)$  are basically the ones already present in the initial condition and have not had time to evolve yet. In between these two limits the curves show a shoulder with a systematic time-dependence that is the most relevant part of our experimental data and it is well described by the analytic prediction (6.3) shown with solid lines. To conclude we show that the random spins introduced by the measuring method are not only responsible for the time-independence of  $n_h$  at

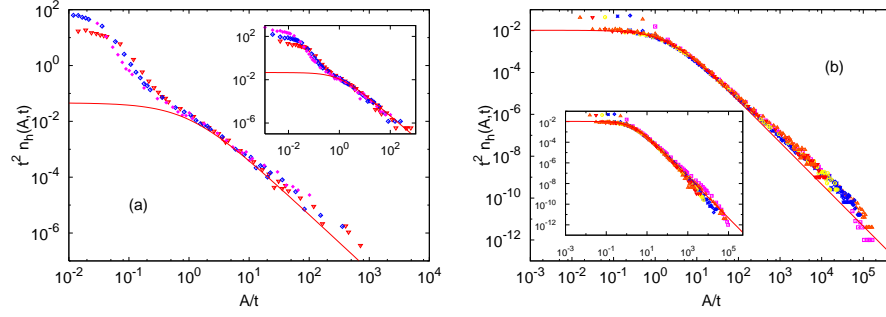


Figure 6.3: Scaling plot of the number density of hull-enclosed areas in: (a) the experiment; (b) the 2dIM with linear size  $L = 1280$  and periodic boundary conditions evolving with non-conserved order parameter at  $T = 0$ . In the latter the measurements are done on a box with linear size  $\ell = 1000$ . The lines are the prediction in Eq. (6.3). In the 2dIM case we exclude the spanning clusters from the statistics. In the insets we exclude all domains that touch the border while in the main panels we include them in the statistics.

small areas but also for the excess weight of the distribution in this region. In the inset to Fig. 6.4 we show the hull-enclosed area distribution in the 2dIM where we introduced 10% random spins at each measuring time. There is indeed a strong similarity with the experimental data in the main panel that could even be improved by choosing to flip spins in a fine-tuned correlated manner.

## 6.4 Conclusion

In summary, our experimental results for the hull-enclosed area distribution in the coarsening dynamics of the liquid crystal are in very good agreement with the exact analytic prediction for  $2d$  non-conserved scalar order parameter dynamics presented in Chap. 3. We thus demonstrate that deracemization in such bent-core liquid crystals belongs to the Allen-Cahn universality class, and that our theoretical results can be useful in interesting experimental situations.

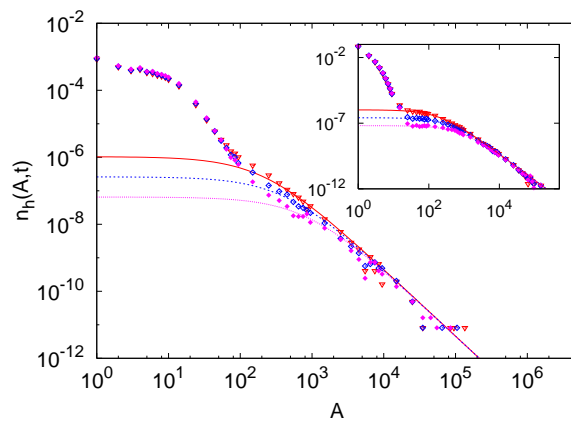


Figure 6.4: The number density of hull-enclosed areas for the liquid crystal sample at  $t = 100, 200, 400$ s, excluding from the analysis the areas that touch the box border. Inset:  $n_h$  for the 2dIM with 10% randomly flipped spins at measurement (see the text for an explanation). In both cases the lines are the theoretical prediction (6.3) with  $c_h = 1/8\pi\sqrt{3}$  and  $\lambda_h = 2.1$ .



## Chapter 7

# Geometry of $2d$ coarsening: a final picture emerging

Let us summarize in this final chapter the picture that emerges from all these studies in the geometry of  $2d$  coarsening:

- The dynamical scaling hypothesis describes very accurately the evolution of all of the systems considered. In the case of phase ordering dynamics with non conserved order parameter, we were able to obtain a proof of the dynamical scaling hypothesis.
- The growth law  $R(t)$  appearing in the scaling hypothesis, not only determines the *average size* of the geometrical structures in the system, but also a *dynamical cross-over* between *large* and *small* coarsening structures. This cross-over can be well characterized when studying geometrical observables, but it is “hidden” in non-geometrical observables such as correlation or response functions.
- *Large structures*, with an area at time  $t$  larger than the typical one  $A(t) > R^2(t)$ , keep the *ramified* geometry they had initially. The areas or perimeters distributions for large structures are the ones corresponding to the equilibrium state before the quench. Even in the non-conserved case, where we obtained the distributions in the whole range of areas or perimeters, the time dependence is negligible for structures with area  $A(t) > R^2(t)$ . The difference between the coarsening from the two extreme initial states,  $T_0 = T_c$  and  $T_0 \rightarrow \infty$ , can be clearly seen in the distribution of perimeters, where the power-law decay is different enough (the distribution of areas presents a power-law decay too close for both initial cases).
- *Small structures* do not keep the initial geometry but become more *regular*. The reason is because structures with typical area  $A(t) < R^2(t)$  “know” that the coarsening process has already started. For a clean system with conserved order parameter, small domains are indeed circular while for non-conserved order parameter they become close to circular. The difference between the  $T_0 = T_c$  and  $T_0 \rightarrow \infty$  cases can be clearly seen, in the small area region, by the extra factor 2 appearing in the latter. For small structures, when exact analysis are not possible, one can infer their time-evolution under the assumption of independence. These small coarsening structures should not be confused with the *equilibrium thermal fluctuations*, which display *time-independent* distributions. Thermal fluctuations can also be characterized by studying correlation or response functions.

- The scaling functions depend on the type of dynamics considered (e.g., conserved or non-conserved order parameter) but they do not depend on the presence of weak disorder or finite temperature once scaled by the pertinent growth law  $R(t)$ .

The results presented along this manuscript can be useful in experiments, as shown in chapter 6 for the coarsening dynamics of liquid crystals.

## Appendix A

# Algorithm to obtain the hull enclosed area

In this appendix, we present the algorithm we developed to identify the hull-enclosed area in the  $2dIM$ .

In order to obtain the size of each hull in an  $L \times L$  system, a biased walk along the interior border of each domain is performed, with the hull enclosed area being updated at each step.

*Labelling.* The  $N = L \times L$  sites are initially indexed from 0 to  $N - 1$  (top-left=0) while the domains are identified and labelled by the Hoshen-Kopelman algorithm [81]. By construction, all sites in each domain receive the (unique) label corresponding to the smaller index among its spins.

*Starting point.* The putative starting site for the walk is the spin whose index identifies the cluster. In some cases (for example, when the cluster crosses a border), it may not be the left-most/top-most site, as it should in order to be counted correctly by the implementation of the algorithm below. Although such domains may be excluded from the statistics, for finite sizes the introduced bias is unacceptable. Thus, before starting, we try to find another site in the same cluster above or to the left of the original spin, where a new starting site may be found. Once this first site is correctly identified, we assign a height  $y_0$ .

*The walk.* From the starting point, we try to turn clockwise around the domain border. Viewed from the incoming direction, the attempted move is performed in the sequence: left, front, right and backwards. For the sake of notation, we label the four directions with the indices shown in the table A. Thus, for example, if the previous step was 0, the attempted order will be 1, 0, 3 and 2.

*The area.* The first step sets the area to the value  $A_1 = y_0 + 1$ . As the walk proceeds, both area and the height are updated,  $A_{i+1} = A_i + \Delta A$  and  $y_{i+1} = y_i + \Delta y$  (in this order), where  $\Delta A$  and  $\Delta y$  depend also on the former direction (see table A). At the end of the walk, when the departure site is reached, if the last direction is 1, we increase  $A$  by  $-y$ . Care should be taken when the starting point has right and bottom neighbours belonging to the same cluster (but not the bottom right diagonal), because in this case the walk should only be finished after the second time the starting point is visited.

$t - 1$	$t$	$\Delta A$	$\Delta y$
0	0	0	1
0	1	0	0
0	2	$y + 1$	-1
0	3	$y + 1$	0
1	0	$-y$	1
1	1	$-y$	0
1	2	0	-1
1	3	1	0
2	0	$-y$	1
2	1	$-y$	0
2	2	0	-1
2	3	0	0
3	0	0	1
3	1	1	0
3	2	$y + 1$	-1
3	3	$y + 1$	0

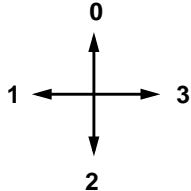


Table A.1: Incremental area contribution for each step during the oriented walk along the domain border. The values depend both on the present ( $t$ ) and former steps ( $t - 1$ ). On the right we show the labelling of the four possible directions.

# Bibliography

- [1] G. Gallavotti and E.G.D. Cohen, *Journal of Statistical Physics* 80 (1995) 931.
- [2] C. Jarzynski, *C. R. Physique* 8 (2007) 495.
- [3] G.E. Crooks, *Phys. Rev. E* 60 (1999) 2721.
- [4] L.F. Cugliandolo and J. Kurchan, *Phys. Rev. Lett.* 71 (1993) 173.
- [5] L.F. Cugliandolo and J. Kurchan, *J. Phys. A: Math. Gen.* 27 (1994) 5749.
- [6] L.F. Cugliandolo, J. Kurchan and L. Peliti, *Phys. Rev. E* 55 (1997) 3898.
- [7] A. Crisanti and F. Ritort, *J. Phys. A: Math. Gen.* 36 (2003) R181.
- [8] A.J. Bray, *Adv. Phys.* 43 (1994) 357.
- [9] J.J. Arenzon et al., *Phys. Rev. Lett.* 98 (2007) 145701.
- [10] A. Sicilia et al., *Phys. Rev. E* 76 (2007) 061116.
- [11] A. Sicilia et al., *EPL* 82 (2008) 10001.
- [12] A. Sicilia et al., *Phys. Rev. Lett.* 101 (2008) 197801.
- [13] A. Sicilia et al., *arXiv:0809.1792* (2008).
- [14] M.B. Hindmarsh and T. Kibble, *Rep. Prog. Phys.* 58 (1995) 477.
- [15] A. Vilenkin and E. Shellard, *Cosmic strings and other topological defects* (Cambridge University Press, 1994).
- [16] A. Gangui, *arXiv:astro-ph/0303504* .
- [17] T. Kibble, *arXiv:astro-ph/0410073* .
- [18] T.W.B. Kibble, *J. Phys. A: Math. Gen.* 9 (1976) 1387.
- [19] Y. Bunkov and H. Godfrin, editors, *Proceedings of the NATO-ASI on topological defects and non-equilibrium dynamics of symmetry breaking phase transitions* (Kluwer, Dordrecht, 2000).
- [20] W.H. Zurek, *Phys. Rep.* 276 (1996) 177.
- [21] C. Bauerle et al., *Nature (London)* 382 (1996) 332.

- [22] V.M.H. Ruutu et al., *Nature* (London) 382 (1996) 334.
- [23] L.E.S. et al., *Nature* 443 (2006) 312.
- [24] T. Kibble, *Physics Today* September (2007) 47.
- [25] A. Polkovnikov and V. Gritsev, arXiv:0706.0212 .
- [26] W.H. Zurek, U. Dorner and P. Zoller, *Phys. Rev. Lett.* 95 (2005) 105701.
- [27] A. Polkovnikov, *Phys. Rev. B* 72 (2005) 161201.
- [28] J. Dziarmaga, *Phys. Rev. Lett.* 95 (2005) 245701.
- [29] L.F. Cugliandolo, G. Biroli and A. Sicilia, in preparation .
- [30] P.D. Francesco, P. Mathieu and D. Senechal, *Conformal Field Theory* (Springer, 1997).
- [31] A.A. Belavin, A.M. Polyakov and A.B. Zamolodchikov, *J. Stat. Phys.* 34 (1984) 763.
- [32] S. Smirnov, *Proc. Int. Congr. Math.* 2 (2006) 1421.
- [33] I. Affleck and F.D.M. Haldane, *Phys. Rev. B* 36 (1987) 5291.
- [34] A.W.W. Ludwig, *Nucl. Phys. B* 285 (1987) 97.
- [35] V. Dotsenko, M. Picco and P. Pujol, *Nucl. Phys. B* 455 (1995) 701.
- [36] M. Bauer and D. Bernard, *Phys. Lett. B* 557 (2003) 309.
- [37] R. Santachiara, *Nucl. Phys. B* 793 (2008) 396.
- [38] M. Picco and R. Santachiara, *Phys. Rev. Lett.* 100 (2008) 015704.
- [39] C.M. Fortuin and P.W. Kasteleyn, *Physica* 57 (1972) 536.
- [40] R.H. Swendsen and J.S. Wang, *Phys. Rev. Lett.* 62 (1987) 361.
- [41] U. Wolff, *Phys. Rev. Lett.* 62 (1989) 361.
- [42] D. Stauffer and A. Aharony, *Introduction to Percolation Theory* (Taylor and Francis, Burgess Science Press, Basingstoke, London, 1994).
- [43] M.P.M. den Nijs, *Phys. Rev. B* 27 (1983) 1674.
- [44] A. Coniglio et al., *J. Phys. A: Math. Gen.* 10 (1977) 205.
- [45] A. Coniglio and W. Klein, *J. Phys. A* 13 (1980) 2775.
- [46] F.C. Alcaraz, *J. Phys. A: Math. Gen.* 20 (1987) 2511.
- [47] F.C. Alcaraz, *J. Phys. A: Math. Gen.* 20 (1987) 623.
- [48] J. Cardy, *J. Phys. A* 13 (1980) 1507.
- [49] M. Picco, R. Santachiara and A. Sicilia, *Journal of Statistical Mechanics: Theory and Experiment* (2009) P04013.

- [50] K. Kaneko, *Prog. Theor. Phys.* 72 (1984) 480.
- [51] J. Miller and D. Huse, *Phys. Rev. E* 48 (1993) 2528.
- [52] D.A. Egolf, *Nature* 369 (1994) 129.
- [53] A. Lemaitre and H. Chate, *Phys. Rev. Lett.* 77 (1996) 0521.
- [54] L.F. Cugliandolo, E. Katzav and A. Sicilia, in preparation .
- [55] F.Y. Wu, *Rev. Mod. Phys.* 54 (1982) 253.
- [56] M.P. Loureiro et al., In preparation .
- [57] M. Blume, *Phys. Rev.* 141 (1966) 517.
- [58] H.W. Capel, *Physica* 32 (1966) 966.
- [59] F. Wang and D.P. Landau, *Phys. Rev. Lett.* 86 (2001) 2050.
- [60] K. Binder and D.P. Landau, *Phys. Rev. B* 30 (1984) 1477.
- [61] A.J. Bray, *Phys. Rev. B* 41 (1990) 6724.
- [62] K. Humayun and A.J. Bray, *Phys. Rev. Lett.* 62 (1989) 2841.
- [63] G.F. Mazenko and O.T. Valls, *Phys. Rev. B* 26 (1982) 389.
- [64] G.F. Mazenko, O.T. Valls and F.C. Zhang, *Phys. Rev. B* 32 (1985) 5807.
- [65] Z.W. Lai, G.F. Manzenko and O. Valls, *Phys. Rev. B* 37 (1988) 9481.
- [66] C. Roland and M. Grant, *Phys. Rev. B* 39 (1989) 11971.
- [67] F. Corberi, A. Coniglio and M. Zannetti, *Phys. Rev. E* 51 (1995) 5469.
- [68] J.P. Bouchaud et al., *Spin Glasses and Random Fields* (World Scientific, Singapore, 1998).
- [69] T.S. Grigera and N.E. Israeloff, *Phys. Rev. Lett.* 83 (1999) 5038.
- [70] L. Buisson, S. Ciliberto and A. Garcimartin, *Eurphys. Lett.* 63 (2003) 603.
- [71] D. Herisson and M. Ocio, *Eur. Phys. J. B* 40 (2004) 283.
- [72] H.A. Makse and J. Kurchan, *Nature* 415 (2002) 614.
- [73] P. Hohenberg and B.I. Halperin, *Rev. Mod. Phys.* 49 (1977) 435.
- [74] A. Coniglio and M. Zannetti, *Europhys. Lett.* 10 (1989) 575.
- [75] J.G. Amar and F. Family, *Phys. Rev. A* 41 (1990) 3258.
- [76] B. Derrida, C. Godereche and I. Yekutieli, *Phys. Rev. A* 44 (1991) 6241.
- [77] T.J. Newman, A.J. Bray and M.A. Moore, *Phys. Rev. B* 42 (1990) 4514.
- [78] P.C. Martin, E. Siggia and H.A. Rose, *Phys. Rev. A* 8 (1973) 423.

- [79] C.D. Dominicis and L. Peliti, *Phys. Rev. B* 18 (1978) 353.
- [80] U.C. Tauber, Critical dynamics: a field theoretical approach to equilibrium and non-equilibrium scaling behaviour (<http://www.phys.vt.edu/tauber/>).
- [81] J. Hoshen and R. Kopelman, *Phys. Rev. B* 14 (1976) 3438.
- [82] S.M. Allen and J.W. Cahn, *Acta Metall.* 27 (1979) 1085.
- [83] J. Cardy and R.M. Ziff, *J. Stat. Phys.* 110 (2003) 1.
- [84] A. Weinrib, *Phys. Rev. B* 26 (2001) 1352.
- [85] J. Kalda, *Phys. Rev. E* 64 (2001) 020101 (R).
- [86] K. Barros, P.L. Kaprivsky and S. Redner, *arXiv:0905.3521* .
- [87] R. Zallen and H. Sher, *Phys. Rev. B* 4 (1971) 4471.
- [88] K. Barros, P.L. Kapivsky and S. Redner, *arXiv:0905.3521* .
- [89] A.D. Rutenberg, *Phys. Rev. E* 54 (1996) R2181.
- [90] A.L. Stella and C. Vanderzande, *Phys. Rev. Lett.* 62 (1989) 1067.
- [91] W. Janke and A.M.J. Schakel, *Phys. Rev. E* 71 (2005) 036703.
- [92] K.T. Leung, *J. Phys. A* 26 (1993) 6691.
- [93] B. Derrida, *Phys. Rev. E* 55 (1997) 3705.
- [94] H. Hinrichsen and M. Antoni, *Phys. Rev. E* 57 (1998) 2650.
- [95] H.B. Tarko and M.E. Fisher, *Phys. Rev. B* 11 (1975) 1217.
- [96] J.L. Cambier and M. Nauenberg, *Phys. Rev. B* 19 (1986) 2675.
- [97] C. Vanderzande and A.L. Stella, *J. Phys. A* 22 (1989) L445.
- [98] H. Saleur and B. Duplantier, *Phys. Rev. Lett.* 56 (1986) 545.
- [99] S. Puri, *Phase Transitions* 77 (2004) 469.
- [100] D.S. Fisher and D.A. Huse, *Phys. Rev. B* 38 (1988) 373.
- [101] A.J. Bray and K. Humayun, *J. Phys. A* 24 (1991) L1185.
- [102] S. Puri, D. Chowdhury and N. Parekh, *J. Phys. A* 24 (1991) L1087.
- [103] H. Hayakawa, *J. Phys. Soc. Japan* 60 (1991) 2492.
- [104] T. Iwai and H. Hayakawa, *J. Phys. Soc. Japan* 62 (1993) 1583.
- [105] R.E. Blundell, A.J. Bray and S. Sattler, *Phys. Rev. E* 48 (1993) 2476.
- [106] B. Biswal, *Physica A* 229 (1996) 72.
- [107] D.A. Huse and L. Henley, *Phys. Rev. Lett.* 54 (1985) 2708.



- [108] J.H. Oh and D.I. Choi, Phys. Rev. B 33 (1986) 3448.
- [109] R. Paul, S. Puri and H. Rieger, Europhys. Lett. 68 (2004) 881.
- [110] H. Rieger, G. Schehr and R. Paul, Prog. Theor. Phys. Suppl. 157 (2005) 111.
- [111] R. Paul, S. Puri and H. Rieger, Phys. Rev. E 71 (2005) 061109.
- [112] F. Baumann, M. Henkel and M. Pleimling, arXiv:0709.3228 .
- [113] M. Henkel and M. Pleimling, arXiv:0703466 .
- [114] H. Hinrichsen, arXiv:0711.2421 .
- [115] E.D. Siggia, Phys. Rev. A 20 (1979) 595.
- [116] A.J. Wagner and J.M. Yeomans, Phys. Rev. Lett. 80 (1998) 1429.
- [117] J.W. Cahn and J.E. Hilliard, J. Chem. Phys. 28 (1968) 258.
- [118] K. Kawasaki, Phys. Rev. 150 (1966) 285.
- [119] S.V. Gemmert, G.T. Barkema and S. Puri, Phys. Rev. E 72 (2005) 046131.
- [120] S. Puri, A.J. Bray and J.L. Lebowitz, Phys. Rev. E 56 (1997) 758.
- [121] M.E.J. Newman and G.T. Barkema, Monte Carlo Methods in Statistical Physics (Oxford Univ. Press, New York, 1999).
- [122] I.M. Lifshitz and V.V. Slyozov, J. Phys. Chem. Solids 65 (1961) 581.
- [123] C. Wagner, Z. Elektrochem 65 (1961) 581.
- [124] S. Puri, Phys. Lett. A 134 (1988) 205.
- [125] R. Toral, A. Chakrabarti and J.D. Gunton, Physica A 213 (1995) 41.
- [126] J.H. Yao et al., Phys. Rev. B 47 (1993) 14110.
- [127] T.M. Rogers and R.C. Desai, Phys. Rev. B 34 (1986) 7845.
- [128] D. Huse, Phys. Rev. B 34 (1986) 7845.
- [129] G.F. Mazenko, Phys. Rev. B 43 (1991) 5747.
- [130] G. Szabo, Phys. Rev. E 57 (1998) 6172.
- [131] M. Marder, Phys. Rev. A 36 (1987) 858.
- [132] G. Pelzl, S. Diele and W. Weissflog, Advanced Materials 11 (1999) 707.
- [133] L. Pasteur, C. R. Acad. Sci. 26 (1848) 535.
- [134] Y. Takanishi et al., Angew. Chem. Int. Ed. 38 (1999) 2353.
- [135] J. Thisayukta et al., J. Am. Chem. Soc. 122 (2000) 7441.
- [136] G. Heppke, D.D. Parghi and H. Sawade, Liq. Cryst. 27 (2000) 313.

- [137] N.V.S. Rao et al., J. Mater. Chem. 13 (2003) 2880.
- [138] D.J. Earl et al., Phys. Rev. E 71 (2005) 021706.
- [139] A. Eremin et al., Phys. Rev. E 67 (2003) 020702(R).
- [140] A. Kane et al., ChemPhysChem 8 (2007) 170.
- [141] J. Martinez-Perdiguero et al., Phys. Rev. E 77 (2008) 020701(R).